Universidad de Concepción
Dirección de Postgrado
Facultad de Ciencias Químicas
Programa Doctorado en Ciencias Geológicas

Evaluación del Peligro Sísmico Para Movimientos Extremos del Terreno en Escenarios de Fuente Cercana.

(*Seismic Hazard Assessment for Extreme Ground Motions in Near-Source Environments*)

Tesis para optar al grado de Doctor en Ciencias Geológicas

DIEGO RENATO CÁRDENAS CÁRDENAS
CONCEPCIÓN-CHILE
2024

Profesor Guía: Gonzalo Montalva Alvarado
Dpto. de Ingeniería Civil, Facultad de Ingeniería
Universidad de Concepción

AGRADECIMIENTOS

A Cristina y Renato, por ser mi inspiración para perseguir mis sueños, y su apoyo incondicional durante esta etapa. A Fanny y Hugo, mis padres, quienes siempre me han guiado y acompañado a lo largo de todos mis retos, a mis hermanas Priscila y Milvia, y a Dios.

A Gonzalo, quien aparte de ser mi tutor, se convirtió en un buen amigo, y creyó en mi capacidad como investigador desde el primer día en que llegué a la UdeC.

A María Esperanza Aravena por su enorme colaboración y apoyo. A los profesores del Departamento de Ciencias de la Tierra (UdeC), especialmente a José Luis Palma por guiarme en los primeros pasos hacia el universo de la programación.

A mis amigos desde siempre, Luchín, Oscar, Daniel, Peter, Chalo, Jaimito, Darío, Milton, por siempre estar ahí, a mis amigos de la cabina 4, Diego José, Fernanda, Bladimir, Adrián, José Tomás, Andrés, los Nicos, Tomás, Cata y demás compañeros con los que compartí durante este periodo.

A la Universidad de Concepción, al Programa de Becas de Doctorado de la Agencia Nacional de Investigación y Desarrollo (ANID) 21190824, y a Núcleo Milenio CYCLO (The Seismic Cycle Along Subduction Zones), financiado por la Iniciativa Científica Milenio (ICM) del Gobierno de Chile beca NC160025, el Fondo de Apoyo al Desarrollo Científico y Tecnológico de Chile (FONDEF) beca ID16I20157, por el apoyo académico, logístico y financiero. A los técnicos de NOC-CEDIA, por el soporte computacional con el manejo del clúster. A la Universidad Central del Ecuador, por concederme el tiempo y las facilidades de mi movilización al extranjero.

A Matt Miller, Sergio Ruiz, Javier Ojeda, Cristian Otarola, Ignacio Pozo, Marcos Moreno por su colaboración en el desarrollo de artículos científicos y críticas constructivas. Y a todas aquellas personas que de una u otra forma colaboraron en la realización de esta tesis doctoral.

¡Gracias Totales!

RESUMEN

Este estudio aborda la reproducción y validación de simulaciones de movimientos fuertes del terreno (*strong-motions)* de banda ancha para grandes terremotos de megathrust (Mw > 7.5) con el fin de mejorar sus predicciones en las regiones cercanas a la fuente sísmica para un amplio rango de frecuencias (0.01 < f < 30 Hz). Se implementó una Simulación Numérica Basada en la Física (PBSs) mediante un enfoque híbrido que combina métodos cinemático y estocástico. Este modelo fue aplicado al Terremoto de Iquique de 2014 (8.2 Mw), incorporando parámetros de modelos de slip co-sísmico heterogéneo, configuraciones de velocidad de la corteza y geometría de una zona de subducción. Las bajas frecuencias (f < 1 Hz) se modelaron utilizando el Método de los Elementos Finitos (3D-FEM) con un mallado en 3D detallado, simulando la ruptura de la fuente sismogénica de manera cinemática, además, se exploraron correlaciones de escalado para el tiempo duración del slip o rotura (*rise time*, Tr), un parámetro temporal crítico en la técnica cinemática, basándose en 45 Modelos de Ruptura de Falla Finita (FFRMs) de grandes terremotos de megathrust (Mw ≥ 7.3), estableciéndose una relación de autosimilitud para el Tr utilizando registros de *strong-motions* y de datos telesísmicos. Para las altas frecuencias (f > 1 Hz), se utilizó una metodología estocástica que incluye FFRMs, evaluaciones de atenuación y respuesta del sitio mediante relaciones espectrales horizontal/vertical (HVSR) para caracterizar la amplificación local. Los resultados de las historias de *strong-motions* híbridos (PBSs) destacan la importancia de integrar la historia de ruptura de la fuente, las condiciones reológicas y las propiedades de atenuación del terreno para reducir las incertidumbres en las evaluaciones de amenaza sísmica. El estudio muestra reducciones en los valores de la desviación estándar de los residuales intra-eventos: hasta un 10.23% en distancias cortas entre fuente-sitio (*rupture-to-station*), primeros ~30 a 70 km, y hasta un 53.9% en el rango de 2 a 100 Hz. Además, se observó una disminución del 50% en valores de diseño para un periodo de retorno de T = 475 años, al comparar las curvas de amenaza sísmica de datos PBSs y ergódicos. La validación del modelo híbrido aplicado al terremoto de Iquique resalta los parámetros críticos que deben considerarse para predicciones más confiables y con menor incertidumbre en futuros terremotos.

ABSTRACT

This study addresses reproducing and validating broadband strong-motions simulations for large-magnitude megathrust earthquakes (Mw > 7.5) to improve their predictions in the near-field region for a broad frequency range (0.01 < f < 30 Hz). Physics-Based Numerical Simulations (PBSs), which encompasses a hybrid approach combining kinematic and stochastic methods. This model was applied to the 2014 Mw 8.2 Iquique Earthquake, incorporating parameters from heterogeneous co-seismic slip models, crustal velocity configurations and geometry of a subduction zone. Low frequencies (f < 1 Hz) were modeled using the Finite Element Method (3D-FEM) with a detailed 3D meshing, simulating the kinematic seismogenic source rupture, also, scaling correlations were explored for the rise time (Tr), a critical time parameter in the kinematic technique, based on 45 Finite Fault Rupture Models (FFRMs) of large megathrust earthquakes (Mw ≥ 7. 3), establishing a self-similarity relationship for Tr using records of strong-motions and teleseismic data. For high frequencies (f > 1 Hz), a stochastic methodology was used, which encompasses FFRMs, attenuation and site response assessments through horizontal/vertical spectral ratios (HVSRs) to characterize local amplification. Results from hybrid strong-motion histories (PBSs) highlight the importance of incorporate seismic source rupture history, rheological conditions, and ground attenuation properties to reduce the uncertainty in seismic hazard analysis. The study shows reductions in the standard deviation values of within-event residuals: to 10.23% in close rupture-to-station distances, first ~30 to 70 km, and up to 53.9% in the range of 2 to 100 Hz. In addition, a 50% decrease in design values for a return period of T = 475 years was observed when comparing the seismic hazard curves of PBSs and ergodic data. The validation of the hybrid model applied to the Iquique earthquake highlights the critical parameters that should be considered for more reliable predictions with less uncertainty in future earthquakes.

ÍNDICE DE CONTENIDOS

ÍNDICE DE FIGURAS

ÍNDICE DE TABLAS

CAPÍTULO I. Introducción general

1.1. Introducción y formulación del problema

En el margen de subducción chilena se han generado grandes terremotos históricos de megathrust con magnitudes Mw > 8.0, por ejemplo: Valdivia 9.5Mw (1960), Maule 8.8Mw (2010), Iquique 8.2Mw (2014), Illapel 8.2Mw (2015) (Ruiz and Madariaga, 2018; Melnick *et al*., 2017), donde se han registrado altos valores de intensidades sísmicas sobre la superficie conocidos como movimientos fuertes del terreno. En el Análisis Probabilístico y Determinístico de Amenaza Sísmica (*Seismic Hazard Assessment* - SHA) para zonas de subducción, se utilizan modelos empíricos de predicción del movimiento fuerte del terreno (Ground Motion Prediction Models - GMPMs) no ergódicos, junto a otra información relevante de fuente, trayectoria y respuesta específica del sitio, para predecir movimientos fuertes del terreno (*strong-motions*) en un sitio específico para futuros terremotos.

Los GMPMs , utilizando datos de eventos sísmicos pasados, predicen el valor medio e incertidumbre de las intensidades espectrales superficiales (IM_{pred}) dentro del rango de frecuencias de importancia para las obras de ingeniería (0.01Hz a 30Hz), desde grandes rascacielos hasta edificios habitacionales y viviendas (Morales, 2016), y se obtienen como una convolución lineal de funciones que se basan en parámetros que describen las contribuciones de la fuente sísmica, la trayectoria y los efectos del sitio que ocurren como resultado de un terremoto, y corresponden a magnitud, distancia fuente-sitio, estilo de falla, condiciones del sitio, más una desviación estándar (Lee *et al*., 2020; Paolucci *et al*., 2018; Al Atik *et al*., 2010). Los GMPMs, debido a su bajo costo computacional son un ingrediente importante dentro del SHA. No obstante, en la región del campo cercano, es decir, en las mínimas distancias entre la ruptura de la fuente sismogénica y el sitio de la estación (*station-to-rupture* - R_{rup}), $R_{rup} < 70$ km, para escenarios de zona de subducción (megathrust) se tiene poca disponibilidad de registros para generar un modelo GMPM que considere la física compleja del fenómeno adecuadamente. Esta falta de registros puede causar un error importante en la estimación de

strong-motions en el campo cercano (i.e., duración y contenido de frecuencia). Estimaciones actuales, basadas en GMPMs, proporcionan resultados bastantes confiables cuando se tiene una distancia estación-fuente suficientemente larga, al menos igual de larga que el tamaño de la fuente, esto describe las principales debilidades de un modelo GMPM (Stupazzini *et al*., 2020; Paolucci *et al*., 2018) particularmente en escenarios como la subducción chilena (Figura 1.1.).

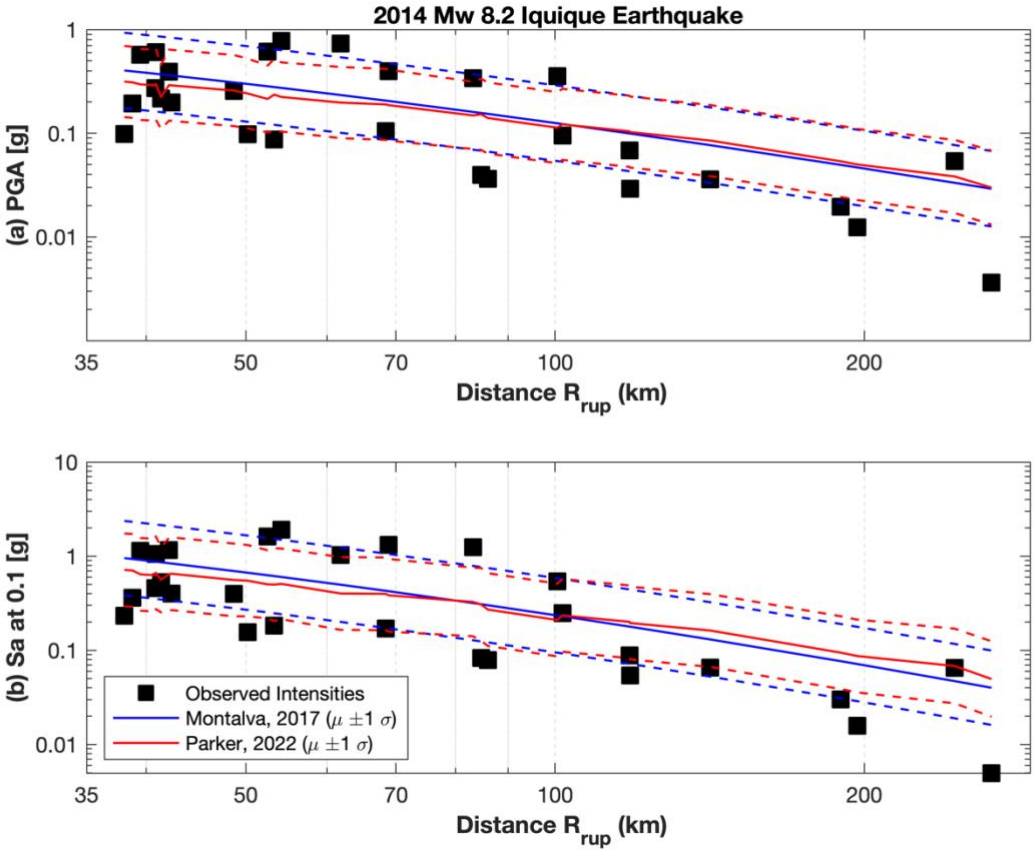

Figura 1.1. Distribución de las IM_{obs} comparadas con la distancia station-to-rupture (R_{rup}), contrastadas con los GMPMs de Montalva et al. (2017) y Parker et al. (2022); para el Terremoto de Iquique Mw 8.2 de 2014. (a) Peak Ground Acceleration - PGA [g], (b) Spectral Acceleration - Sa a 0.1 [g].

Considerando las debilidades que pueden presentar los moldeos GMPM, anteriormente puntualizadas, el modelamiento numérico de terremotos se ha vuelto necesario para una mejor la comprensión del mecanismo de propagación de ondas sísmicas, las características de los movimientos fuertes del terreno, y como un complemento o un substituto de datos registrados (Taborda and Bielak, 2014). La disponibilidad cada vez mayor de capacidad computacional de

alto rendimiento, ha permitido que las Simulaciones Numéricas Basadas en la Física (*Physics-Based Numerical Simulations* - PBSs) se estén convirtiendo en una de las herramientas de vanguardia para el cálculo de *strong-motions*. Estas PBSs permiten obtener *strong-motions* sintéticos representativos, y pueden ayudar a incrementar ampliamente el número limitado de observaciones que se tiene en regiones del campo cercano para terremotos de larga duración (McCallen *et al*., 2021). Cuando la distancia R_{rup} es muy corta (campo cercano), y su fuente tiene un área bastante grande con una distribución compleja de desplazamientos (e.g., megathrust de zona de subducción), el uso de modelos PBSs resulta una herramienta útil para la predicción de *strong-motions* (Stupazzini *et al*., 2020; Paolucci *et al*., 2018; Taborda and Bielak, 2014).

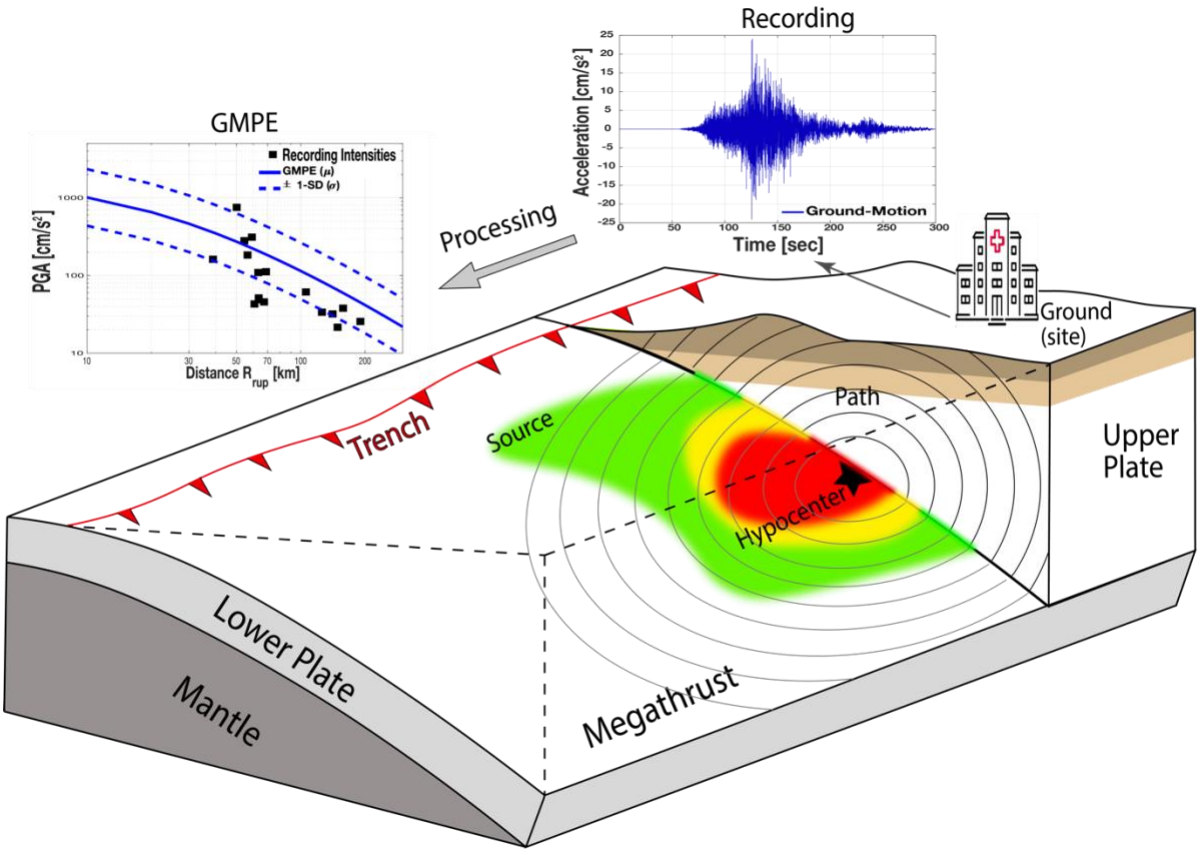

Figura 1.2. Diagrama que indica la ruptura de la fuente sismogénica de un megathrust y la subsecuente propagación de ondas sísmicas, indicando la problemática planteada.

En el presente trabajo se considera la problemática de la evaluación de la demanda sísmica en escenarios de campo cercano (*near-field)* para la zona de subducción de Chile (*i.e.*, megathrust, ver Figura 1.2); donde se considera una metodología híbrida de banda ancha para obtener los *strong-motions* en el rango de frecuencias de interés de obras de ingeniería desde grandes edificios hasta viviendas habituales (0.01 Hz a 30 Hz), donde para las bajas frecuencias (f < 1 Hz) se utilizó una metodología determinística (McCallen *et al*., 2021; Taborda and Bielak, 2014; Aagaard *et al*., 2010), y para las altas frecuencias (f > 1 Hz) se aplicó una técnica estocástica (e.g. Ojeda *et al.*, 2021; Ruiz *et al*., 2018, Ghofrani *et al*., 2013; Motazedian and Atkinson, 2005), para posteriormente unir sus resultantes en una sola historia de tiempo de banda ancha (Bradley *et al*., 2017; Skarlatoudis *et al*., 2015; Graves and Pitarka, 2016; 2015; 2010; 2004), donde los acelerogramas sintéticos de banda ancha, que incluyen las técnicas cinemática y estocástica, obtenidos dentro de este trabajo son denominados como PBSs.

1.2. Hipótesis

Considerando los antecedentes expuestos se desprenden dos preguntas científicas:

- *Factores de Fuente y de Trayectoria: ¿Pueden ser separados linealmente a distancias cercanas en eventos de megathrust?*

- *¿Las simulaciones numéricas basadas en la física podrían ayudar en la mejora de la predicción de las intensidades de los movimientos del terreno (strong-motions) para sitios cercanos a la zona de subducción?*

A partir de lo cual, se propone la siguiente hipótesis:

La predicción de intensidades sísmicas sobre la superficie del terreno en escenarios extremos (cercanos al megathrust), obtenida del análisis probabilístico, no representa adecuadamente la interacción entre los efectos de la fuente y los mecanismos de amplificación

geológica. Estos pueden identificarse en simulaciones numéricas de la física del fenómeno. Una combinación de ambos modelos permitirá una mejora en la confiabilidad de la evaluación del peligro sísmico.

1.3. Objetivos

1.3.1. Objetivo General

Mejorar el análisis probabilístico de la demanda sísmica de los movimientos en la superficie, mediante la aplicación de límites físicos de sus parámetros en escenarios extremos, integrando un modelo que considere la ruptura dinámica, la trayectoria de ondas en la corteza, y los efectos de la geología, en zonas cercanas al megathrust.

1.3.2. Objetivos Específicos

1. Evaluar las posibles distribuciones espaciales del deslizamiento (slip) en la ruptura de un megathrust.
2. Mejorar los efectos de amplificación del sitio incorporando parámetros de decaimiento espectral y relaciones de ondas H/V.
3. Validar el modelo numérico mediante análisis de la variabilidad de los residuales que presentan los *strong-motions* de banda ancha (PBSs) obtenidos a través de la metodología híbrida, con métodos empíricos, para eventos de subducción.

1.4. Organización de los resultados

Los resultados del presente trabajo están desarrollados en cuatros capítulos. En el primero de ellos se muestra la problemática de la investigación y la formulación del problema. Con esta información se plantea la hipótesis y los objetivos del trabajo, así como un resumen de las principales metodologías utilizadas para el desarrollo y cumplimiento de dichos objetivos. A continuación, en los capítulos 2 y 3 se presentan dos artículos científicos enviados a revistas

indexadas (WoS), donde se desarrollan los principales resultados de la tesis según los objetivos expuestos en el apartado anterior.

En el capítulo 4 se presenta una síntesis y discusión general donde se integran los principales resultados obtenidos en los artículos desarrollados y finalmente en el capítulo 5 se destacan las conclusiones de la presente tesis de doctorado.

1.5. Metodología

Para el desarrollo de los objetivos planteados, se describen brevemente las distintas metodologías empleadas, tomando como caso de estudio el Terremoto de Iquique ocurrido 01 de abril de 2014 registrando una magnitud de $8.2M_w$, para la validación de los *strong-motions* que se van a modelar numéricamente, evento cuyo comportamiento de slip co-sísmico ha sido estudiado previamente (Schurr *et al.*, 2014; Hayes *et al*., 2014; Ruiz *et al*., 2014), y además, existen registros acelerográficos del evento, registradas en 28 estaciones ubicadas en un rango de 38 km a 140 km de distancia entre hipocentro y estación (Bastías and Montalva, 2016). Los detalles específicos se abordan en el cuerpo de los siguientes dos capítulos.

1.5.1. Adquisición de datos

Los datos de acelerogramas e intensidades instrumentales registradas se obtuvieron de la base de datos de Bastías and Montalva (2016). Los parámetros de modelos de slip cosísmico heterogéneo se adquirieron de Schurr *et al.* (2014); Hayes *et al.* (2014) y Ruiz *et al.* (2014). La configuración de batimetría y topografía se la derivó a partir de *General Bathymetric Chart of the Oceans* (GEBCO), mientras que, las estructuras del slab y de las capas del interior de la corteza y manto terrestre, se modelaron desde Slab2 (Hayes *et al*., 2018), y Tassara and Echaurren (2012), respectivamente.

1.5.2. Análisis y modelamiento de datos de intensidades símicas

Se analizó y contrastó la información derivada de los acelerogramas que registraron el evento de Iquique 2014 ($8.2M_w$) con dos modelos de GMPM utilizados para zonas de subducción (Montalva *et al.*, 2017; y Parker *et al.* 2022), con la finalidad de evaluar el desajuste entre los datos de aceleraciones espectrales observados y modelados empíricamente, previo a la realización de las PBSs.

1.5.3. Análisis y modelamiento de datos de slip cosísmico y de velocidades sísmicas

Se utilizaron los parámetros del slip cosísmico heterogéneo según el modelo de Schurr *et al.* (2014). Posteriormente, se identificó que para la generación de series de tiempo en bajas frecuencias el *rise-time* o tiempo de duración del slip en su plano de ruptura es un parámetro crítico dentro de la modelación numérica. Razón por la cual, se desarrolló una correlación de escalamiento para obtener el *rise-time* en eventos de megathrust, a partir de regresiones que involucran el área de ruptura de la fuente sismogénica, momento sísmico, área de asperezas y valores promedio de slips. Esta correlación es producto del análisis de 45 modelos de ruptura de falla finita, para sismos de interfase de zona de subducción ocurridos alrededor del mundo.

Para el modelo de velocidades sísmicas del interior de la corteza y manto, se realizaron interpolaciones derivadas de los modelos propuestos por Comte *et al.* (2016), y Gao and Tilmann (2021), con lo que se obtuvieron parámetros valores de velocidades V_S, V_P, y densidad, permitiendo también generar valores de tiempo de ruptura, tiempo de iniciación de la ruptura y velocidad de la ruptura, factores importantes dentro de la simulación numérica.

1.5.4. Generación de malla de elementos finitos

Mediante el software Cubit® se realizó la malla 3D de elementos finitos (3D-FEM) para la zona de subducción donde ocurrió en Terremoto de Iquique 2014 (M_w 8.2), que contiene 4 cuerpos: Corteza Continental, Corteza Oceánica (contiene el slab), Manto Continental y Manto Oceánico, diferenciándose, además, un volumen de slip cosísmico (con mallado gradacional). Los distintos volúmenes y geometría del mallado contienen también datos de batimetría, y reología de los materiales.

1.5.5. Modelación numérica en bajas frecuencias (f < 1 Hz)

Utilizando el código PyLith© (Aagaard *et al.*, 2023a; 2013), se simuló la ruptura de la fuente sismogénica desencadenando la trayectoria de ondas y los desplazamientos en superficie, permitiendo obtener las series de tiempo de los *strong-motions* en bajas frecuencias (f < 1 Hz), en donde, se consideran condiciones de frontera de tipo borde absorbente implementados en PyLith©, para evitar reflexiones espurias durante la propagación de ondas sísmicas hacia el interior del dominio de análisis.

1.5.6. Modelación estocástica en altas frecuencias (f > 1 Hz)

Aplicando la técnica descrita y utilizada por Ojeda *et al.*, (2021); Ruiz *et al*., (2018) y Otarola and Ruiz, (2016), se generaron las series de tiempo de los *strong-motions* en altas frecuencias (f > 1 Hz), donde el modelo de falla finita del megathrust con sus correspondientes slips para cada subfalla, se lo desarrolló interpolando el modelo Slab2 (Hayes *et al.*, 2018) con los parámetros de slip propuestos por Schurr *et al.* (2014).

1.5.7. Generación de series de tiempo de banda ancha

Realizando un *match-filtering* (Graves and Pitarka, 2010; 2004; Kamae *et al.*, 1998; R. Graves, 2023 personal communication) en el dominio de las frecuencias, se unieron las series de tiempo en bajas y altas frecuencias generando series de tiempo de *strong-motions* de banda ancha, utilizando un filtro Butterworth de segundo orden, con un intervalo de emparejamiento comprendido entre 0.75 a 1.1 Hz, y posteriormente se evaluó su desajuste con las señales registradas.

CAPÍTULO II. Subduction Interface Earthquake Rise Time Scaling Relations

Cárdenas, D. R., Miller, M., & Montalva, G. A. (2024). Subduction Interface Earthquake Rise-Time Scaling Relations. *Bulletin of the Seismological Society of America*, *114*(1), 278-290. Available from: https://doi.org/10.1785/0220230422

Abstract

The slip duration in a fault plane, also known as rise time (T_r), is determined in Finite Fault Rupture Models (FFRMs) through the analysis of seismic source inversions using strong ground motion records and teleseismic data. For subduction interface earthquakes (megathrust), models exist that provide estimates for T_r values. The SRCMOD and NEIC databases include FFRMs that allow for the extension of source-scaling relations. Currently, T_r versus seismic moment (M_0) scaling relations specifically derived for large megathrust earthquakes in the near-source region are scarce. The relationship between stress drop and M_0 is not straightforward, thus the logarithmic distribution of stress drop among earthquakes of different magnitudes (M_W) appears to be constant or self-similar. This self-similarity refers to a symmetry of the time-dependent fields, which remain unchanged under certain scale transformations in space and time characterized by similarity exponents and a function of the scaled variable, called the scaling function. In this study, T_r scaling has been conducted using 45 FFRMs derived from large megathrust earthquakes ($M_W \geq 7.3$) obtained from the previously-mentioned databases. The scaling relation derived from the FFRMs based on strong ground motion records closely approximates $\log(T_r) = \text{const} + 1/3\log(M_0)$, which agrees with the self-similarity assumption for earthquake ruptures. On the other hand, the scaling relation obtained from the teleseismic dataset exhibits a smaller slope, indicating that the teleseismic data may overestimate source time characteristics when compared to strong ground motion data from seismic stations located close to the source.

2.1. Introduction

In previous years, significant efforts have been made to develop Finite Fault Rupture Models (FFRMs) for both recent and historical megathrust earthquakes (Mai and Thingbaijam, 2014), as well as scaling relations that allow for the estimation of important source characteristics such as rupture area and average slip. Scaling relations have been specifically developed for events occurring on shallow crustal faults (e.g., Somerville *et al*., 1999; Prieto *et*

al., 2004; Blaser *et al*., 2010; Leonard, 2010; 2014; Strasser *et al*., 2010), as well as for megathrust events (Murotani *et al*., 2008; Strasser *et al*., 2010; Murotani *et al*., 2013; Skarlatoudis *et al*., 2016; Allen and Hayes, 2017). The FFRMs adopt rectangular subfault source configurations in a total area typically larger than the effective rupture area, where each subfault encompasses an average slip, seismic moment, and the time it takes for a slip at a particular point on the fault to reach its final value (rise time; T_r).

The scaling of seismic source parameters in heterogeneous slip distribution models provides essential information for understanding their physical characteristics (e.g., Murotani *et al.,* 2008). The selected FFRMs used in this study were mostly obtained from teleseismic waveform inversions from strong ground-motion (SGM) inversions, a combination of both, and occasionally combined with geodetic data as Global Navigation Satellite System (see Table 2.1). In these FFRMs, certain subfault zones contain slip values higher than the D within the S; these subfault zones are referred to as asperities in this work. It is hypothesized that asperities within the S have an influence on ground-motion characteristics (Murotani et al., 2008).

In the conventional self-similarity approach, the source parameters for earthquake rupture processes are analyzed to obtain scaling relations; these kinematic parameters (e.g., seismic moment, fault area, slip, rise time, rupture velocity) are part of the FFRMs (Herrero and Bernard, 1994; Somerville *et al*., 1999; Leonard, 2010). These scaling relations operate under the assumption that an increase in the seismic moment (M_0) is accompanied by proportional changes in average slip, D, and in rupture area, S, (i.e., length L and width W) so that the average stress drop remains constant. Furthermore, the slip duration on the fault (rise time, T_r) is assumed to increase proportionally with D to ensure a constant slip velocity. For megathrust earthquakes (i.e., $M_W > 7.0$) many seismological studies have estimated slip distributions using FFRMs, deriving scaling relationships between seismic moment (M_0), fault area, fault length (L), and fault width (W). However, to date, no established relationships have been obtained for rise time (T_r).

In broadband strong ground motion simulations for future large earthquakes, the rise time (T_r) is considered a crucial parameter within the deterministic approach. This is because the earthquake source is characterized by a kinematic description of the spatially varying dislocation (slip) across the entire fault rupture area, thus incorporating both rise time and rupture velocity (Liu *et al.*, 2006; Ichinose *et al.*, 2007; Graves and Pitarka, 2010; 2016; Skarlatoudis *et al.*, 2015). However, rise time is difficult to determine and tabulate for use in deterministic simulations. In fact, only a few FFRMs provide values for T_r and rupture velocity for megathrust events, resulting in epistemic uncertainty due to this lack of data. Typically, T_r estimates obtained when instruments are located very close to the seismic source (i.e., near-source) are considered most reliable. Such instruments record the formation history of the static offset, enabling a more direct estimation of T_r (Gusev and Chebrov, 2019).

Few studies have been conducted on the scaling relationship between T_r and M_0. Somerville *et al.* (1999) derived a scaling law based on fifteen crustal events with magnitudes between M_W 5.6 and 7.2, Gusev and Chebrov (2019) arrived at the same scaling law using 83 crustal events ranging from M_W 5.0 to 8.5. In contrast, Melgar and Hayes (2017), determined the scaling law by analyzing 153 earthquakes with magnitudes ranging from M_W 6.8 to 9.1, of which 72 correspond to subduction interface events (M_W 7.0 to 9.1). In the subsequent sections, we present an analysis of source parameter characteristics (e.g., D, S, M_0, T_r) for 45 FFRMs associated with 23 megathrust earthquakes (Figure 2.1). These FFRMs were obtained from the SRCMOD database (Mai and Thingbaijam, 2014), the U.S. Geological Survey National Earthquake Information Center (NEIC), and from Ichinose *et al.* (2007); event magnitudes range from M_W 7.3 to 9.2, and the dataset includes both source parameters and the inversion method used (Table 2.1).

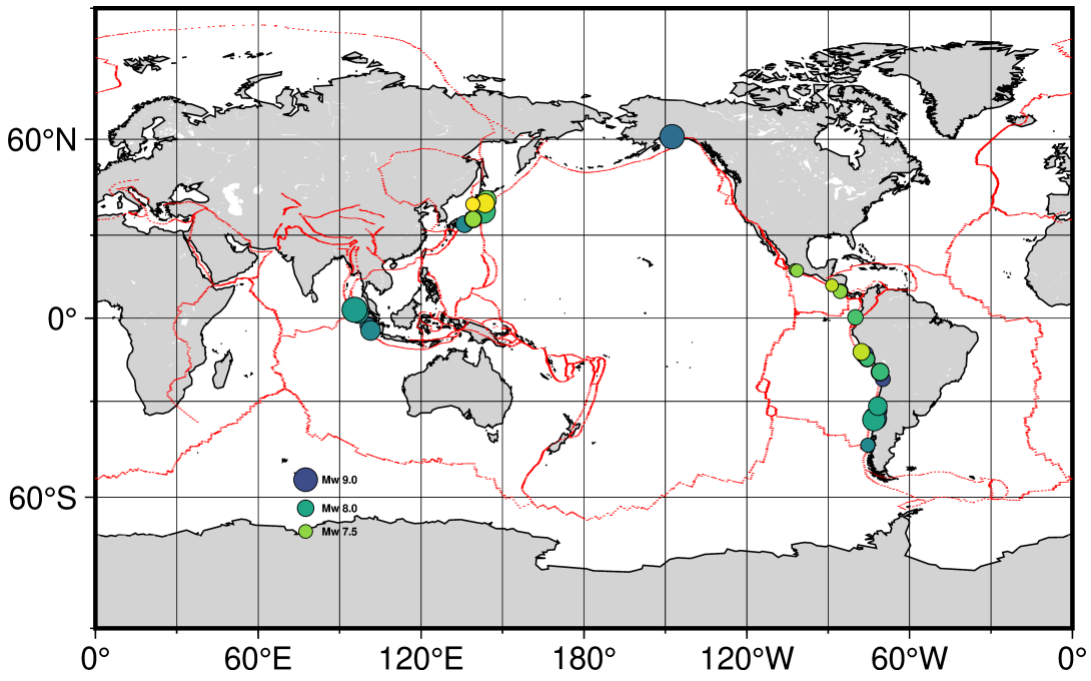

Figure 2.1. Distribution of the megathrust earthquakes listed in Table 2.1. The symbol size indicates event magnitude, while color represents focal depth ranging from shallow (yellow) to deeper (blue) events.

Table 2.1. List of the earthquakes used in the present study and their source parameters (Supplementary @S1).

In this current study, we focus on analyzing FFRMs specifically for subduction interface earthquakes. We characterize the scaling behavior of various parameters, namely the rupture area (S), total asperity area (S_a), and average slip (D), in relation to the seismic moment (M_0). Moreover, we include our main objective of developing a source scaling relationship for T_r as a function of M_0. This relationship holds significant importance in earthquake source physics and has practical applications in strong ground motion simulations and hazard assessment. Within our analysis, we consider asperities as zones with substantial slip values; specifically, we define asperities as areas where slip exceeds 1.5 times the average slip across the entire rupture area (Somerville *et al.*, 1999; Murotani *et al.*, 2008; Skarlatoudis *et al.*, 2016).

Once these relationships are established, by incorporating asperities and rise time within the group of parameters that govern the kinematic seismic source rupture process, it will be

possible to gain a better understanding of the dynamics and behavior of earthquake ruptures. This improved understanding can lead to more accurate simulations and predictions of strong ground motions during megathrust earthquakes, with significant implications for seismic hazard assessment.

2.2. Earthquakes Ruptures and slip models

The recording of great megathrust earthquakes on modern digital seismic networks provides an opportunity to expand the understanding of source-scaling relations for large-magnitude events and place constraints on the potential range of their source parameters (Skarlatoudis *et al.*, 2016). Furthermore, information about the source characteristics of these recent earthquakes includes the spatial distribution of slip and slip velocity on the fault; this information is obtained through inversions of strong ground motion recordings (SRCMOD) and teleseismic data (SRCMOD and NEIC). Strong ground motion data in the near-source region provide more detailed information about the source rupture process during earthquakes, especially for shorter periods (Kurahashi and Irikura, 2011). Meanwhile, teleseismic data inversions provide more of the largest asperities, but, the overall spatial resolution commonly is not sufficient to resolve the source rupture process in detail (Yokota *et al.* 2011).

The slip heterogeneities (asperities) and the slip velocity on the fault rupture surface are considered within the kinematic seismic source rupture process parameters. The temporal component T_r is derived from the rupture velocity (V_r) using the equation $T_r = l / V_r$ (Gusev and Chebrov, 2019), where l represents the the size of the currently slipping fault zone, which is significantly smaller than the complete fault length (i.e., a subfault or group of subfaults). These kinematic parameters are of utmost importance for the accurate prediction of strong ground motions (Skarlatoudis *et al.*, 2016; Graves and Pitarka, 2010; 2016; Liu *et al.*, 2006).

2.3. Source scaling relationships

The seismic moment corresponds to $M_0 = \mu DLW = \mu DS$ (Aki, 1966), in which μ represents the shear modulus (rigidity). According to the basic property of a self-similar system, the distribution of stress drop values among earthquakes of different sizes shows only a minimal variation. This property allows events of different sizes to be distinguished by a scale factor. Within this framework, the seismic moment (M_0) increases in proportion to equal changes in average slip (D), fault length (L), and fault width (W), ensuring that the stress drop in this self-similar system (proportional to the ratio of D to L or W) remains constant. Additionally, the duration of slip on the fault (T_r) increases proportionally to D, L, or W, causing the slip velocity (the ratio of D to T_r) to remain constant. Therefore, in this system there is no characteristic rise time independent of seismic moment (Somerville *et al*., 1999; Melgar and Hayes, 2017; Gusev and Chebrov, 2019).

For the selected Finite Fault Rupture Models, the following four parameters are available for the relations to be self-consistent: rupture area (S), total asperity area (S_a), average slip (D), and rise time (T_r). These parameters were obtained from the SRCMOD and NEIC databases, and from Ichinose *et al.* (2007); and the least-squares method was used for regression analysis. First, we categorized the data based on inversion type, obtaining 12 models derived or including Strong Ground Motion (SGM) recordings, and 33 models acquired from or including teleseismic waveform inversions. In instances where several inversions were available for the same event, these were treated as independent entries. For the 45 total FFRMs, we defined the asperity zones by following the procedure described in Somerville *et al*. (1999) and Murotani *et al*. (2008), which consists of trimming and extracting the areas of major slip from the entire rupture area.

The regression slopes were constrained to yield self-similarity relationships using the least-squares method. The logarithms of S and S_a are proportional to two-thirds of the seismic moment, while the logarithm of D is proportional to one-third of the seismic moment, due to the

logarithmic dependence of earthquake magnitude (M_W) on M_0. The proposed relationships have the form

$$log\ (Y) = log\ (a) + (b) log\ (M_0) + \sigma \quad (2.1)$$

in which Y corresponds to the different source parameters, *a*, *b* are the regression coefficients, and σ denotes the standard deviation. In general, estimates of T_r obtained from SGM recordings tend to be more reliable, especially when the instruments are positioned very close to the earthquake source. The minimum source-to-site distance, that is, the closest strong ground motion station to the source is described as R_{min} (see Table 1). Unfortunately, for megathrust earthquakes FFRMs available in this study, R_{min} values are only provided for 12 models derived mainly from strong ground motion inversions, out of which three have R_{min} > 90 km (i.e., far from the source), nevertheless, the 12 models are included in the regressions. The regression coefficient values, along with their standard deviations, for the regressions from all FFRMs, as well as for the models obtained by distinguishing the SGM and teleseismic data, are listed in Table 2.2

The slopes achieved in the least-squares fit, and the self-similarity, for the total number of FFRMs, and additionally the reduced SGM and teleseismic datasets, are presented below. Figure 2.2 displays rupture area against M_0; next Figure 2.3 illustrates the relationship between the total M_0 with the total area of all asperities, which, at around 0.22 (~ 22%) times the rupture area is close to the results of Skarlatoudis *et al*. (2016). In Figure 2.4, the regression slopes for the average slip are displayed, following the same format. Similarly, Figure 2.5 presents the regression slopes for the rise time. By performing the p-value null hypothesis on the regression slopes for the rupture area, total asperity area, and average slip, it is possible to confirm the statistical representativeness of the regressions resulting from the models used. The estimated p-values are 2.84×10^{-13} (S), 1.39×10^{-10} (S_a), 1.07×10^{-13} (D), and 0.00997 (T_r). These values are notably small, supporting the acceptance of self-similarity representativeness (Murotani *et al*., 2008; Skarlatoudis *et al*., 2016).

Table 2.2. Regression parameters obtained in this study for the total dataset of 45 FFRMs, and additionally for the strong ground motion (SGM) and teleseismic (TELE) sub datasets.

Source Parameter	***a***	***b***	***σ***	***a (s-s)***	***b (s-s)***
Rupture area (S)	1.4674×10^{-6}	0.49	1.69	2.27×10^{-10}	
SGM Rupture area	3.2255×10^{-7}	0.51	1.00	1.64×10^{-10}	2/3
TELE Rupture area	2.0432×10^{-6}	0.48	0.99	2.56×10^{-10}	
Total Asperity area (Sa)	1.7359×10^{-6}	0.45	1.22	4.84×10^{-11}	
SGM Total Asperity area	4.2600×10^{-9}	0.56	1.49	2.93×10^{-11}	2/3
TELE Total Asperity area	3.3957×10^{-6}	0.44	0.86	5.82×10^{-11}	
Average Slip (D)	1.3145×10^{-11}	0.51	1.09	9.57×10^{-8}	
SGM Average Slip	3.5264×10^{-9}	0.41	1.01	1.24×10^{-7}	1/3
TELE Average Slip	8.3147×10^{-12}	0.52	1.03	8.73×10^{-8}	
Rise Time (Tr)	1.6427×10^{-4}	0.22	0.93	6.31×10^{-7}	
SGM Rise Time	4.0843×10^{-7}	0.36	0.27	1.36×10^{-6}	1/3
TELE Rise Time	6.0293×10^{-5}	0.23	0.93	4.73×10^{-7}	

SGM is Strong-Ground Motion data, **TELE** is Teleseismic data, ***a*** is the regression intercept, ***b*** is the regression slope, ***a*(s-s)** and ***b*(s-s)** self-similarity approach, ***σ*** standard deviation.

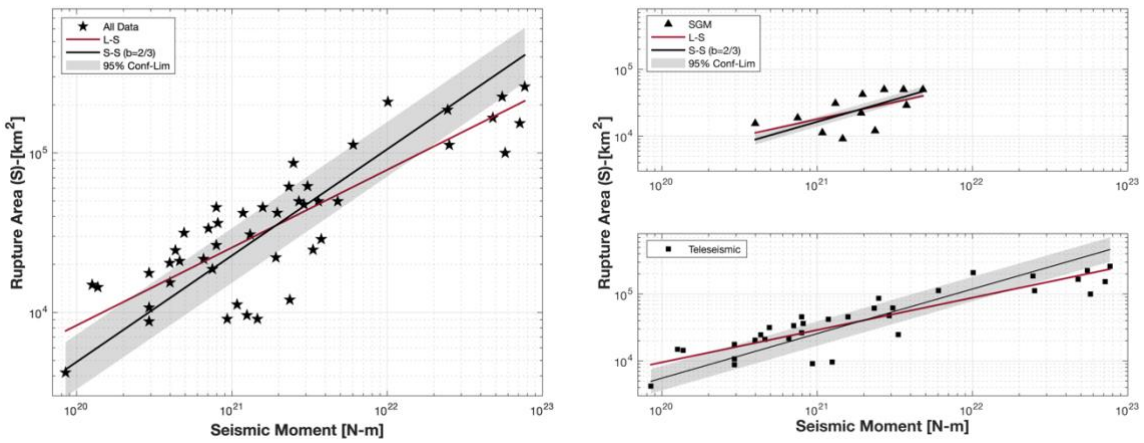

Figure 2.2. Scaling of the rupture area with seismic moment for: all data (left), strong ground motion (SGM) data (upper right), and teleseismic data (lower right). The shaded area indicates the 95% confidence limit interval for the regressions. Lines, red: least-squares (L-S), black: self-similarity (S-S), regressions.

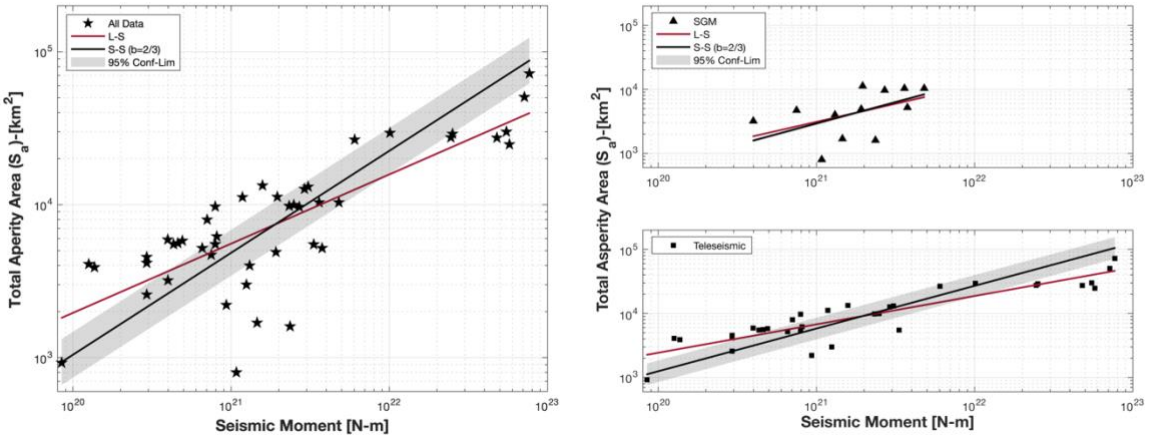

Figure 2.3. Scaling of the total asperity area with seismic moment for: all data (left), strong ground motion (SGM) data (upper right), and teleseismic data (lower right). The shaded area indicates the 95% confidence limit interval for the regressions. Lines, red: least-squares (L-S), black: self-similarity (S-S), regressions.

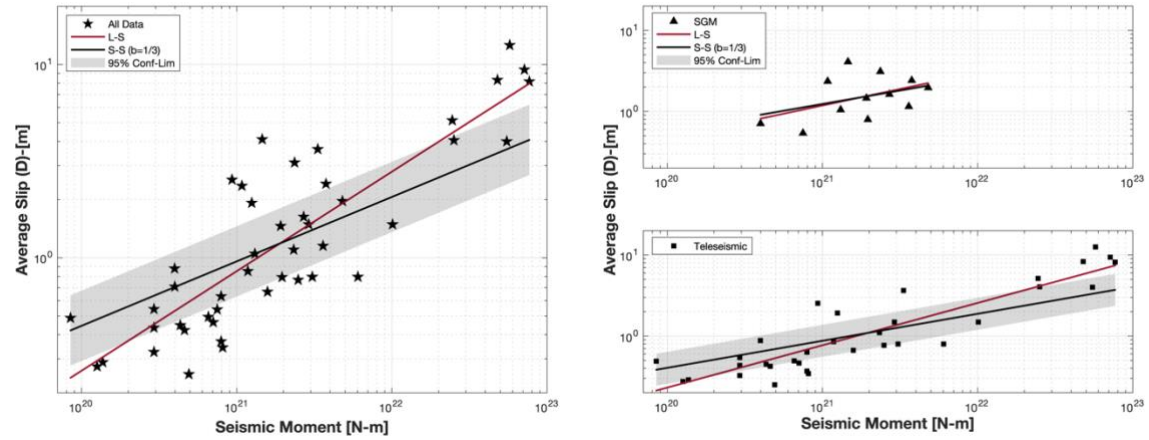

Figure 2.4. Scaling of average slip with seismic moment for: all data (left), strong ground motion (SGM) data (upper right), and teleseismic data (lower right). The shaded area indicates the 95% confidence limit interval for the regressions. Lines, red: least-squares (L-S), black: self-similarity (S-S), regressions.

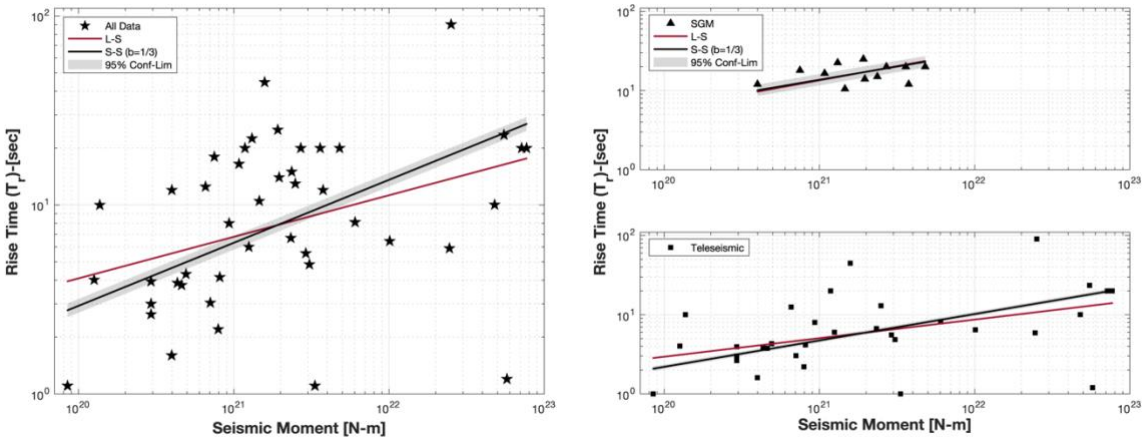

Figure 2.5. Scaling of the rise time with seismic moment for: all data (left), strong ground motion (SGM) data (upper right), and teleseismic data (lower right). The shaded area indicates the 95% confidence limit interval for the regressions. Lines, red: least-squares (L-S), black: self-similarity (S-S), regressions.

The residual analyses presented in Figure 2.6, visually differentiating between the results from the SGM and teleseismic FFRMs, are used to assess the regression quality and identify potential trends within the dataset. The residuals are calculated as ln(observed/predicted), that is, the difference of the natural logarithms between the observed and the regression predicted values (observed values refer to the values reported by each considered study) for the different rupture parameters, S, S_a, D and T_r compared to M_0, and show a general horizontal trend with values close to zero for the range of seismic moments used in this study. Further analysis of the residuals is discussed in the subsequent section.

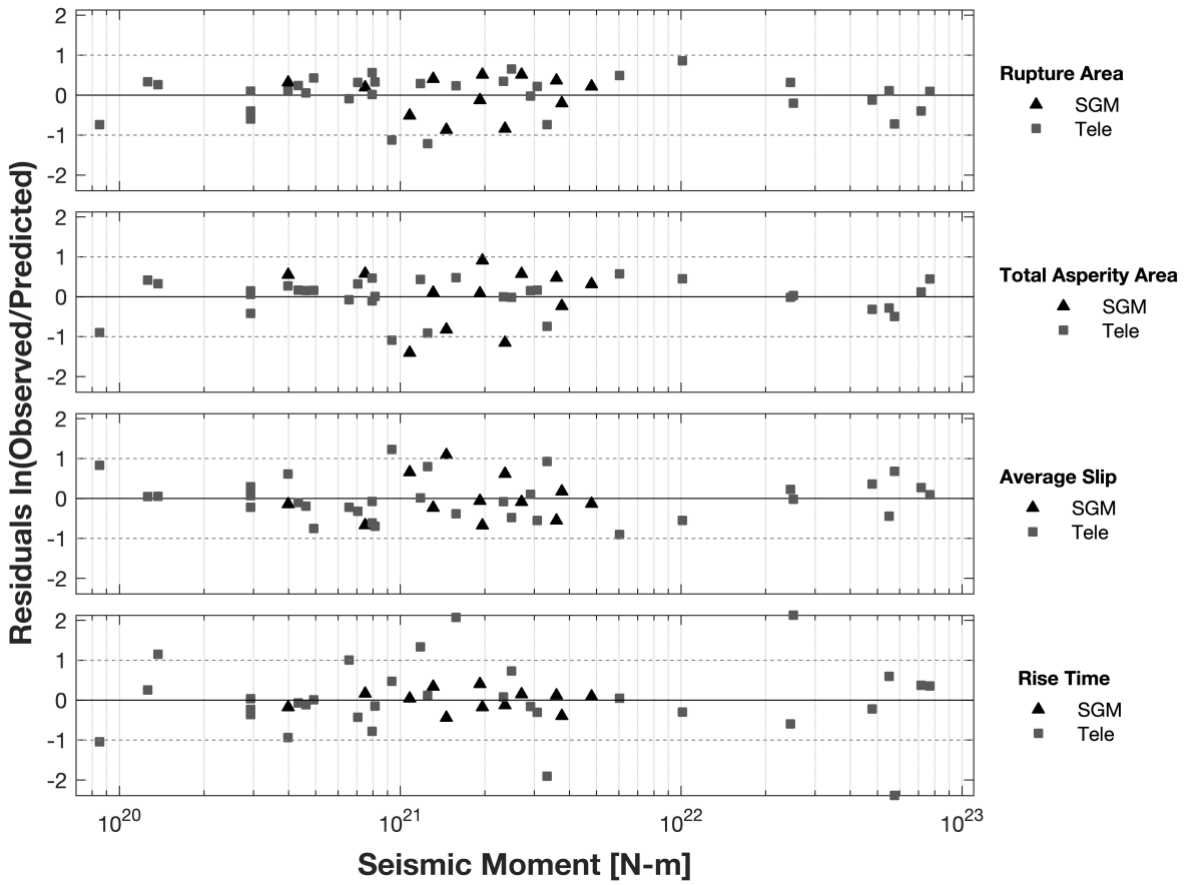

Figure 2.6. Residuals, ln(observed/predicted), plotted against seismic moment for, from top to bottom, respectively: rupture area, total asperity area, average slip, and rise time. The data is differentiated between strong ground motion (SGM - triangles) and teleseismic (TELE - squares) data.

2.4. Discussion

Seismic network spacing (i.e., the spacing between stations and the distance of the closest stations to the fault), and the velocity rupture (V_r), particularly in the case of a super-shear, are important parameters for T_r resolution. For high V_r values and an increase in the spacing between stations, the T_r resolution decreases (Somala *et al.*, 2014). The FFRMs derived from local SGM data used here have close to far distances between stations, nevertheless, these show lower V_r values and consider interface subduction zone environments, thus they are not strongly affected by seismic network spacing, despite having meager SGM network coverage.

FFRMs created with far-field data are capable of resolving the large-scale, low-frequency properties of the rupture model, however, the fine details are sometimes overlooked due to signal attenuation (Yokota *et al*., 2011). Different geophysical datasets can be included in the rupture inversion which are capable of resolving different aspects of the source. Teleseismic and geodetic data can resolve the overall rupture area and slip distribution (Moreno *et al*., 2010), for megathrust events far-field tsunami data can improve the resolution of the shallowest part of the rupture (Yoshimoto *et al*., 2016) which can be further refined by near-field tsunami and marine geodetic observations (Kubota *et al*., 2022). For the whole source process in the spatial and temporal domain, local strong ground motion data is capable of resolving source characteristics that may be otherwise overlooked (Hicks and Rietbrock, 2015). This suggests that if all the data available (e.g., Strong Ground Motion, Teleseismic, Geodetic, and Tsunami) can be combined to perform the inversion, is possible to determine the most suitable source rupture model (Ichinose *et al*., 2007, Yusuke *et al*., 2011), however the Strong Ground Motion records, with their higher frequency content, are fundamental to be able to resolve the shorter duration characteristics. The quantity of rupture models determined by SGM data is still relatively low compared to the size of the overall database. With improved SGM coverage in the future, increased station density, and therefore significantly more SGM rupture models available for study, it will be possible to further refine the rise time parameter scaling relations and determine how the different source inversion techniques can affect this parameter. We stress the importance of SGM networks for subsequent studies to accurately incorporate rise time scaling in broadband strong ground motion simulations for future large subduction earthquakes.

By assuming that the slip of a particle occurs at a constant velocity, the rise time (T_r) will therefore be directly proportional to the displacement (D) of an earthquake (Somerville *et al.*, 1999; Gusev and Chebrov, 2019). Previous studies have suggested that in order to satisfy the self-similarity condition, the regression slope for T_r must be of the order of 1/3 (refer to the *b* values in Table 2.2). However, the regression analysis conducted in this work yielded *b* values of 0.22, 0.36 and 0.23 with standard deviations of 0.93, 0.27 and 0.93, for All data, SGM data,

and teleseismic data, respectively. The SGM dataset slope value is in broad agreement with the findings of Melgar and Hayes (2017) and Gusev and Chebrov (2019) (see Table 2.3). Figure 2.5 depicts the scaling of rise time (T_r) and shows the regression lines for the two subsets of data used in this study. The regression line for the SGM data exhibits a relatively small discrepancy between the least-squares and the self-similarity slope (error ~ 16%), whereas the teleseismic slopes show a slightly larger mismatch (error ~ 34%) than those of the SGM data.

Table 2.3. Regression parameters obtained in this study for the Tr versus Mo relation, for the strong ground motion (SGM) sub dataset, the teleseismic sub dataset, and the total (all data) dataset. Values compared with the previous studies of Melgar and Hayes, 2017 and Gusev and Chebrov, 2019.

Data Source	Data Volume	M_W Range	a	b	σ
SRCMOD/NEIC, SGM	12	7.6 - 8.4	4.08×10^{-7}	0.36	0.27
SRCMOD/NEIC, Teleseismic	33	7.3 - 9.2	6.03×10^{-5}	0.23	0.93
SRCMOD/NEIC, all data.	45	7.3 - 9.2	1.64×10^{-4}	0.22	0.93
Melgar and Hayes (2017)	153	6.8 - 9.1	4.75×10^{-6}	0.29	0.15
Gusev and Chebrov (2019)	83	5 - 8.5	9.31×10^{-7}	0.33	0.33

a is the regression intercept**,** ***b*** is the regression slope, ***σ*** standard deviation.

The intercepts obtained for the regressions of rupture area (S), total asperity area (S_a), and average slip (D), which are denoted as *a* values in Table 2.4, are broadly consistent with findings from other studies that focus on large magnitude earthquakes (e.g., Strasser *et al*., 2010; Murotani *et al*., 2013; Skarlatoudis *et al*., 2016). This agreement holds true for the overall dataset analyzed in this study, as well as for the two separate component subsets examined.

Table 2.4. Regression intercept coefficients and standard deviations for the self-similar scaling relations, for the strong ground motion (SGM) sub dataset, the teleseismic sub dataset, and the total (all data) dataset. Values compared with four previous cited studies.

Data Source	Rupture Area (S)		Total Asperity Area (Sa)		Average Slip (D)	
	a **(s-s)**	$\boldsymbol{\sigma}$	***a*** **(s-s)**	$\boldsymbol{\sigma}$	***a*** **(s-s)**	$\boldsymbol{\sigma}$
SRCMOD/NEIC, SGM	1.64×10^{-10}	1.00	2.93×10^{-11}	1.49	1.24×10^{-7}	1.01
SRCMOD/NEIC, Teleseismic	2.56×10^{-10}	0.99	5.82×10^{-11}	0.86	8.73×10^{-8}	1.03
SRCMOD/NEIC, all data.	2.27×10^{-10}	1.69	4.84×10^{-11}	1.22	9.57×10^{-8}	1.09
Murotani *et al*. (2008)	1.48×10^{-10}	1.61	2.89×10^{-11}	1.78	1.48×10^{-7}	1.72
Strasser *et al*. (2010)*	5.60×10^{-10}	0.3	---		---	
Murotani *et al*. (2013)	1.34×10^{-10}	1.54	2.81×10^{-11}	1.72	1.66×10^{-7}	1.64
Skarlatoudis *et al*. (2016)	1.77×10^{-10}	1.49	4.16×10^{-11}	1.61	1.23×10^{-7}	1.53

The slopes for **S** and $\mathbf{S_a}$ are 2/3, and the slope for **D** is 1/3. ***S** slope is $b = 0.6347$. $\boldsymbol{\sigma}$ standard deviation.

Figures 2.7 and 2.8 show that the fitted slopes for S and S_a are in good agreement with the relationships proposed by Strasser *et al.*, (2010), Murotani *et al*. (2013), and Skarlatoudis *et al*. (2016). The average slip (D) scaling, depicted in Figure 2.4, reveals two notable trends in the least-squares fit when considering the two distinct data subsets. The SGM data exhibits a shallow slope, which could be attributed to the fact that all 12 earthquakes modeled from the SGM data have slip values larger than 1 meter (ranging from 1.83 to 7.82 meters), reducing the span of seismic moments over which the regression analysis is conducted. Also, the SGM data display a slope that aligns better with the self-similarity trend. In Figure 2.9, it is noteworthy that the slip values obtained with the models of Murotani *et al*. (2013) and Skarlatoudis *et al*. (2016) appear slightly larger than the values obtained in this present study, suggesting a potential overstimation of the average slip for subduction interface events (i.e., they would overestimate the seismic demand).

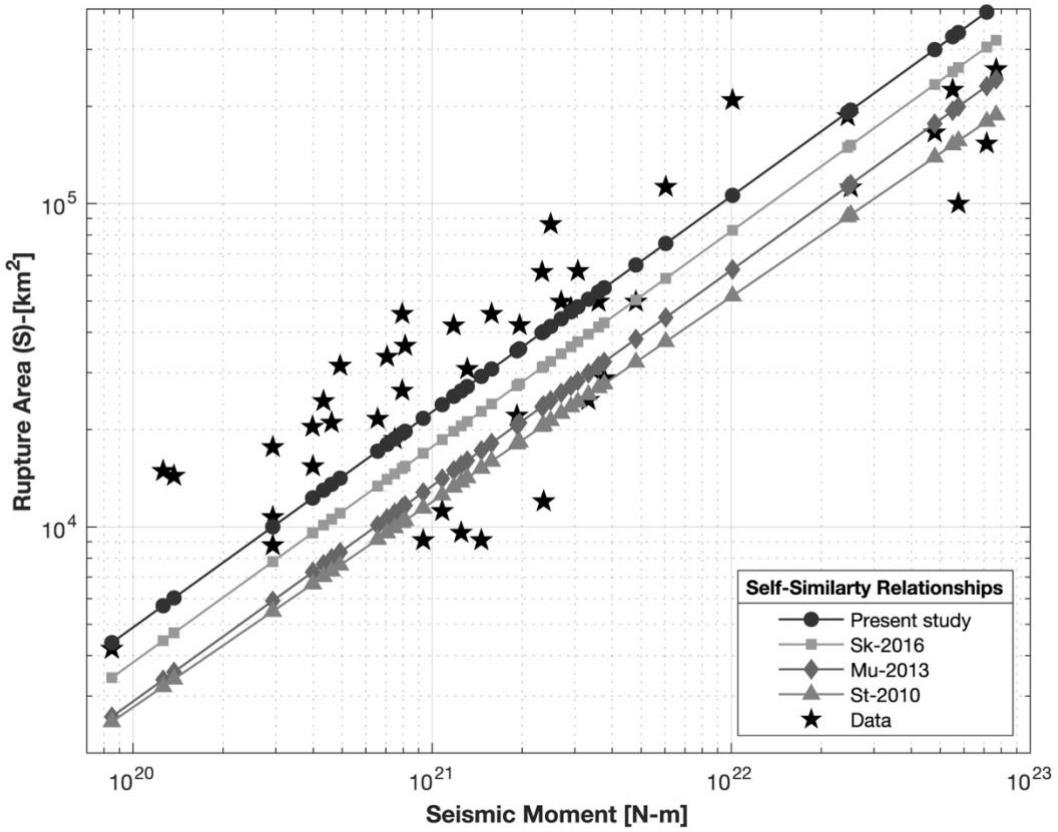

Figure 2.7. Scaling of rupture area against the seismic moment plotted alongside relations from various studies for megathrust environments, following the self-similarity approach: Sk-2016, Skarlatoudis et al., 2016, Mu-2013, Murotani et al., 2013 and St-2010, Strasser et al., 2010.

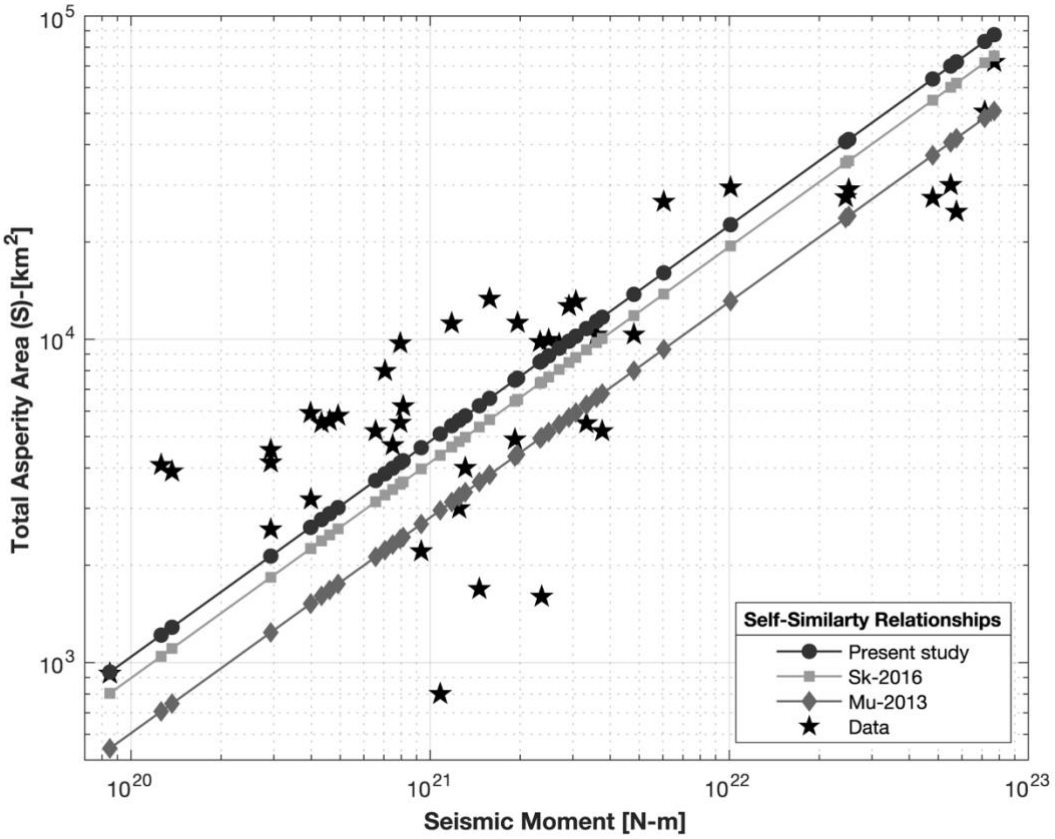

Figure 2.8. Scaling of total asperity area against the seismic moment plotted alongside relations from various studies for megathrust environments for which this parameter is available, following the self-similarity approach: Sk-2016, Skarlatoudis *et al*., 2016, Mu-2013, Murotani *et al*., 2013.

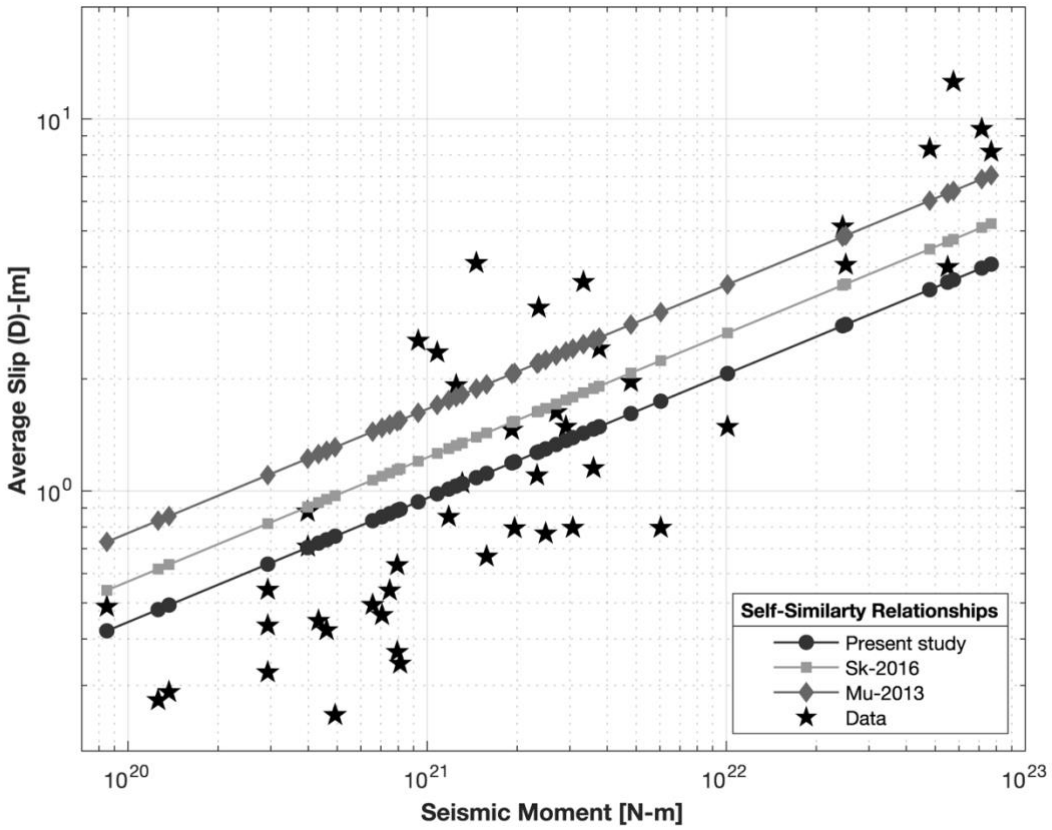

Figure 2.9. Scaling of total asperity area against the seismic moment plotted alongside relations from various studies for megathrust environments for which this parameter is available, following the self-similarity approach: Sk-2016, Skarlatoudis *et al*., 2016, Mu-2013, Murotani *et al*., 2013.

The comparison of studies regarding the rise time (T_r), as presented in Figure 2.10, reveals only a slight difference between the slope obtained in this study and that of Melgar and Hayes (2017), who included both megathrust earthquakes and crustal events in their dataset. In contrast, there is a notable disparity between the best-fit slope found in this present study and that of Gusev and Chebrov (2019), since the latter study used only crustal earthquakes with magnitudes up to 5.5, while the present study concentrates on megathrust events with magnitudes starting at M_W 7.3.

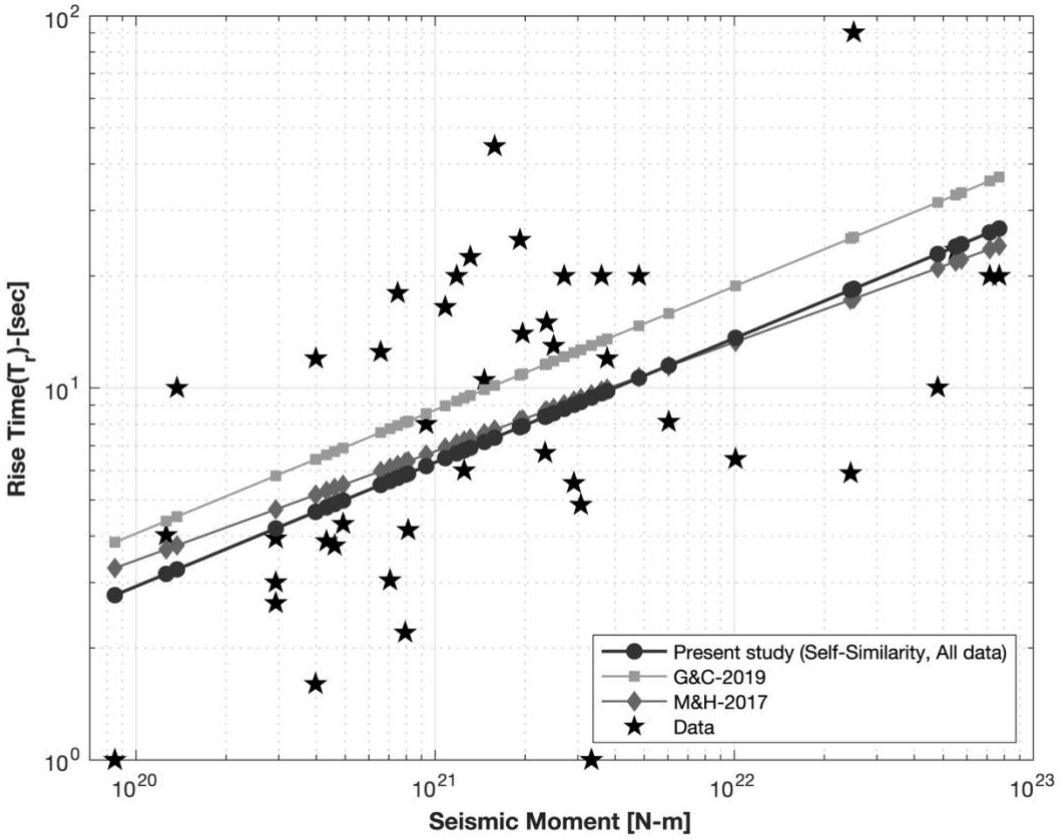

Figure 2.10. Scaling of resulting rise time (self-similarity, all data) against the seismic moment, plotted alongside relations from other related studies: G&C-2019, Gusev and Chebrov, 2019, M&H-2017, Melgar and Hayes, 2017.

The residual analysis presented in Figure 2.6, which plots the log-scale difference of the observed - predicted values against M_0, examines potential trends in the quality of the regression within the dataset. For the rupture area (S), total asperity area (S_a), average slip (D), and rise time (T_r) parameters, the residuals do not exhibit any significant trends across the range of seismic moments considered in this study; this suggests that for the studied range of moments the proposed model is unbiased. Furthermore, the residuals show a constrained range of values around ± 2 for all parameters, this is comparable with the residual analyses obtained in the regressions for S, Sa, and D scaling relations in subduction interface earthquakes showed in Skarlatoudis et al. (2016), where all its residual values fit around ± 1. Notably, for higher values

of M_0 corresponding to the largest magnitudes, the residuals tend to be closer to zero, particularly for the parameters of S, S_a, and D. Another remarkable feature that can be observed regarding the rise time (T_r) residuals is that the subset of data from SGM analysis has noticeably lower residuals compared to the dataset derived from the teleseismic data analysis.

2.5. Conclusions

In this study, we have analyzed a database of worldwide subduction interface earthquakes with magnitudes ranging from 7.3 to 9.2. For each earthquake, we have evaluated all available rupture models containing the rise time parameter, and, subsequently, performed further regression analysis on subsets of data based on whether the rupture models were derived from strong ground motion (SGM) or teleseismic data. The regression analysis of the SGM dataset revealed that the slope (*b*) versus the average slip (D) does not significantly deviate from the expected value of 1/3 for the ideal case of self-similarity scaling. This is a result consistent with previous studies conducted on megathrust environments. Furthermore, the regression self-similarity parameters for rupture area (S) and total asperity area (S_a) closely match those reported in previous works, especially concerning the intercept (*a*) and standard deviation (σ).

The rise time (T_r) values examined in this study focus specifically on large-magnitude subduction zone earthquakes. Our findings indicate that the rise time values tend to be relatively shorter for rupture models derived from teleseismic data, with slightly longer values observed for models derived from strong ground motion data. In contrast, case studies of crustal earthquakes covering a range of magnitudes M_W ~5.0 – 8.5 (Somerville *et al.* (1999)) calculate T_r values shorter than their equivalent-magnitude subduction interface events. Similarly, studies focusing on crustal earthquakes with magnitudes limited to only M_W 5.5, Gusev and Chebrov (2019), also show shorter rise time values.

The T_r slope value (*b*) obtained for the strong ground motion (SGM) regression in our study is 0.36 with an accuracy of approximately 16%; this aligns with the T_r slope values of Gusev and Chebrov (2019), with b = 0.33, and Melgar and Hayes (2017), with b = 0.29. However, our analysis of T_r using only teleseismic data reveals a smaller slope value of b = 0.23. Also, teleseismic stations are located at much greater distances from the earthquake source compared to local SGM stations, which can lead to greater attenuation effects in the seismic waves showing a lower slip resolution, increasing source rupture duration (Yokota *et al.* 2011; Kurahashi and Irikura, 2011), also reported by Gusev and Chebrov (2019). This indicates that teleseismic-data-only inversions may tend to overestimate the source time characteristics when compared to high-frequency strong ground motion data from seismic stations situated close to the earthquake epicenter.

The quantity of rupture models determined by SGM data is still relatively low compared to the size of the overall database. With improved SGM coverage in the future, increased station density, and therefore significantly more SGM rupture models available for study, it will be possible to further refine the rise time parameter scaling relations and determine how the different source inversion techniques can affect this parameter. We stress the importance of SGM networks for subsequent studies to accurately incorporate rise time scaling in broadband strong ground motion simulations for future large subduction earthquakes.

The differences observed between this present study and that conducted by Melgar and Hayes (2017), in terms of T_r values obtained by employing the scaling relationship, are relatively small, typically on the order of a few seconds. This suggests that the T_r scaling employed in our study can be effectively applied to large-magnitude earthquakes and that the current uncertainty between different rise time models does not overly affect source rupture models for megathrust events. In conclusion, the results presented herein reinforce studies on the application of scaling relations and confirm their suitability for application to large-magnitude subduction interface earthquakes.

CAPÍTULO III. Hybrid Broadband Strong-Motions Uncertainties Simulations in the Near-Field Megathrust Earthquakes.

Cárdenas, D., Montalva, G., and Ruiz S. (2024). *Bulletin of the Seismological Society of America*. Manuscrito enviado.

Abstract

Reproducing and validating broadband strong-motions simulations for great megathrust earthquakes (M_w>8.0) is a crucial step to reduce uncertainty in intensity predictions in the near-field and high-frequency range. Several authors have proposed hybrid simulation techniques to obtain broadband time series in seismic environments, capturing the physical process involved in the source rupture, and the waves propagation. These simulations include the path and the site conditions and consider Physics-Based Numerical Simulations (PBSs) techniques. We examined the 8.2 M_w Iquique earthquake, recorded in seismological stations located in the near-field region. We compared these records with simulated ones using a hybrid approach to obtain broadband strong-motions in the three-components at the frequency range of engineering interest. Both Low and High frequencies are based on a heterogeneous slip model and a crustal velocity model. Low frequencies are computed using a kinematic approach through the Finite Element Method (FEM), using scaling relationships to determine the necessary physical parameters. High frequencies are obtained by employing a stochastic method. The attenuation assessment includes different kappa (κ) values for each station. Additionally, due to the scarcity of empirical transfer functions for our stations, we calculated the horizontal-to-vertical spectral ratios (HVSR) to evaluate the site amplification behavior. The broadband time series obtained by combining source rupture history, attenuation characteristics, and adequate site responses over the entire frequency engineering interest spectrum can reproduce and improve the strong-motions predictions in the near-field environments controlled by large-magnitude earthquakes.

3.1. Introduction

Chile is one of the countries with the highest seismic activity in the world. Large-magnitude earthquakes Mw ≥ 7.5 occur frequently, in the last 15 years took place the Maule 2010, Mw8.8; Iquique 2014, Mw 8.2; Illapel 2015, Mw 8.3 and Chiloé 2016, Mw 7.6 (Ruiz and Madariaga, 2018; Melnick *et al.*, 2017). During these earthquakes, high-intensity values were registered, and serious structural damage were observed (Astroza et al., 2012; Montalva and Chávez-Garcia, 2016; Becerra et al., 2016; Fernandez et al., 2017). The instrumental intensity

measures (IM_{obs}) are directly proportional to the damage degree that the earthquake is capable (Silva *et al.*, 2020). In Probabilistic and/or Deterministic Seismic Hazard Analyses (SHA) for subduction zones, the use of empirical ground-motion prediction models (GMPMs) is an important part of the SHA, predicting the needed IM at a specific site. The GMPMs involve both probabilistic and deterministic criteria using data from past seismic events return the median predicted value of the surface spectral intensities (IM_{pred}), and are obtained as linear convolutions of functions based on a limited number of relevant parameters such as magnitude, the source-to-site distance, the faulting style, the site-conditions, plus a standard deviation, parameters that describe the contributions of seismic source, path, and site-effects that occur as a result of an earthquake (Lee *et al*., 2020; Stupazzini *et al.*, 2021; Paolucci *et al*., 2018a; 2015; Rodriguez-Marek *et al*., 2011; Atik *et al*., 2010), a simplified scheme of how they are obtained is shown in Figure 1.2. Nevertheless, the GMPMs models in the near-field region for subduction megathrust earthquakes present some weaknesses described below.

Contrasting the strong-motions registered intensities (IM_{obs}) during the earthquake (*i.e.*, PGA and Sa at 01. [g]) with the station-to-rupture distance (R_{rup}) for the 2014 Mw 8.2 Iquique earthquake, from two GMPMs models (Montalva *et al*., 2017; and Parker *et al*., 2022) as is shown in Figure 1.1, it can be seen that IM_{obs} exceed ± 1 standard deviation from the prediction model mostly in the first 30 to 70 km from the source.

The total residual (Δ) of a GMPM corresponds to $\Delta = Ln(IM_{obs}) - Ln(IM_{pred})$ permits analyze the variability of resulting predicted values, the total residuals can be decomposed in between-event (δB_e) and within-event (δW_{es}) residuals (Rodriguez-Marek *et al*., 2011; Atik *et al*., 2010), the general form is given by:

$$Ln(IM_{obs})_{es} = \mu_{es} + \delta B_e + \delta W_{es} \quad (3.1)$$

where μ_{es} is the median ground-motion model, and the subscripts *e* and *s* refer to "event" and "station," respectively. The between-event residual represents the average shift of the observed

ground motion from an individual earthquake, *e*, from the population median predicted by the ground-motion model. The within-event residual is the misfit between an individual observation at station *s* from the earthquake-specific median prediction, which is defined as the median prediction of the model plus the between-event term for earthquake *e* (Atik *et al.*, 2010). Residuals analysis is helpful to show how the behavior of spectral predicted intensities IM_{pred} with the period or frequency, with this aim, the within-event residuals (δW_{es}) were obtained and evaluated with the frequency (Figure 3.1) where exists a remarkable variability for high frequencies (~1 to 100 Hz) or short periods (~1 to 0.01 s), additionally, when contrasting δW_{es} residuals against the station-to-rupture distance (R_{rup}) a prominent misfit between the residuals and the ±1 standard deviation of the IM_{obs} data for each event is exhibited in the first ~30 to 70 km (Figure 3.2).

Based on the above, megathrust earthquakes (Mw>8.0) tend to generate a high variability between spectral intensities (IM_{pred}) from conventional models (*i.e.* GMPMs) and measured intensities (IM_{obs}) in the near-field distances (*i.e.* 30 to 70 km; distance station-to-rupture). Furthermore, a remarkable misfit in the within-event residuals values is evident for the high frequencies (1 to 100 Hz) or short periods (0.01 to 1 s). The high variability trends for intensities and residuals values are key issues that reflect the principal uncertainties from GMPMs models where is not possible to consider all or most of the dynamic process produced during an earthquake, for example, the source rupture process (*e.g.* heterogeneous coseismic slip, rise time, rupture velocity), and reflects that the uncertainty in GMPMs is produced as a result of scarcity of observed intensities data for near-field subduction scenarios.

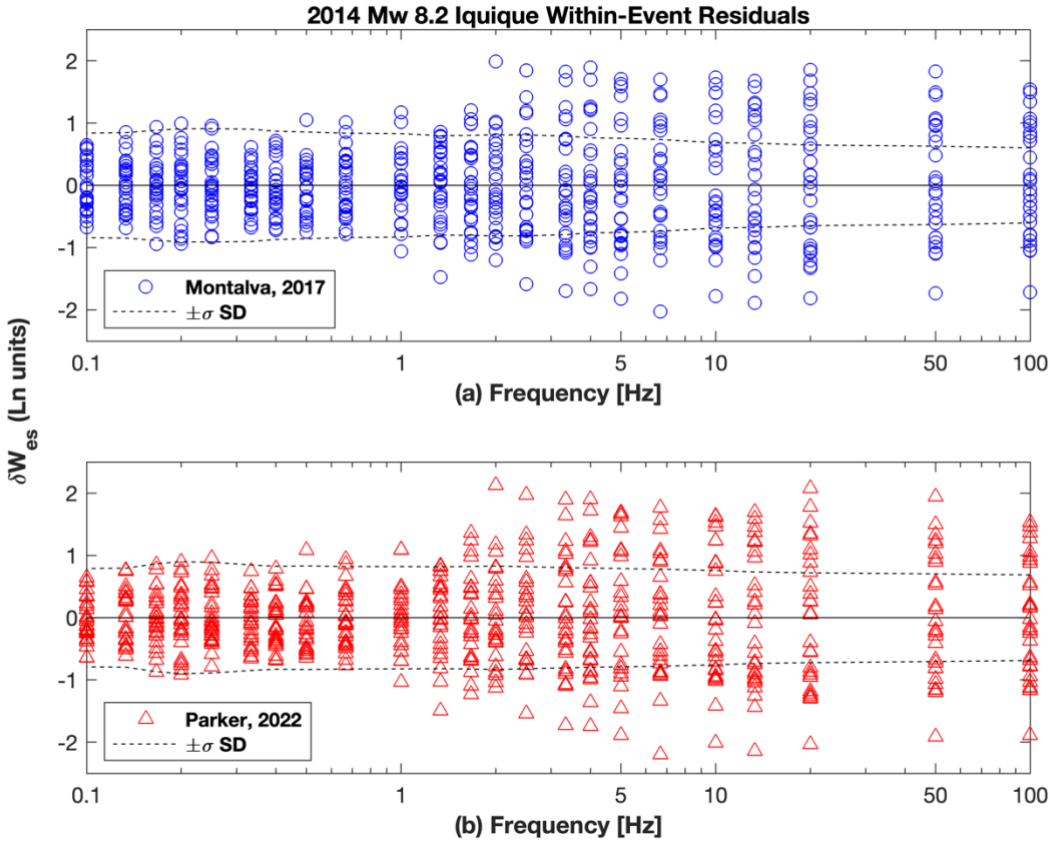

Figure 3.1. Within-event residuals (δW_{es}) against frequency: (a) Montalva *et al*. (2017); (b) Parker *et al*. (2022) GMPM models, for the 2014 Mw 8.2 Iquique Earthquake.

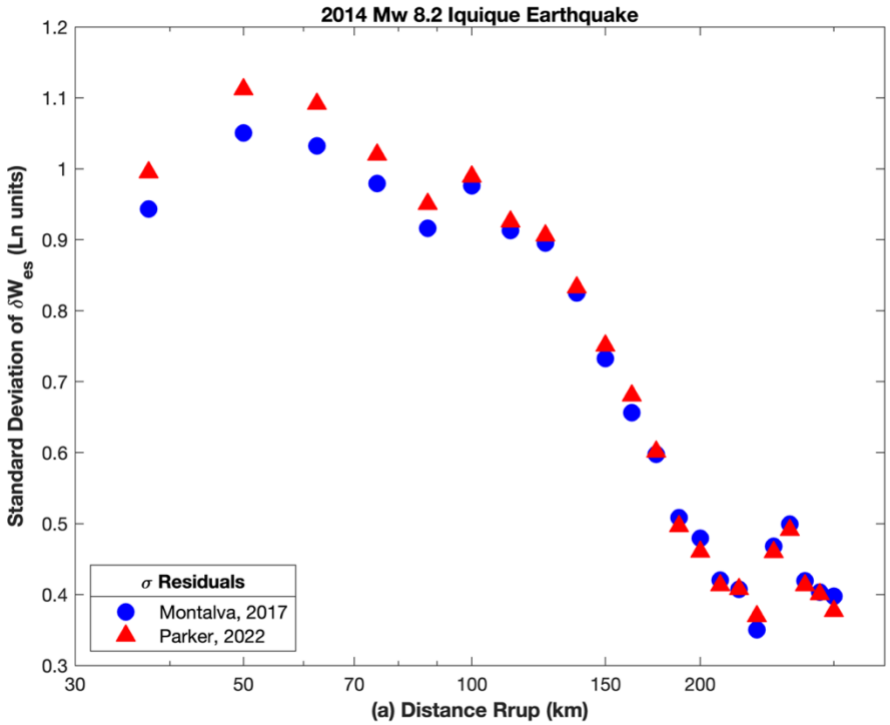

Figure 3.2. Within-event residuals (δW_{es}) standard deviation against the source-to-site distance from Montalva *et al.* (2017) and Parker *et al*. (2022) GMPMs models; 2014 Mw 8.2 Iquique Earthquake.

Utilizing GMPMs is well consolidated in the SHA, but the use of Physics-Based Numerical Simulations (PBSs) is gaining popularity thanks to the ongoing progress in recent years that allowed the validation of real earthquake case studies and compare the simulations results with records (Tsuda, 2021; McCallen *et al.,* 2021; Stupazzini *et al.*, 2021; Paolucci *et al*., 2015; 2018a; 2018b; Bradley *et al.*, 2017; Taborda and Bielak, 2013; 2014; Graves and Pitarka, 2015; 2010; 2004). Earthquake PBSs have become necessary for a better understanding of the seismic wave propagation mechanism, strong-motions characteristics, and as a complement to recorded data (Ojeda *et al.,* 2021; McCallen *et al.,* 2021; Stupazzini *et al.*, 2021; Taborda and Bielak, 2013). The increasing availability of high-performance computational capability has enabled PBSs to obtain representative synthetic strong-motions, helping to augment the limited number of observations in near-field regions for destructiveness earthquakes (McCallen *et al.,* 2021), yielding reliable results for large rupture areas (Stupazzini

et al., 2021; Paolucci *et al*., 2018a; 2018b; Taborda and Bielak, 2014). Ground-motion simulations through PBSs and verification are becoming necessary chores to determining its predictive capabilities in the SHA and in seismic engineering applications.

Earthquakes produce broadband strong-motions records, where both the low-frequency ($f < 1$ Hz) and high-frequency ($f \geq 1$ Hz) regions are included. Nevertheless, performing the three-component waveforms simulations, that is North-South (NS), East-West (EW), and Vertical (Z), are still defiant, especially at frequencies larger than 1 Hz (Ojeda *et al.*, 2021; Stupazzini *et al.*, 2021; Graves and Pitarka, 2010; 2004). A hybrid method which combines low-frequency strong-motions time histories and high-frequency ones has been proposed to simulate realistic strong-motions and is currently popular in recent studies (Ojeda *et al.*, 2021; Akinci *et al.*, 2017; Graves and Pitarka, 2015; 2010; 2004; Liu *et al.*, 2006).

Low-frequency strong-motions histories are calculated with a deterministic technique using 3D Finite Element Method (3D-FEM) wave propagation (Aagaard *et al.*, 2013). The three-component high-frequency strong-motions histories are obtained through a stochastic approach proposed by Otarola and Ruiz (2016) and Ruiz *et al*. (2018). Finally, merged the low and high-frequency strong-motions histories into a single broadband series (Ojeda *et al*., 2021; Graves and Pitarka, 2010; 2015; Mai and Beroza, 2003) using a match-filtering (Kamae *et al.*, 1998; R. Graves, personal communication).

The integration of PBSs focused on subduction megathrust earthquakes, and validated with a known event, *i.e.*, 2014 Mw 8.2 Iquique earthquake, will help to adjust the scattering between measured and observed intensities on the ground surface for the near-field region. Imposing physical thresholds to both source parameters (e.g. slip, rise time, rupture velocity) and geologic rheology for a subduction zone, the numerical simulations will be performed within a much more limited parametric space in the near-field region (i.e. 30 to 70 km), resulting in a restricted dispersion range for the IM_{pred} for future earthquakes.

3.2. Methodology

We focus on the 1 April 2014 Mw 8.2 Iquique Earthquake, this event ruptured a portion of the subduction zone in northern Chile offshore of the city of Iquique, a major port and hub for the country's copper mining industry (Hayes *et al.*, 2014; Ruiz et al., 2014; Schurr *et al.*, 2014). The rupture area broke a central fraction of the so-called northern Chile seismic gap, a zone where the last mega-earthquake occurred in 1877 (Ruiz and Madariaga, 2018). Iquique 2014 has a rupture with a maximum slip of 4.5 m obtained from continuous GPS stations data inversion (Schurr *et al.*, 2014). Peak shaking intensities reached MMI VIII on land, and a tsunami ~2 m high hit coastal towns in southern Peru and northern Chile (Cilia et al., 2017; Catalan et al., 2015). The ground-motions were recorded from strong-motion stations located on the continental surface near the hypocenter (Leyton et al., 2018b), the stations used here are listed in Table 3.1.

Table 3.1. Stations with peak ground accelerations (PGA) from processed recordings of the April 1, 2014 Iquique Earthquake, minimum distance rupture-to-station (R_{rup}) and local V_{S30} site conditions.

Station Code	Lat (°)	Lon (°)	R_{rup} (km)	PGA_N (cm/s)	PGA_E (cm/s)	PGA_Z (cm/s)	V_{S30} (m/s)
PB01	-21.04	-69.48	68.41	102.65	95.91	69.49	603
PB02	-21.32	-69.89	53.27	85.28	163.42	109.20	746
PB03	-22.05	-69.75	118.31	28.57	36.23	32.45	711
PB04	-22.33	-70.15	141.56	35.16	29.16	23.65	563
PB11	-19.76	-69.65	61.84	718.43	484.82	464.66	846
T03A	-20.23	-70.14	40.86	592.62	562.69	211.36	635
T05A	-20.21	-70.15	40.83	267.08	299.45	250.09	809
PB08	-20.14	-69.15	101.67	93.14	81.12	58.08	742
PB12	-18.61	-70.32	38.08	96.67	105.82	67.63	599
PB16	-18.33	-69.51	86.01	35.57	29.41	24.14	861

The synthetic broadband strong-motions time histories were performed in its three-components covering the entire frequency band of engineering interest (0.01 to 30 Hz), following a hybrid technique, where the low-frequencies (LF) and high-frequencies (HF) were computed separately and then merged into an entire broadband time history (Ojeda *et al.*, 2021; Graves and Pitarka, 2015; 2010; 2004).

3.2.1. Low-frequency ground-motions simulations (f < 1 Hz)

The low-frequency (LF) seismograms were simulated through the Finite Element (3D-FEM) package, PyLith© (Aagaard *et al.,* 2023a*;* 2013), using a kinematic source rupture process following the slip time function developed by Liu *et al.* (2006), who combined cosine-sine functions to create a slip time history with a finite duration of slip. The 3D-FEM mesh geometry is placed between 18.5°S and 22.5°S along the northern Chile subduction zone. The slab surface is constructed according to the Slab2 model (Hayes et al., 2018), combined with the trench and the moho discontinuity described in Tassara and Echaurren (2012). Additionally, the bathymetry and the topography were obtained from the General Bathymetric Chart of the Oceans (GEBCO). Cubit® software is employed to develop the mesh, where tetrahedral elements are used, and a simulation domain of 700 km x 500 km x 140 km was considered that covers the subducting slab, the hypocenter, the rupture area, and the projected affected surface zone.

The considered bodies in the 3D-FEM mesh correspond to: Continental Crust, Oceanic Crust (including slab), Continental Mantle, and Oceanic Mantle (see Figure 3.3). For the last three volumes the visco-elastic properties, that is, Young's modulus (E), Poisson's ratio (ν), and density (ρ) were derived from the works of Tassara and Echaurren (2012); Moreno *et al.,* (2012). The material properties within the Continental Crustal body, that is, the seismic velocities V_P and V_S, and the material density ρ, correspond to an interpolation of the velocity models data for northern Chile proposed in Comte *et al.* (2016), and Gao and Tilmann. (2021). The mesh elements size (e) was zoned, that is, in the resultant projection of the coseismic area on the ground surface the mesh elements were fitted to satisfy the maximum frequency of 1.5 Hz and the minimum Vs of 200 m/s, resulting in e between 200 and 300 m, and for the rest of mesh bodies, the e are increased to optimize the running time, Table 3.2 shows the mesh characteristics. Finally, to avoid wave refractions and the consequent disturbance within the domain of interest, we adopted the PyLith-implemented absorbing boundary conditions in each domain border.

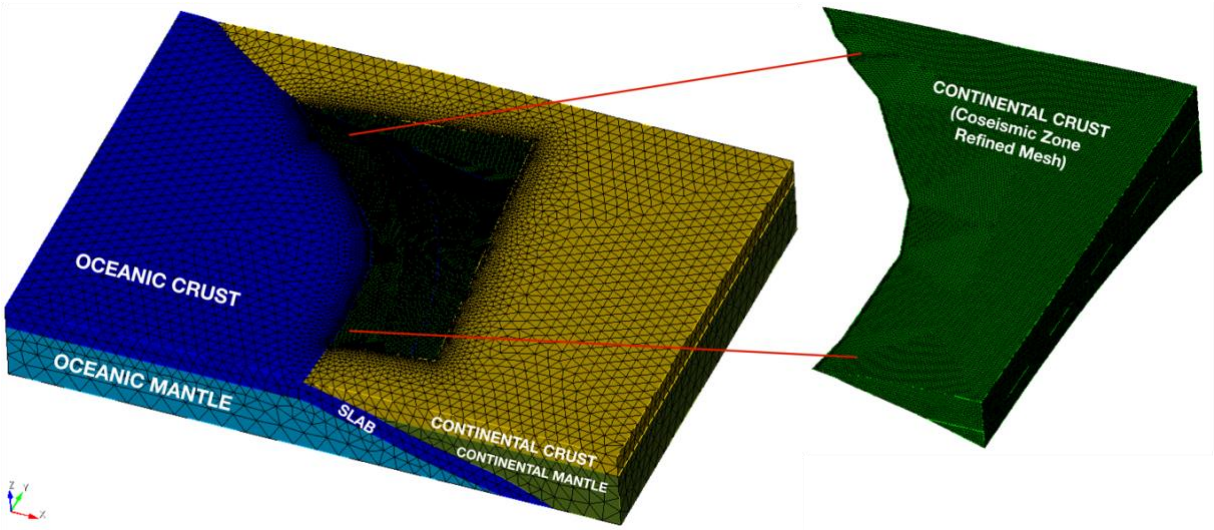

Figure 3.3. FEM-mesh over the subduction zone studied.

Table 3.2. Mesh characteristics and FEM-simulation parameters.

Domain	
Domain Size	700 km x 500 km x 140 km
Southwest corner	-22.2541°, -72.8595°
Northwest corner	-17.2148°, -73.1982°
Northeast corner	-16.9041°, -68.9850°
Southeast corner	-21.9449°, -68.5119°
Spatial Resolution	
Maximum frequency	1.5 Hz
Minimum V_S	200 m/s
Minimum *e*	300 m
Maximum *e*	35000 m
Number of elements	13,190,179
Number of nodes	2,268,623
Time Resolution	
Simulation Δt	0.001 s
Simulation Total Time	192 hours

The coseismic slip, rise time (T_r), and rupture velocity of each sub-fault, i, are three parameters that play critical roles in determining the evolution of slip at a point on the surface. Coseismic slip distribution over the rupture area is obtained from Schurr *et al.* (2014) who developed its model through joint inversion of the teleseismic waveforms and geodetic (GPS) data. T_r is calculated with the relationship proposed by Cárdenas *et al.* (2023) for large

subduction megathrust earthquakes, which involves the seismic moment (M_0) in its functional form, and corresponds to:

$$T_r = 6.31 \times 10^{-7} \times M_0^{1/3} \quad (3.2)$$

The rupture initiation time (T_i) parameter is determined using the following expression:

$$T_i = R/Vr \quad (3.3)$$

where R is the distance between the earthquake hypocenter to a given slip point on the rupture area, V_r is the rupture velocity and corresponds to 80% of the shear wave velocity, V_S, at the source, which was validated after several iterations and resembles that proposed by Liu *et al.* (2006); Graves and Pitarka. (2010; 2004); and Skarlatoudis *et al.* (2015). The 3D-FEM compilations were run using the CEDIA-HPC supercomputer with 28 CPU cores and 256 GB RAM.

3.2.2. High-frequency ground-motions simulations (f > 1 Hz)

The high-frequency (HF) time series were obtained through a stochastic method to simulate P, SV, and SH waves that allow to obtain horizontal and vertical strong-motion accelerograms, following the methodology proposed by Otarola and Ruiz (2016), Ruiz *et al.* (2018) and (Ojeda *et al.*, 2021), wherein, starting from the method proposed by Boore (2003) which is stochastically modeled only one horizontal seismic wave component (SH), they extended the method to obtain the three-component acceleration time series (see details and references therein). The authors modeled the Fourier Spectrum of synthetic acceleration (A_{ijm}^{X}) according to equation (3.4),

$$A_{ijm}^{X} = \frac{\mathcal{R}_{ijm}^{X} FS_{ijm}^{X} EP_{ijm}^{X} M_{0ij}}{4\pi\rho V^{3}} \frac{1}{1+\left(\frac{f}{f_{cij}^{X}}\right)^{\gamma}} G(R_{ijm})$$

$$\exp\left(-\frac{\pi f R_{ijm}}{Q_X(f)V}\right) Amp(f) \exp(-\pi\kappa_{0m} f) (2\pi f)^{2} \quad (3.4)$$

where X corresponds to P, SV or SH waves, V velocity (P or S waves). The subscripts *i, j* specify sub-faults positions and the rupture time in which this sub-fault is activated, the subscript m indicates the station simulated, as is described in Ruiz *et al.* (2018). The source parameters consider the amplification factor due to the free surface (FS), the factor which models the energy partition obtained by incident and azimuthal angles of direct seismic rays from source to the station (EP), the radiation patterns ($\mathcal{R}$), for P, SV and SH waves are calculated for each sub-fault following the descriptions in Ojeda *et al.* (2021), that is, $\mathcal{R}$ coefficients are calculated according to the formulation proposed by Aki and Richards (Aki and Richards, 2002); furthermore, the seismic moment of each sub-fault (M_{0ij}), and the density in the source vicinity are considered. A $\omega^{-\gamma}$ model (γ = 1.75), and dynamic corner frequency, f_{cij}, for P or S waves were included (Otarola and Ruiz, 2016). The path parameters involve geometrical spreading G(R) and anelastic attenuation by employing quality factors Q(f). Finally, the site factors include both high-frequency attenuation through the kappa parameter (κ_0), and an amplification function ($Amp(f)$) for soil or rock. The κ_0-parameter represents the surface attenuation (in the uppermost kilometers of the crust) of seismic waves and is noted that κ_0-parameter values decrease as V_{S30} increases (Pozo *et al.*, 2022). Seismic station used in the simulations are located over different rock materials, the stations' shallow subsurface V_{S30} data are scarce in the northern Chile area, however, we use the horizontal-to-vertical spectral ratio (HVSR) to make up for the lack of better site characterization (Leyton *et al.*, 2018a; 2018b).

3.2.3. Input parameters for the broadband physics-based numerical simulations (PBSs) strong-motions: Finite Fault Source Rupture Model

For the 2014 Iquique earthquake finite fault source rupture model, the strike, dip and rake angles over the megathrust faulting area, and the dimension of each sub-fault were derived by combining the hypocenter location with the slab model, considering the rupture area described in the co-seismic slip by Schurr *et al.* (2014) which contains the entire asperities area investigated. The total earthquake finite fault rupture area over the megathrust is 66.960 km2, 558 km long (along trench strike) and 120 km wide (slab-dip direction). We adopted a value of 43.6 bars for stress drop ($\Delta\sigma$) in the HF spectral amplitudes simulations following Folesky et al. (2021).

Table 3.3. Source, Path, and Site parameters used as input for the high-frequency stochastic simulation.

Parameter	Value or Function	References
Source		
Finite Fault Rupture Model	558 (km) x 120 (km) strike, dip, rake, sub-faults number 347.00°, 13.50°, 90.00°, 372	Schurr *et al.* (2014) Hayes *et al.* (2014)
Hypocenter	lat, lon, depth -19.57°, -70.91°, 21.60 km	Bastías and Montalva (2016) and, Ruiz *et al.* (2014)
Rupture Time	According to Rupture Model	This study.
Velocity S waves	3.7 km/s	Comte *et al.* (2016) Gao and Tilmann. (2021)
Velocity P waves	6.2 km/s	
Density	3.3 g/cm^3	
Stress Drop	43.6 bar	Folesky *et al.* (2021)
Path		
Quality factor	$Q_S(f) = 600f^{0.4};\ Q_P(f) = 1350f^{0.4}$	
Geometrical spreading	$G = \begin{cases} \frac{1}{R} & if\ R \leq 50\ km \\ \left(\frac{1}{50}\right)\left(\frac{50}{R}\right)^{-0.1} & if\ 50 < R \leq 100\ km \\ \left(\frac{1}{50}\right)\left(\frac{50}{100}\right)^{-0.1}\left(\frac{100}{R}\right)^{1.4} & 100 < R \end{cases}$	Otarola and Ruiz (2016)
Site		
Kappa	Station dependent: $0.026 \leq \kappa_0 \leq 0.040$	Pozo *et al.* (2022)
Amplification	Amp(f) ~ HVSR-ratio (each station)	This study.

3.2.4. Input parameters for the broadband physics-based numerical simulations (PBSs) strong-motions: Seismic Wave Attenuation

In the stochastic simulation, seismic attenuation is an important physical parameter that influences fundamentally the shape and the spectra' amplitude. The quality factors correspond to $Q_S(f) = 600f^{0.4}$ *and* $Q_P(f) = 1350f^{0.4}$.

3.2.5. Input parameters for the broadband physics-based numerical simulations (PBSs) strong-motions: Site Amplifications

Site amplification is one of the crucial parameters that define the strong-motions records during the shaking of large events, these are controlled by the local site conditions causing amplifications in different period ranges of the response spectrum during an event, and damage in urban areas (Ojeda *et al.,* 2021; Leyton *et al.,* 2018a; 2018b). The stochastic methodology followed here encompasses the site amplification, where it follows both a subsoil shear wave velocity V_{S30} configuration or a Transfer Function in a frequency array. Nevertheless, owing to a scarcity of V_{S30} data for the seismological stations emplaced in northern Chile which recorded the Iquique earthquake, and lack of defined Transfer Functions, we employed the HVSR-ratios geophysical characterization to characterize the site amplification. It has been established that there is no direct correlation between peak amplitude and predominant period of the horizontal-to-vertical spectral ratio curves for the different strong-motions stations (Leyton *et al.,* 2018a; 2018b), therefore the HVSR-ratios were obtained for each station analyzed. The HVSR amplitudes vs. frequency (period) curves work as a transfer function (Ghofrani *et al.,* 2013) for the three-components defined in a frequency range of 0.01 to 10 Hz, Figure 3.4 shows an example of an HVSR-ratio curve as a soil amplification factor (transfer function) applied in the T05A station.

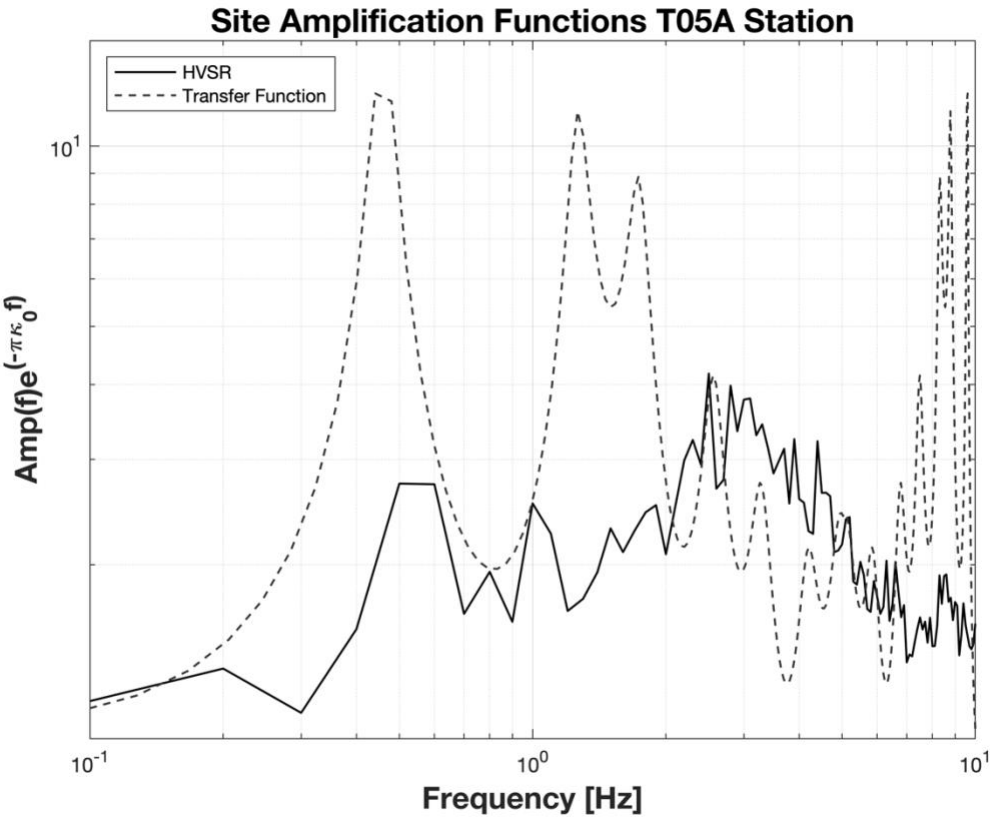

Figure 3.4. Comparison between HVSR-ratio curve and transfer function for the T05A station.

Once the amplification factors have been applied, in the broadband strong-motions time series merging, a match-filtering criterion requires that either the amplitude or the power spectra of the low- and high-pass filters sum the unity across all frequencies. However, it is not always possible in a hybrid approach, due to the influence of various factors including multi-pathing, travel time, and site response, therefore, the match-filtering is used by first applying low-pass and high-pass N^{th}-order, zero-phase Butterworth filters to the low- and high-frequency series, respectively, and then summing these filtered histories with a cross-over frequency range of around 0.75 to 1.1 Hz (Graves and Pitarka, 2010; Kamae *et al.*, 1998, R. Graves, 2023 personal communication).

3.3. Results and Discussion

The Schurr *et al*. (2014) slip model for the 2014 Mw 8.2 Iquique megathrust earthquake shows a single concentric asperities zone, however, the frequency content irradiated during the earthquake is more complex. Here was not possible to characterize the areas that contain large slip velocity or high-stress drop, over the seismic source rupture area known as High-Frequency Strong-Motions-Generation-Areas (Kurahashi and Irikura, 2011), that is, the zones which radiate more high frequencies, despite these zones could show low slip values. The slip distribution obtained through 3D-FEM technique shows a single asperity zone (concentric patch), where the maximum megathrust slip is 4.50 m (see Figure 3.5). Figure 3.6 shows the evolution of displacement magnitude distribution with final maximum values up to 200 cm. In the following sections, we describe the result analyses for the four closest stations to the source (PB01, PB08, PB12, T05A). The recorded acceleration time series were obtained from Bastías and Montalva (2016) database. Slip and displacement distribution animations are included in @S2 (supplementary).

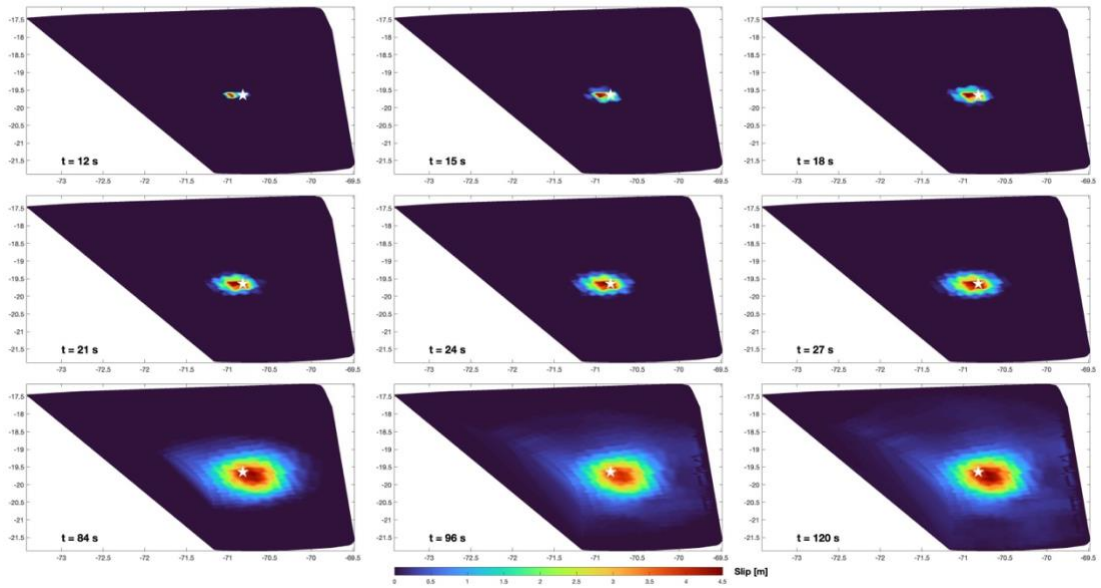

Figure 3.5. Snapshots of the simulation's slab (source) rupture. Corresponding instantaneous times are shown at the bottom-left corner of each frame. The epicenter of the event is indicated by a white star. White diamonds correspond to the consider stations.

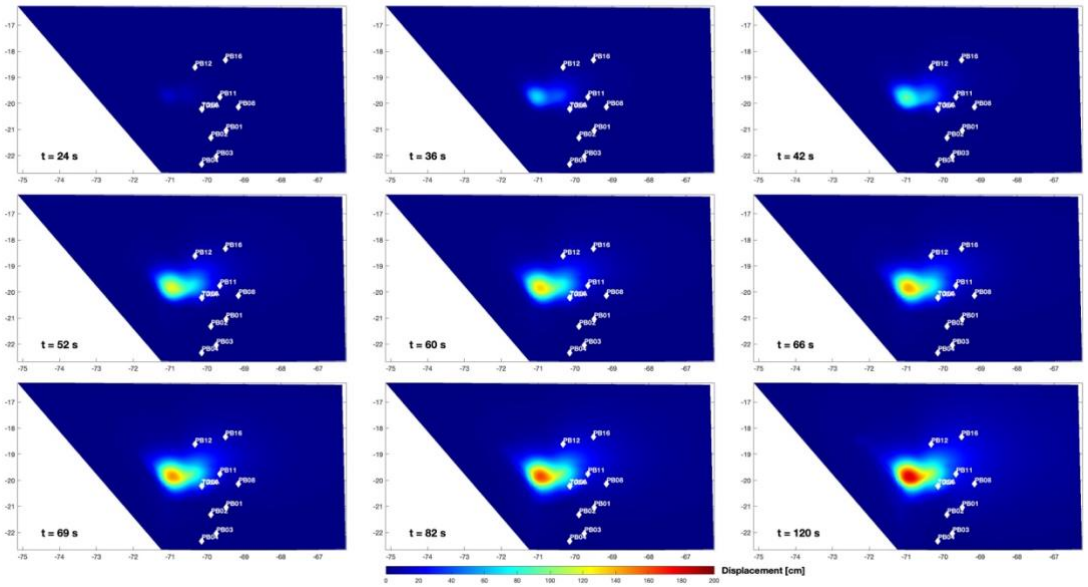

Figure 3.6. Snapshots of the simulation's surface horizontal magnitude displacement. Corresponding instantaneous times are shown at the bottom-left corner of each frame. White diamonds correspond to the consider stations.

3.3.1. Low-Frequencies (LF)

Through the 3D-FEM method was possible to obtain the strong-motions acceleration time series up to 1 Hz, high simulations computation time was demanded (192 hours) due to the large megathrust source rupture, and the great mesh domain to include all the principal subduction bodies involved during the earthquake initiation. The Fourier amplitude spectra (FAS) for the analyzed stations in the low frequencies range denote a good agreement between the simulated and the recorded data, see Figure 3.7. However, the PB01 station shows a slight major misfit in relation to the other stations, especially on the EW and Z components.

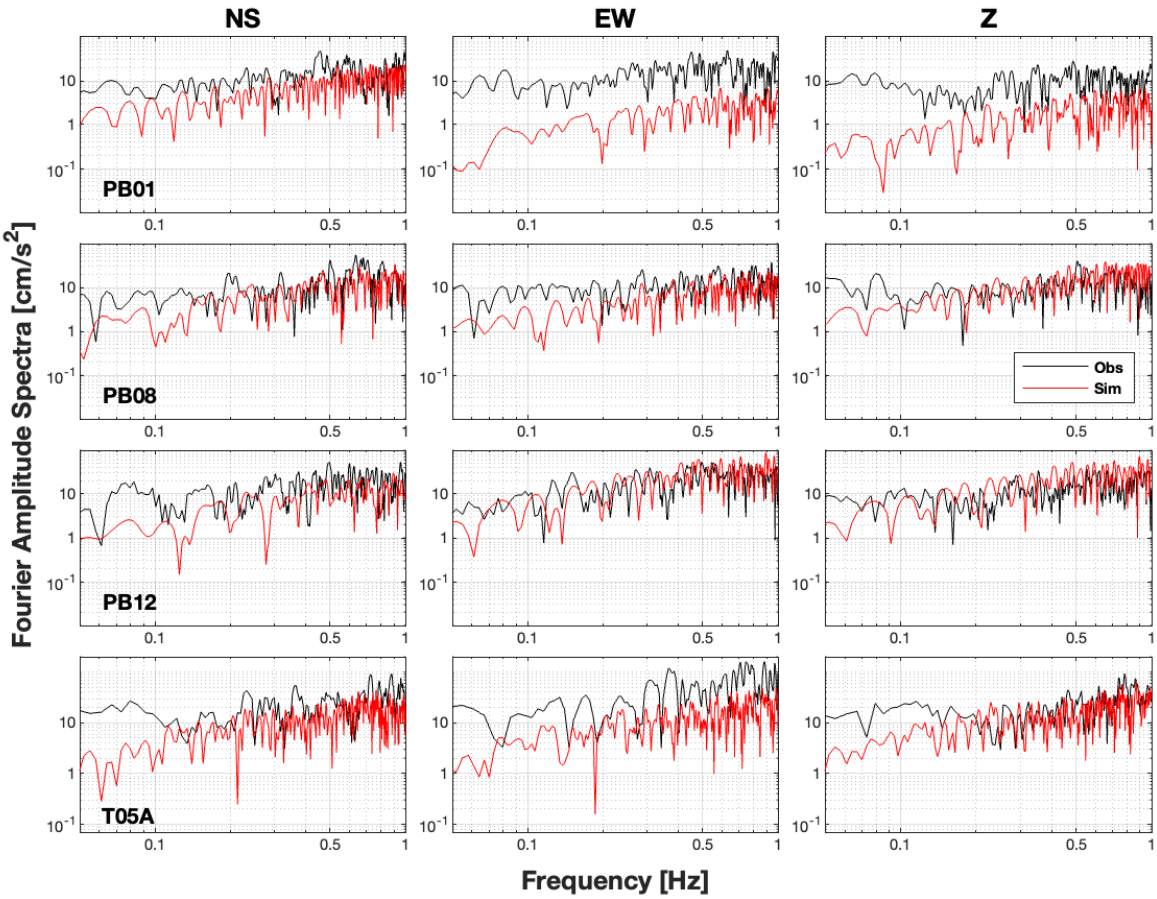

Figure 3.7. Example of Low-Frequency three-components acceleration synthetic's FAS at PB01, PB08, PB16 and T05A stations. Both spectra are combined using a complementary filter around 0.01-1.1 Hz after a time synchronization.

3.3.2. High-Frequencies (HF)

The high-frequency arranges were estimated with the stochastic approach up to 30 Hz, where the site effect was evaluated using the HVSR-ratios instead of a defined transfer function for each station (see Figure 3.6). The FAS in each station shows a good fit between simulations and recordings (Figure 3.8) demonstrating that HVSR-ratios used as site amplification functions work properly.

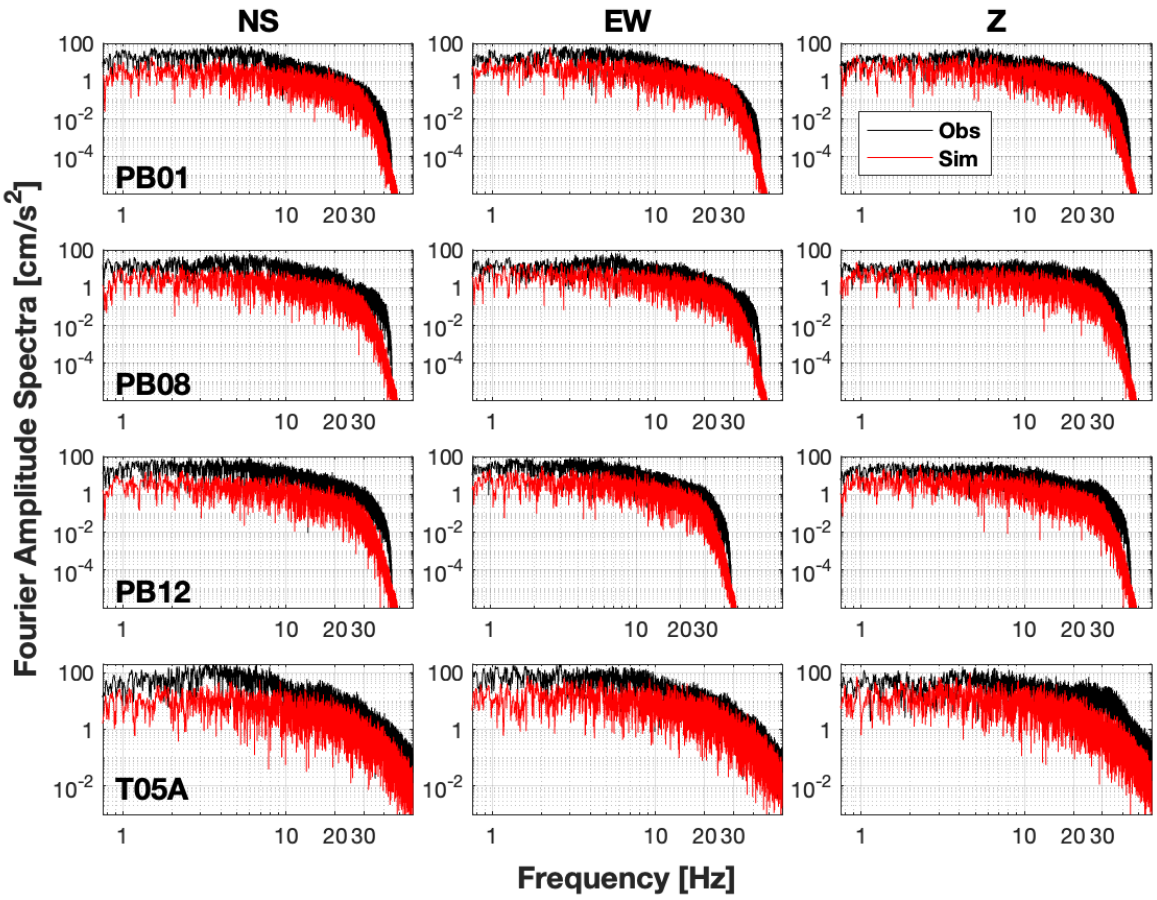

Figure 3.8. Example of High-Frequency three-components acceleration synthetic's FAS at PB01, PB08, PB16 and T05A stations. Both spectra are combined using a complementary filter around 0.75-30.0 Hz after a time synchronization.

3.3.3. Broadband Time Series

The broadband acceleration time series were paired following the match-filtering procedure described above using a Butterworth second-order filter (see Figure 3.9), the peak acceleration values from the simulated series show a slight misfit compared with the recorded values. The earthquake duration trace in each component does not show major differences between recorded and simulated data for the four stations.

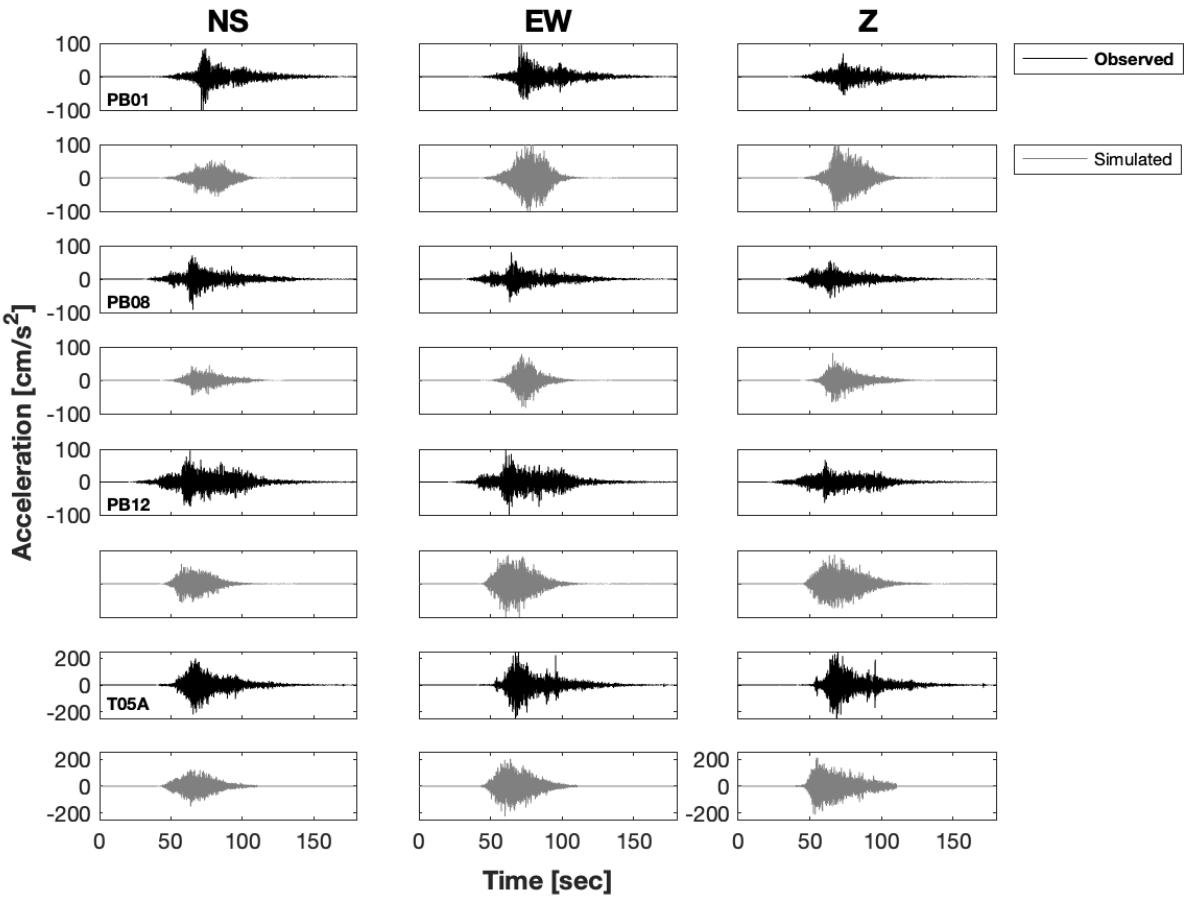

Figure 3.9. Simulated and observed accelerograms for PB01, PB08, PB16 and T05A stations for the 2014 Iquique earthquake, in the three-components.

For spectral accelerations, in general, the simulated spectra have similar values to recordings (Figure 3.10), suggesting that the use of the HVSR-ratios as site amplification functions work properly. Nevertheless, in some cases, clear spectral peaks in the observed records were not reproduced by simulations. For example, the peak amplitude of the NS component of the PB08, PB12, and T05A and the EW component of the T05A stations are underestimated, while in other stations the spectral accelerations are overestimated as is the case of the EW component of PB01 and the Z component of T05A. A possible explanation for this discrepancy is that most stations do not have a detailed velocity model (e.g. V_{S30}, V_P/V_S) in the shallow zone up to the subsurface.

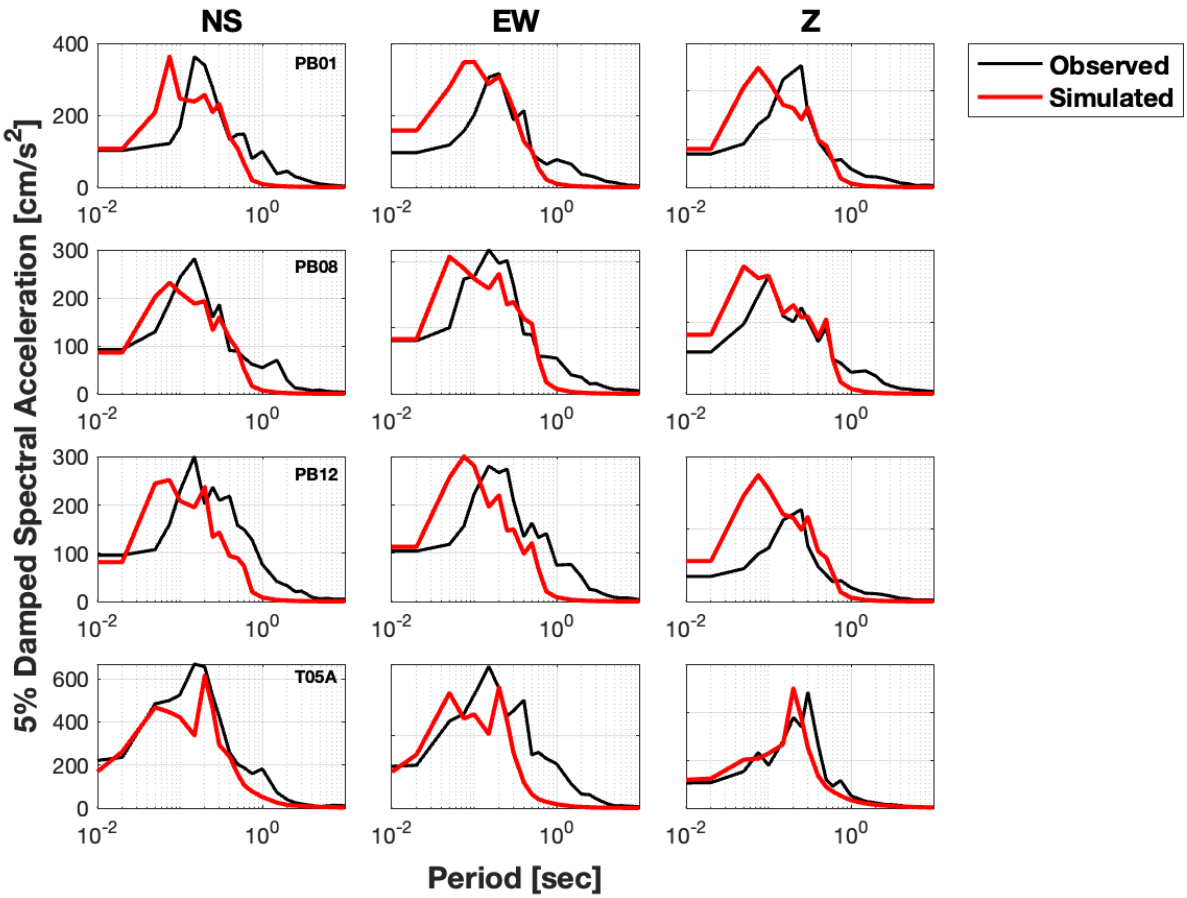

Figure 3.10. 5% - Damped Sa-s for PB01, PB08, PB16 and T05A stations in their three-components.

To evaluate the goodness of fit, we compare the observed and simulated records using the model bias B(T_i) and standard error for the 5% damped spectral acceleration following Graves and Pitarka (2010):

$$B(T_i) = \frac{1}{N}\sum_{j=1}^{N}\left\{r_i(T_i) = ln\left[\frac{O_j(T_i)}{S_j(T_i)}\right]\right\} \quad (3.5)$$

where $r_i(T_i)$ is the residual between the observed and simulated spectral acceleration at period T_i for the jth station, $O_j(T_i)$ and $S_j(T_i)$ are the observed and simulated records respectively, and N is the number of stations. The standard error is given by:

$$\sigma(T_i) = \left(\frac{1}{N}\sum_{j=1}^{N}\left[r_j(T_i) - B(T_i)\right]^2\right)^{\frac{1}{2}} \quad (3.6)$$

The goodness of fit is summarized in Figure 3.11, in general values of B(T_i) included between -1.5 and 1.5 are considered successful modeling, and as well as low standard deviation values, we observe a good fitting for the periods between 0.01 and 1 s in the three components. On the other hand, for periods > 1s, especially in the Z component, the values of B(T_i) are around 2 with high standard error values which indicates that the simulation is underestimating the ground motion.

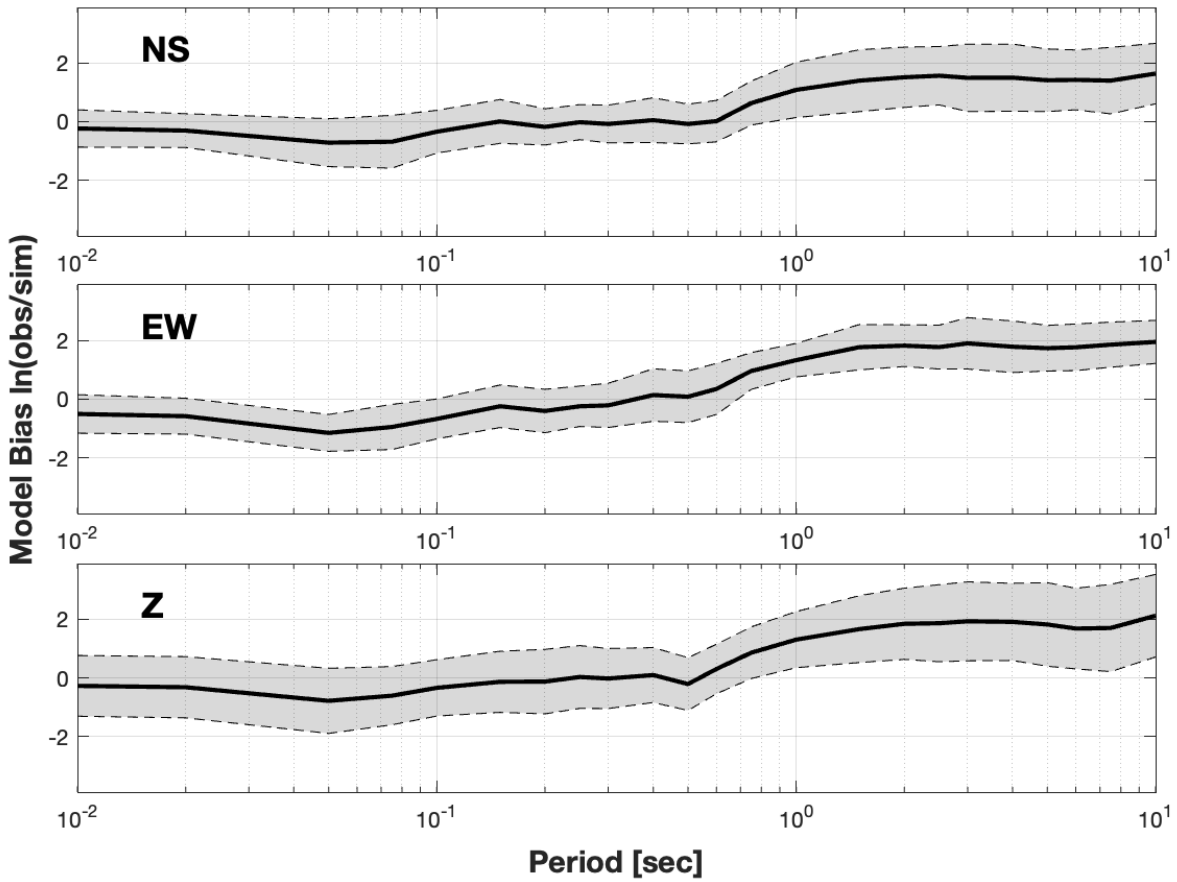

Figure 3.11. Model Bias (heavy line) and standard error (shaded region) between observed and simulated acceleration response spectra of 5% damping, using 10 stations.

Here, unfortunately, was not possible to obtain the entire broadband time series only through the 3D-FEM approach, this is a consequence of the fact that for large magnitude subduction earthquakes the resulting 3D-FEM-mesh volume domain is very large (*i.e.* there is a high number of elements and nodes) due to we had to include at least the four principal subduction zone bodies ensuring the computational time cost also very high, in contrast with earthquakes triggered in crustal faults, where the 3D-FEM-mesh volume domain and running time are less expensive (Taborda and Bielak, 2013; 2014). To keep the running time on the supercomputer around 192 hours, here the element size of the 3D-FEM-mesh for the coseismic zone was not reduced to the most optimal size ~200 to 100 m per element, seems this can contribute to the underestimation observed in the model Bias.

The hybrid broadband series were constructed using a match band to link the LF and HF spectra, the band match is ranged between 0.75 and 1.1 Hz, unlike what has been proposed in previous works for crustal earthquake simulations (Lee *et al.,* 2020; Akinci *et al.*, 2017; Graves and Pitarka, 2015; 2010; 2004; Mai and Beroza, 2003) where only a single frequency value of 1 Hz is used to match HF and LF spectra. The final form of the synthetic Iquique earthquake accelerograms do not reproduce, as well as slightly lower peak accelerations in some stations, this could be as consequence of the fact that the position of the slip distribution of the 2014 Iquique earthquake located near the trench favor the presence of reflected and refracted waves, affecting specially the HF range (stochastic method), also described by Otarola and Ruiz (2016).

Finally, Figure 3.12, shows the behaviors of the IM_{obs} and PBSs intensities values for the 8.2 M_w Iquique Earthquake and are compared with the empirical GMPMs proposed by Montalva *et al*. (2017) and Parker *et al.* (2022). Where it is observed that the PBSs intensities show a good fit with the IM_{obs}, in addition, the PBS intensities fall in a more constrained range below the GMPM ±1 standard deviation (σ), especially in the closets station-to-site distances (R_{rup} < 70 km). Furthermore, the total residual values (Figure 3.13) obtained from the PBS and each GMPM, respectively, the PBS residuals are slightly lower than the GMPMs ones, in the near-field distances, which indicates that an improvement in the prediction of seismic intensities

has been achieved, validating the near-field simulations based on earthquake physics (PBSs) for the Iquique event. While, in the $R_{rup} > 70$ km range, the residual values of both PBS and GMPMs show no major differences.

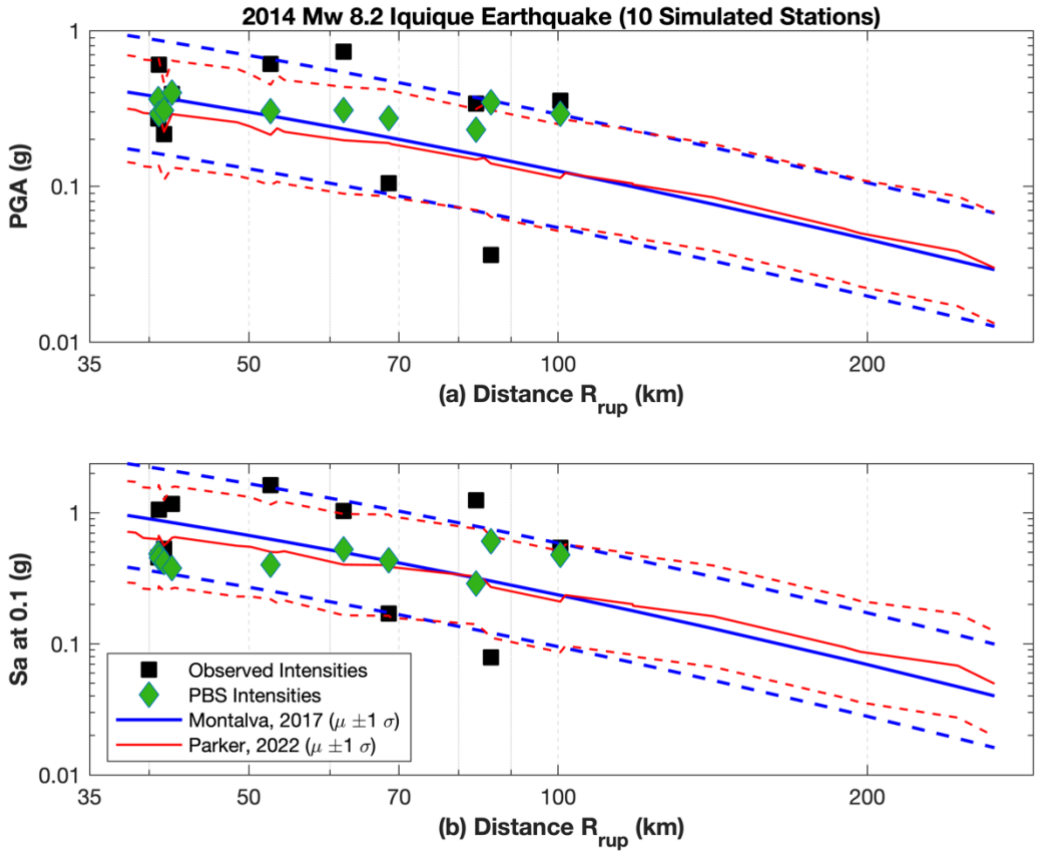

Figure 3.12. Comparison of Observed and Physics-Based Simulations, PBS. (a) peak ground acceleration (g), (b) Sa at 0.1 (g) values of the M_W 8.2 Iquique Earthquake against the simulated Montalva *et al.* (2017) and Parker *et al.* (2022) GMPMs parameters calculated at the 10 corresponding stations.

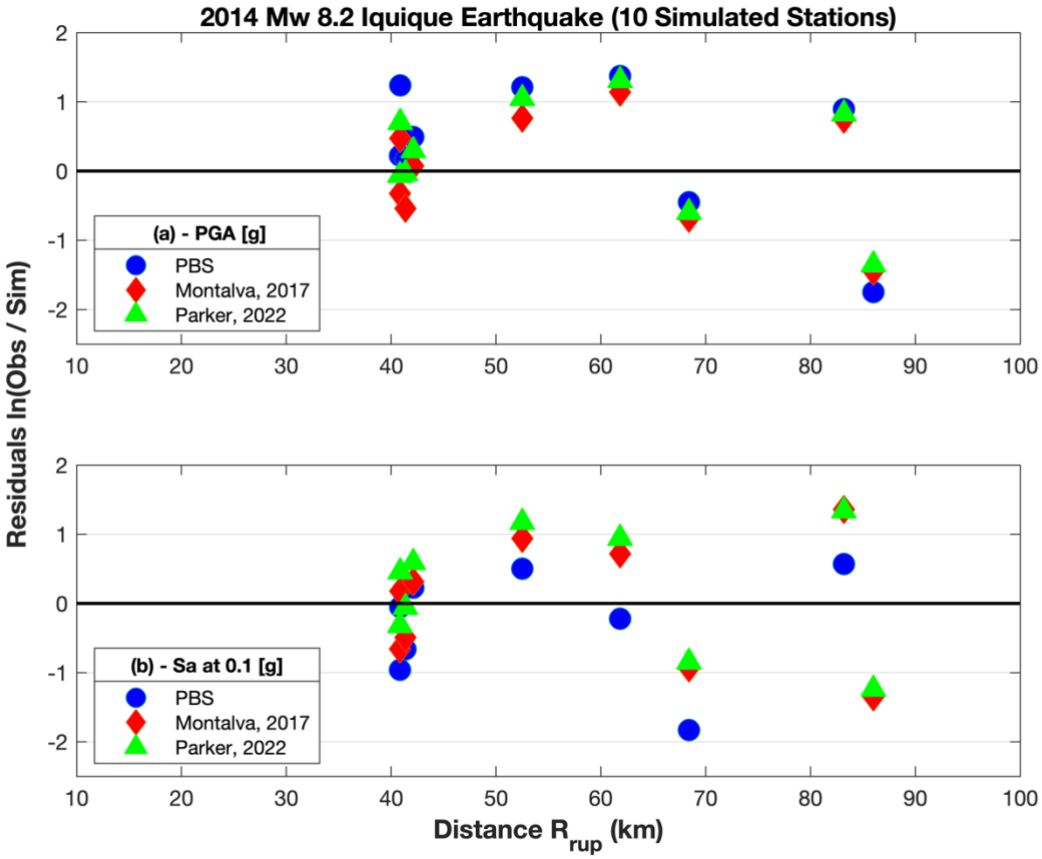

Figure 3.13. Residuals calculated for the Physics-Based Simulations and the two GMPMs from Montalva et al. (2017) and Parker et al. (2022), (a) peak ground acceleration (g), (b) Sa at 0.1 (g) values of the MW 8.2 Iquique Earthquake plotted as functions of station-to-rupture distance (R_{rup}) at the 10 corresponding stations.

3.4. Conclusions

We simulated Broadband synthetic strong-motions for Mw 8.2 Iquique earthquake triggered in the Chilean subduction zone. Simulated accelerograms were reproduced for 10 stations that recorded the event located up to 142 km of station-to-rupture distance (R_{rup}). The geological complexity of a megathrust somehow limited us to reach the high frequency (f >1 Hz) strong-motion content using only the FEM simulation methodology, therefore, the hybrid approach was developed, i.e., using both the stochastic and the FEM methods to complete the

entire broadband acceleration time series for the three-components (NS, EW, Z), merging the LF and HF ranges for each orthogonal component.

For the LF range we developed a large FEM-mesh domain which contains a great number of tetrahedron elements (13,190,179) and nodes (2,268,623), where e = 200 m to 300 m was chosen for the coseismic interest zone, allowing frequencies of up to 1.5 Hz to pass through, employing the PyLith code (Aagaard *et al.*, 2023a; 2013). For the HF a stochastic technique was employed through the PWSIM (Ojeda *et al.,* 2021; Ruiz *et al*., 2018; Otarola and Ruiz, 2016) as described.

The hybrid technique allowed us to obtain simulated broadband time series ranged between 0.01 to 30 Hz. Unfortunately, so far, the High-Frequency Strong-Motion-Generation-Areas have not been characterized for the Iquique 2014 event then these results could be improved in the future. Our work has some limitations, the model Bias evaluation showed an underestimation for periods > 1 s (*i.e.,* f < 1 Hz) this is a consequence of the large FEM-mesh domain and its element size around ~ 200 m to keep not too great running times. Furthermore, we employed a regional velocity model derived from Gao and Tilmann (2021) and Comte *et al.* (2016), consequently for the uppermost subsurface zone (~ 0 to 5 km depth) there is no detailed velocity model.

To improve the site amplification evaluation the HVSR-ratios were introduced in this work, the HVSR-ratios were obtained following the recommendations stated in Leyton *et al.*, (2018a; 2018b), using HVSR amplitudes vs. frequency (period) curves, and the results are in good agreement.

Simulated strong-motions at the selected stations are compared against the observed records showing low misfits. The close match between the simulated peak values and the corresponding values obtained from spectral accelerations curves indicates a good

parametrization of the source, propagation, and site despite the existing uncertainties in the megathrust.

For future analyses of large megathrust earthquakes through PBSs, we recommend trying to use slip deficit models, source scaling relationships, and more detailed velocity models that allow to determine and evaluate strong motions for non-occurring events, and that their physical credibility presents little uncertainty.

CAPÍTULO IV. Síntesis y discusión

La presente tesis doctoral abordó la evaluación de la amenaza sísmica (*Seismic Hazard Analysis, SHA*) mediante Simulaciones Numéricas Basadas en la Física (Physics-Based Simulations - PBSs) de grandes terremotos de megathrust, donde a través de validar un evento ocurrido y registrado como el Terremoto de Iquique 2014 ($8.2M_w$), sirva de herramienta para obtener la distribución de los movimientos fuertes del terreno (*strong-motions*) en un determinado emplazamiento (sitio o localización de la estación sismológica) ubicado en la región del campo cercano (*near-field*) para futuros terremotos que se desencadenen en el megathrust de una zona de subducción. Los acelerogramas sintéticos (*strong-motions*) de banda ancha, que incluyen y combinan las técnicas cinemática y estocástica, obtenidos dentro de este trabajo son denominados como PBSs.

Se seleccionaron 10 estaciones acelerográficas ubicadas sobre roca (ver Tabla 3.1), que registraron las aceleraciones de los *strong-motions* durante el Terremoto de Iquique, disponibles en la base de datos de Bastías y Montalva (2016). Las modelaciones de las series de tiempo para los *strong-motions* en el rango de frecuencias de 0.01 Hz a 30 Hz, utilizando PBSs, se obtuvieron mediante una metodología híbrida, que comprende:

- Técnica determinística, implementada a través del método de elemento finitos (3D-FEM) para la estimación del movimiento fuerte en bajas frecuencias ($0.1 \text{ Hz} < f < 1 \text{ Hz}$).
- Método estocástico, donde se modelaron las altas frecuencias ($1 \text{ Hz} < f < 30 \text{ Hz}$), con la utilización de la técnica estocástica, descrita previamente.

Esto permitió incluir los parámetros fundamentales involucrados en la ruptura de la fuente sismogénica (i.e., Tr, *velocity rupture*, *co-seismic slip*), el patrón de radiación de ondas sísmicas y el comportamiento espacial de los movimientos fuertes del terreno (*strong-motions*), producto de la generación de grandes terremotos en el megathrust de zonas de subducción.

4.1. Diseño del mallado de elementos finitos (3D-FEM)

Se desarrolló un mallado de elementos finitos a través del software Cubit®, en donde se incorpora: la geometría (volúmenes), las reologías elásticas (*i.e.* corteza oceánica, corteza continental), las reologías viscoelásticas (*i.e.* manto oceánico, manto continental), típicos del megathrust del norte chileno entre los 18.5°S y 22.5°S de latitud. El cuerpo del slab de subducción se construyó a partir del modelo Slab2 (Hayes *et al*., 2018) combinado con la fosa y profundidad del Moho descritos en Tassara and Echaurren (2012). La batimetría y topografía fue diseñada con datos de General Bathymetric Chart of the Oceans (GEBCO).

Las características de la malla se describen en la Tabla 3.2, donde se obtuvo un dominio de 700 km x 500 km x 140 km, conformada por elementos tetrahedrales con un tamaño mínimo de 200 m (zona co-sísmica) y máximo de 35000 m (manto continental y manto oceánico) dando un total de 13,190,179 elementos con 2,268,623 nodos.

4.2. Metodología Determinística

La simulación de la ruptura de la fuente sismogénica inicia con la obtención de datos de slip cosísmicos heterogéneos a partir de los modelos de Schurr *et al.,* (2014) y Hayes *et al.*, (2014), para el terremoto de Iquique 2014 (8.2 M_W). Con el código FEM PyLith© (Aagaard *et al., 2023a;* 2013), que utiliza un proceso de ruptura cinemática siguiendo la función de slip, desarrollada por Liu *et al.*, (2006); en donde, además se identificó los parámetros que describen la física que se produce durante un gran terremoto de megathrust. Estos parámetros incluyen principalmente el slip cosísmico, velocidad de ruptura (*rupture* velocity) , tiempo de iniciación de la ruptura (*slip initiation time*), tiempo de duración del slip o rotura (*rise time* - Tr).

El Tr resultó ser un parámetro crítico y determinante dentro de la simulación cinemática para obtener las series de tiempo de los movimientos fuertes del terreno en bajas frecuencias

(LF), razón por la cual, se desarrolló una correlación a partir de datos de Modelos de Ruptura de Falla Finita (*Finite Fault Rupture Model*), FFRM, de grandes terremotos de megathrust estudiados alrededor del mundo, cuya regresión permite obtener valores escalados de Tr en función del M_0.

El rango LF se desarrolló con un dominio de malla 3D-FEM que contiene un gran número de elementos tetraédricos (13.190.179) y nodos (2.268.623), donde el tamaño del elemento; e = 300 m para la zona de interés co-sísmico, permitiendo el paso de frecuencias de hasta 1,5 Hz, empleando el código PyLith©, con un tiempo de ejecución de la simulación en un supercomputador de 192 horas.

En la Figura 4.1, se aprecian los Espectros de Amplitud de Fourier resultantes de las simulaciones para el Terremoto de Iquique 2014 en 3 estaciones (PB01,PB08, T05A), obtenidas mediante 3D-FEM para frecuencias < 2 Hz, considerando un mallado con tamaños de elemento (*e*) comprendidos entre 500 a 900 m para la zona co-sísmica, dónde se utilizaron dos modelos de configuración de slips co-sísmicos de Schurr *et al.* (2014) y Hayes *et al.* (2014), con valores máximos de slip de 4.5 m y 8.0 m, respectivamente. De la figura se puede inferir que la diferencia de valores entre espectros es mínima en la región de frecuencias mayores a 0.2 Hz, mientras que, para las frecuencias menores a los 0.2 Hz esta diferencia se observa más amplia. Con base en lo descrito, la distribución espacial de valores de slip considerados dentro de la ruptura de la fuente sismogénica, llega a marcar sus mayores diferencias dentro de un intervalo acotado a muy bajas frecuencias, y para los rangos de frecuencias más altas la distribución del slip no genera mayores cambios para los espectros. El slip co-sísmico junto con el Tr son parámetros críticos y se correlacionan entre sí (Cárdenas *et al.*, 2023; Cárdenas *et al.*, 2024 en revisión) dentro de las modelaciones numéricas 3D-FEM, además de que, distintas configuraciones de estos parámetros van a definir los niveles de variación entre datos de simulaciones y registrados, pero como se ha mencionado, estas variaciones no serán demasiado grandes, logrando que modelos de distribución de slip/slip-déficit racionales para rupturas de

grandes terremotos sean plausibles dentro de las simulaciones basadas en la física de terremotos (PBSs).

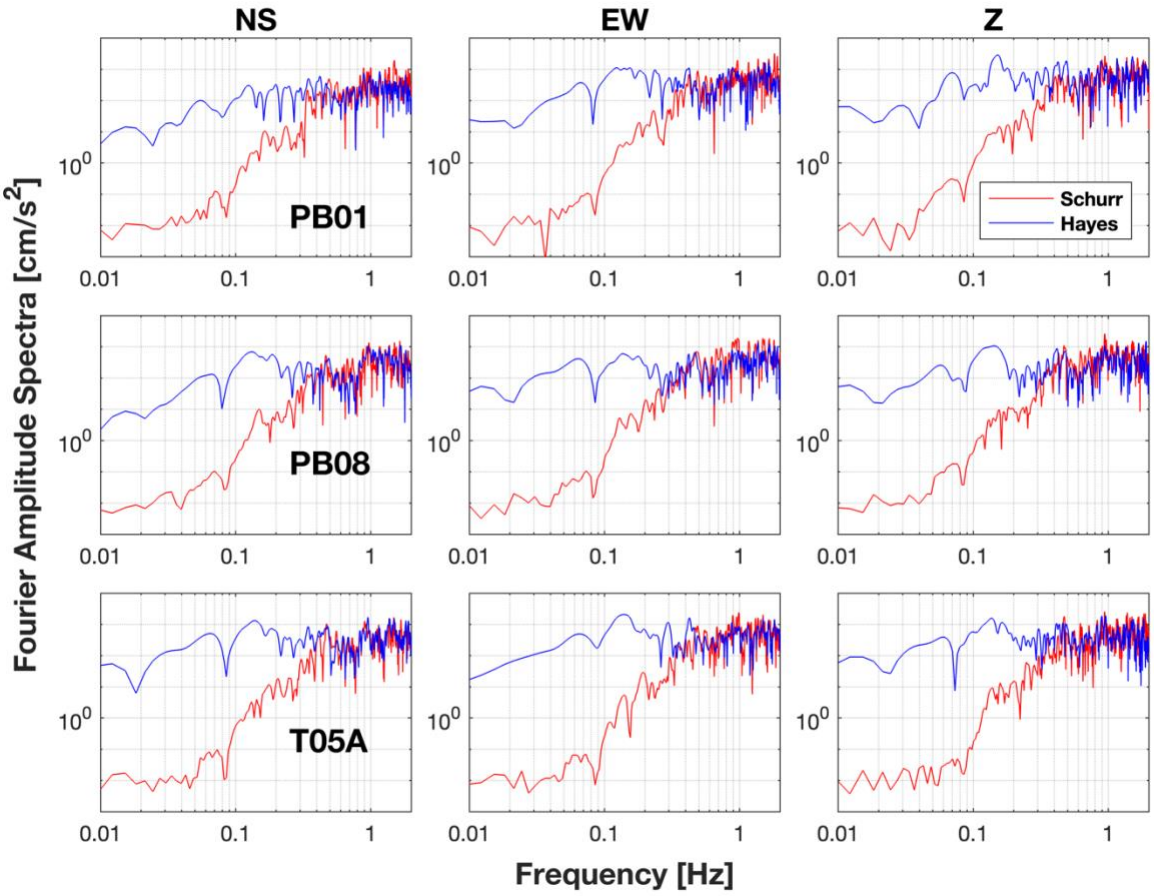

Figura 4.1. Espectros de Amplitud de Fourier para aceleraciones sintéticas 3D-FEM en bajas frecuencias (0.01 a 2.0 Hz) considerando los modelos de distribución espacial de slip co-sísmico de Schurr *et al.* (2014) y Hayes *et al.* (2014), en tres estaciones (PB01, PB08 y T05A).

4.3. Metodología Estocástica

Las series de tiempo de los *strong-motions* en altas frecuencias en sus tres componentes (P, SV y SH) vertical y horizontales, respectivamente, se desarrollaron mediante una

metodología estocástica, siguiendo lo descrito por Ojeda *et al.*, (2021); Ruiz *et al.*, (2018); y Otarola *and* Ruiz (2016). Dentro de esta técnica, se incluyen factores de: patrón de radiación de ondas, $\mathcal{R}$, forma funcional del espectro de desplazamiento $\omega^{-\gamma}$, frecuencia de esquina dinámica, f_{cij},, atenuación inelástica, Q(f), atenuación en altas frecuencias a través de kappa, κ_0, y funciones de amplificación $Amp(f)$, todos estos descritos en la sección 3.2.2.

El factor κ_0 que representa una atenuación somera dentro de la corteza terrestre para las ondas sísmicas y decrece proporcionalmente a medida que decrecen los valores de las velocidades de onda V_{S30}. Este es un parámetro sensible dentro de la forma de decaimiento de la atenuación de los Espectros de Amplitud Fourier resultantes de la simulación estocástica.

4.4. Parámetros de input en las modelaciones numéricas basadas en la física (PBSs)

Dentro de las técnicas empleadas para las simulaciones en bajas y altas frecuencias, se ha empleado un modelo de velocidades de ondas sísmicas V_P y V_S, para corteza y manto terrestres, extrapolado de los modelos descritos por Comte *et al.*, (2016) y Gao and Tilmann (2021).

En fuente sismogénica se adoptó un modelo de ruptura de fuente de falla finita, combinando la ubicación del hipocentro, el modelo del slab anteriormente descrito, los slips cosísmicos obtenidos de inversiones de datos GPS propuesto por Schurr *et al.*, (2014), derivándose así, el strike, dip, rake, y área de cada subfalla dentro del megathrust.

La amplificación del sitio es un parámetro determinante que controla la forma de los registros de *strong-motions* durante la ocurrencia de un gran terremoto. Las simulaciones comprenden este fenómeno, y se lo evalúa a través de configuración de velocidades de ondas sísmica de cizalle (o corte) del subsuelo Vs, generalmente utilizando el promedio harmónico en los 30 metros superiores V_{S30}, o una función de transferencia para un rango de frecuencias determinado. Sin embargo, dada la escasez de datos de velocidades de onda de corte o valores

de V_{S30} en las ubicaciones de las estaciones sismológicas emplazadas en el norte de Chile y analizadas en este trabajo, sumado a la falta de funciones de transferencia propuestas, aquí se empleó la caracterización geofísica HVSR para cada estación analizada (Leyton *et al.*, 2018a; 2018b), con el propósito de caracterizar la amplificación de cada sitio. Las curvas de amplitudes HVSR vs frecuencia (periodo) funcionan como una función de transferencia (Ghofrani *et al.*, 3013) para las tres componentes definidos en un rango de frecuencias de 0.1 a 10 Hz (Figura 3.4). Adicionalmente, se emplearon valores actualizados de κ_0 para la zona de subducción chilena, reportados en Pozo *et al.,* (2022) y Cárdenas *et al.,* (2024, en revisión).

4.5. Series de Tiempo de Banda Ancha

Para generar las formas de aceleraciones sísmicas del Terremoto de Iquique 2014 (8.2M_W) en el rango de frecuencias comprendido entre 0.01 y 30 Hz, se emparejaron las series de tiempo previamente desarrolladas para bajas y altas frecuencias utilizando el procedimiento de *match-filtering* que incluye un filtro de Butterwoth de segundo orden, descritos en la sección 3. Las figuras 3.9 y 3.10 muestran las formas de los acelerogramas y de las aceleraciones espectrales resultantes de la PBSs para los *strong-motions*, respectivamente.

El denominado filtrado de coincidencias o solapamiento (*match-filtering*) para simulaciones híbridas de banda ancha se realiza aplicando primero un filtro de paso bajo a los movimientos de baja frecuencia, aplicando después un filtro de paso alto a los movimientos de alta frecuencia y sumando finalmente los movimientos filtrados para obtener un resultado de banda ancha, los filtros que se utilizan corresponde a los de tipo Butterworth de N-orden con fase cero (*N^{th}-order zero-phase Butterworth filters*), donde, existe un criterio para que este enfoque funcione adecuadamente, que exige que los espectros de amplitud o los espectros de potencia de los filtros de paso alto y bajo sumen la unidad en todas las frecuencias, una ventaja adicional de este método corresponde a que los filtros son de fase cero, por lo que no se produce desplazamiento de la fase en la respuesta filtrada (Graves, 2023 personal communication, Graves and Pitarka, 2010; 2004). El proceso de *match-filterin*g utilizado para combinar dos

series temporales en una única serie temporal de banda ancha, utilizando el álgebra, puede escribirse en el dominio de frecuencias como:

$$A_{BB}(\omega) = F_{HP}(\omega)A_{H}(\omega) + F_{LP}(\omega)A_{L}(\omega) \qquad (4.1)$$

donde, $A_{BB}(\omega)$, $A_{H}(\omega)$ y $A_{L}(\omega)$ son las transformadas de Fourier de valor complejo de la serie temporal y $F_{HP}(\omega)$ y $F_{LP}(\omega)$ son las transformadas de Fourier de valor complejo de los operadores de filtro. Separando cada uno de los términos de la ecuación anterior en su espectro de amplitud y fase se obtiene (R):

$$R_{BB}(\omega)e^{-i\phi_{BB}(\omega)} = R_{HP}(\omega)e^{-i\phi_{HP}(\omega)}R_{H}(\omega)e^{-i\phi_{H}(\omega)} + R_{LP}(\omega)e^{-i\phi_{LP}(\omega)}R_{L}(\omega)e^{-i\phi_{L}(\omega)} \qquad (4.2)$$

Esta expresión puede simplificarse suponiendo que los espectros de fase de los filtros son iguales [$\phi_{HP}(\omega) = \phi_{LP}(\omega) = \phi_{F}(\omega)$], quedando:

$$[R_{HP}(\omega)\cos\phi_{H}(\omega) + R_{LP}(\omega)\cos\phi_{L}(\omega)]^2 + [R_{HP}(\omega)\sin\phi_{H}(\omega) + R_{LP}(\omega)\sin\phi_{L}(\omega)]^2 = 1 \qquad (4.3)$$

Lo que puede simplificarse aún más realizando un poco de álgebra y utilizando la identidad $\cos(\alpha - \beta) = \cos\alpha\cos\beta + \text{sen}\,\alpha\,\text{sen}\,\beta$, lo que da:

$$R_{HP}^2(\omega) + R_{LP}^2(\omega) + 2R_{HP}(\omega)2R_{LP}(\omega)\cos[\phi_{H}(\omega) - \phi_{L}(\omega)] = 1 \qquad (4.4)$$

Es bastante común que los espectros de fase de las series de alta y baja frecuencia de entrada no sean iguales. De hecho, la diferencia en los espectros de fase puede variar significativamente no sólo en la gama de frecuencias de interés, sino también en múltiples realizaciones de la simulación. En este caso, el valor esperado del término coseno tenderá a su media, es decir, $(\cos\phi) = 0$, lo que da:

$$R_{HP}^2(\omega) + R_{LP}^2(\omega) = 1 \qquad (4.5)$$

Para juntar los espectros de amplitud simulados en bajas y altas frecuencias, primero se utilizaron filtros de fase cero y se aproxima al requisito de que los espectros de amplitud o de potencia de los filtros individuales sumen la unidad (ecuación 4.5), luego, esto se consigue especificando filtros de esquina de paso alto (f_{H}) y paso bajo (f_L) que se desvían ligeramente de la frecuencia de solapamiento o cruce f_m.

$$R_{\mathrm{HP}}(f) = (f/f_H)^{2n}[1 + (f/f_H)^{2n}]^{-1} \qquad (4.6)$$

$$R_{\mathrm{LP}}(f) = [1 + (f/f_L)^{2n}]^{-1} \qquad (4.7)$$

Donde el requisito es que los filtros de esquina sean simétricos (en el dominio logarítmico) con respecto a la frecuencia de solapamiento, es decir, $f_H = \alpha f_m$ y $f_L = f_m/\alpha$, y, además, la restricción de que la suma de los espectros de amplitud o de potencia de los filtros para que sea la unidad exactamente en la frecuencia de solapamiento, da como resultado las siguientes expresiones para las esquinas de paso alto y bajo.

$$f_H = f_m[\sqrt{2} - 1]^{1/(2n)} \qquad (4.8)$$

$$f_L = f_m[\sqrt{2} - 1]^{-1/(2n)} \qquad (4.9)$$

La respuesta de amplitud de este método cuando se utilizan las ecuaciones 4.8 y 4.9, para especificar las esquinas de paso alto y bajo es cercana a la unidad incluso dentro de la zona de transición alrededor de la frecuencia de adaptación o solapamiento. En este trabajo el emparejamiento se lo realizó aplicando un filtro Butterworth de 2$^{\mathrm{do}}$ orden con fase cero (*2th-order zero-phase Butterworth filter*), y sumando las historias de tiempo en bajas y altas frecuencias simuladas en un rango de frecuencias de cruce o solapamiento comprendidas entre 0.75 Hz a 1.1 Hz.

En la Figura 3.12, se muestran cómo se comportan los valores de las intensidades sísmicas observadas (IM_{obs}) para el Terremoto de Iquique 2014 ($8.2M_W$), comparadas con las intensidades sísmicas aquí obtenidas mediante las simulaciones PBSs, estas dos, comparadas con los modelos empíricos de GMPMs propuestos por Montalva *et al.,* (2017) y Parker *et al.*, (2022). Donde se observa que las intensidades PBSs muestran un buen ajuste en relación con las IM_{obs} registradas durante el evento, además que las intensidades PBSs caen en un rango más acotado por debajo de los valores de ±1 desviación estándar (σ) de los modelos GMPM. El nivel desajuste entre las intensidades PBS y los modelos GMPMs, se lo evalúa por medio de sus residuales totales (Figura 3.13), en donde se aprecia que, en la región del campo cercano, R_{rup} < 70 km, los valores residuales resultantes de las intensidades PBS son ligeramente menores que los valores de residuales de GMPMs, mejorando la predicción de intensidades, validando las simulaciones basadas en la física del terremoto (PBSs). Mientras que, para la zona de R_{rup} > 70 km, los valores residuales tanto de las PBSs y GMPMs no muestran mayores diferencias.

Los residuales intra-eventos (δW_{es}) obtenidos a partir del GMPM de Parker *et al.* (2022), y de los resultados PBSs de este trabajo para el Terremoto de Iquique 2014, contrastados con el rango de frecuencias de banda ancha para las 10 estaciones consideradas (*Table 3.1*), se observan en la Figura 4.2. Donde, para las simulaciones PBSs el rango de bajas frecuencias (f < 1 HZ) se tienen valores de residuales δW_{es} de hasta $\pm$ 1.22, indicando un desajuste más marcado con relación a los valores obtenidos de Parker *et al.* (2022), mostrando que la incertidumbre está controlada por la cantidad y variación de parámetros físicos involucrados en la simulación del fenómeno de terremoto (i.e., slip co-símico, Tr, velocidad de ruptura, reología y geometría de las capas geológicas del megathrust, etc.), es decir, que mientras mayor cantidad de parámetros físicos que se puedan incorporar dentro del modelamiento numérico, ayudaría a ir mejorando o reduciendo estos niveles de incertidumbre, que demás, en este trabajo se produce por la capacidad computacional para la ejecución del modelo 3D-FEM, ya que a mayor cantidad de parámetros mayores tiempo de compilación en el supercomputador para las bajas frecuencias. Por otro lado, un modelo GMPM, está generando un menor desajuste en esa región considerando se nutren de datos registrados en eventos ocurridos y son capaces mantener una buena

estimación. Para las altas frecuencias (f > 1 Hz), en cambio los registros PBSs mantienen valores bajos de δW_{es} en relación con el GMPM, disminuyendo el nivel de desajuste, esto se debe a que, en esa región dentro de la metodología utilizada, se aplicó la técnica estocástica que involucra más parámetros físicos para la generación sintética del terremoto (e.g., stress drop, κ_0, factores de calidad y dispersión geométrica del patrón de trayectoria de ondas, etc.).

Las variaciones de residuales δW_{es} mencionadas tanto para las bajas y altas frecuencias, son evidenciadas también en la Figura 4.3, donde se muestra como varían sus desviaciones estándar ($\sigma_{\delta Wes}$). Finalmente, la reducción más notable de valores se produjo en el rango de entre 2 a 100 Hz (14.9% hasta 53.9%) relacionado con la metodología estocástica, y en la zona de frecuencias menores a 2 Hz no es notoria una reducción de valores residuales, debido a que la metodología cinemática aquí adoptada (3D-FEM) para ese rango requiere cada vez mas de mayores parámetros para generar la ruptura basada en la física del fenómeno y mayor capacidad computacional, con el propósito además de lograr alcanzar inclusive frecuencias superiores a los 2 Hz.

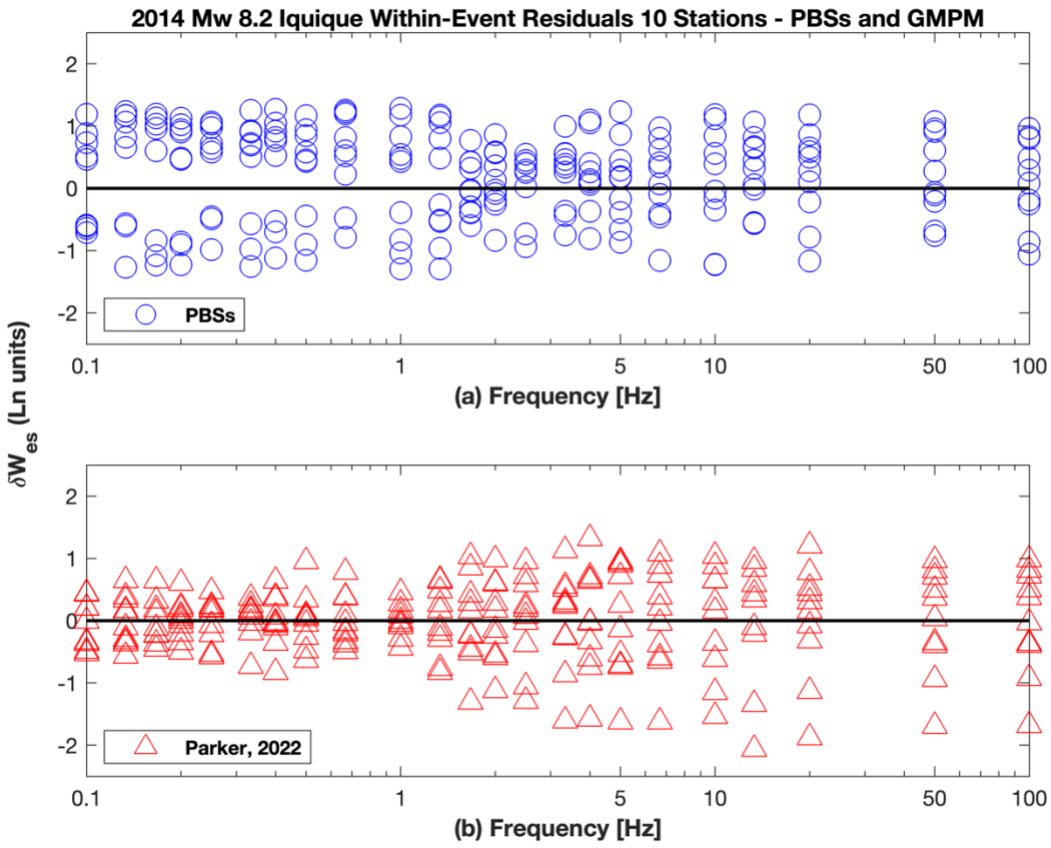

Figura 4.2. Residuales intra-eventos (Within-event residuals - δW_{es}) versus frecuencia, para las 10 estaciones analizadas en este trabajo (*Table 3.1*): (a) Modelo PBSs híbrido; (b) Modelo GMPM de Parker *et al*. (2022), para el Terremoto de Iquique 2014 (8.2Mw).

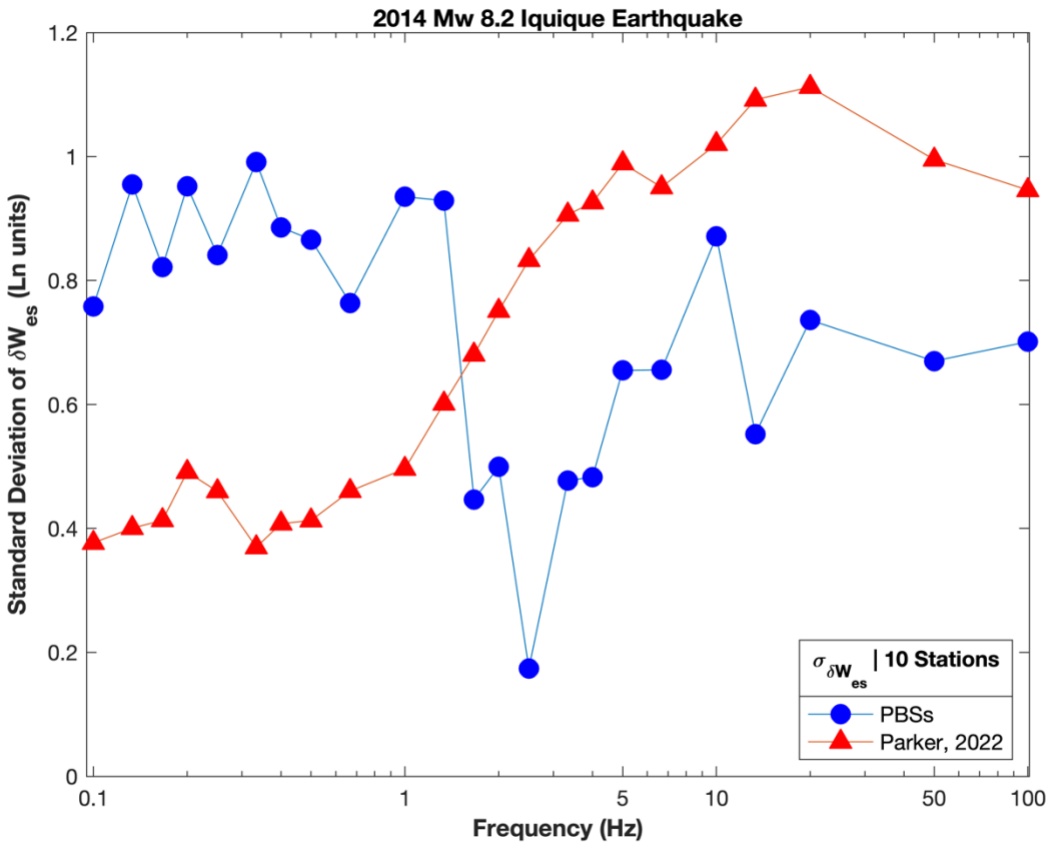

Figura 4.3. Desviación estándar de los residuales intra-eventos ($\sigma_{\delta Wes}$) comparada con la frecuencia, en las 10 estaciones analizadas en este trabajo (*Table 3.1*), para los modelos PBSs híbrido y GMPM de Parker *et al.* (2022), para el Terremoto de Iquique 2014 (8.2Mw).

Adicionalmente, al comparar las $\sigma_{\delta Wes}$ de las simulaciones PBSs y el modelo GMPM (Parker *et al.*, 2022) para el Terremoto de Iquique 2014, con la distancia mínima entre la ruptura y la estación (R_{rup}) en las 10 estaciones consideradas en la Tabla 3.1 (ver Figura 4.4), se aprecia que los valores de $\sigma_{\delta Wes}$ obtenidos en la simulaciones PBSs arrojan valores menores en la región del campo cercano a la fuente sismogénica (primeros ~ 30 a 70 km de distancia), con relación a los valores del modelo GMPM, esto se debe a que la metodología híbrida que combina técnicas determinística y estocástica, captura de una manera más completa parámetros involucrados en la física del fenómeno de terremoto, mejorando la confiabilidad de sus resultados en el campo cercano. Los valores de

residuales PBS contrastados con los del GMPM, se redujeron entre un 2.6% hasta 10.23% para las más cortas distancias R_{rup} equivalentes a los primeros ~30 a 70 km.

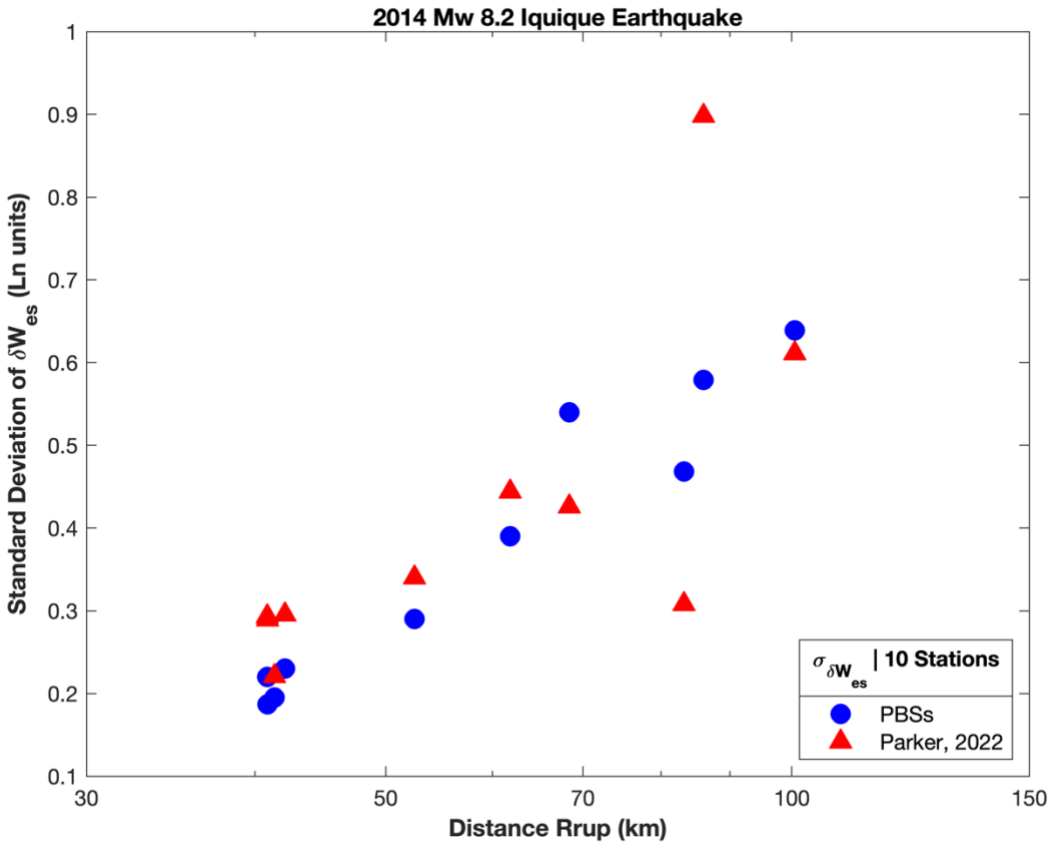

Figura 4.4. Desviación estándar de los residuales intra-eventos ($\sigma_{\delta Wes}$) comparada con la distancia mínima entre la ruptura y la estación (R_{rup}) en las 10 estaciones analizadas en este trabajo (*Table 3.1*), para los modelos PBSs híbrido y GMPM de Parker *et al.* (2022), para el Terremoto de Iquique 2014 (8.2Mw).

4.5.1. Ejemplo de cálculo del Evaluación Probabilística de la Amenaza Sísmica (Probabilistic Seismic Hazard Assessment – PSHA)

Aquí se presenta un ejemplo simplificado de cálculo curvas de amenaza sísmica, siguiendo una metodología probabilística (PSHA), incorporando los resultados de las PBSs en banda ancha para un registro de *strong-motions* en un sitio específico (*single site*),

simultáneamente con una estimación ergódica convencional. Los parámetros sísmicos que se definen a continuación se obtuvieron parcialmente de Ríos (2015) y Leyton *et al.* (2010):

- Área de ruptura afectada por la sismicidad 100 x 100 km
- Truncamiento de la distribución exponencial de M_W ($\boldsymbol{\lambda} = 0.74$)
- Tasa de actividad de 0.34 para M_W entre 4.5 y 8.2

Se ha seleccionado el sitio de ubicación de la estación T05A con coordenadas 20.21° S y 70.15°W, con una velocidad V_{S30} de 809 m/s, y distancia R_{rup} = 40.83 km. Dentro del ejemplo se examinan las predicciones *de strong*-motions y las curvas de amenaza sísmica para el *peak ground acceleration* (PGA). En la Figura 4.5 se observan las curvas de amenaza ergódica y para el caso de sitio específico (*single site*). Donde, para la condición ergódica se utiliza la mediana de la predicción GMPM (Montalva *et al.*, 2017) y su correspondiente desviación estándar, no obstante, para el caso de sitio específico la desviación estándar, σ_{S2S}, involucrada con los residuales *site-to-site* (δ_{S2S}) es posible considerarla casi nula, dada la amplificación del sitio en la simulación estocástica (HVSR y κ_0), además, es posible disminuir el parámetro τ (incertidumbre aleatoria relacionada con la variación entre eventos) mediante el uso de las PBSs asociadas al método cinemático, pero sería utilizable solo en bajas frecuencias. Adicionalmente, se observa una reducción de los valores PGA para periodos de retorno, T, altos (475 y 2500 años), es decir, para el T = 475 años, el valor de PGA se reduce alrededor de un 50%, al comparar datos PBs con ergódicos.

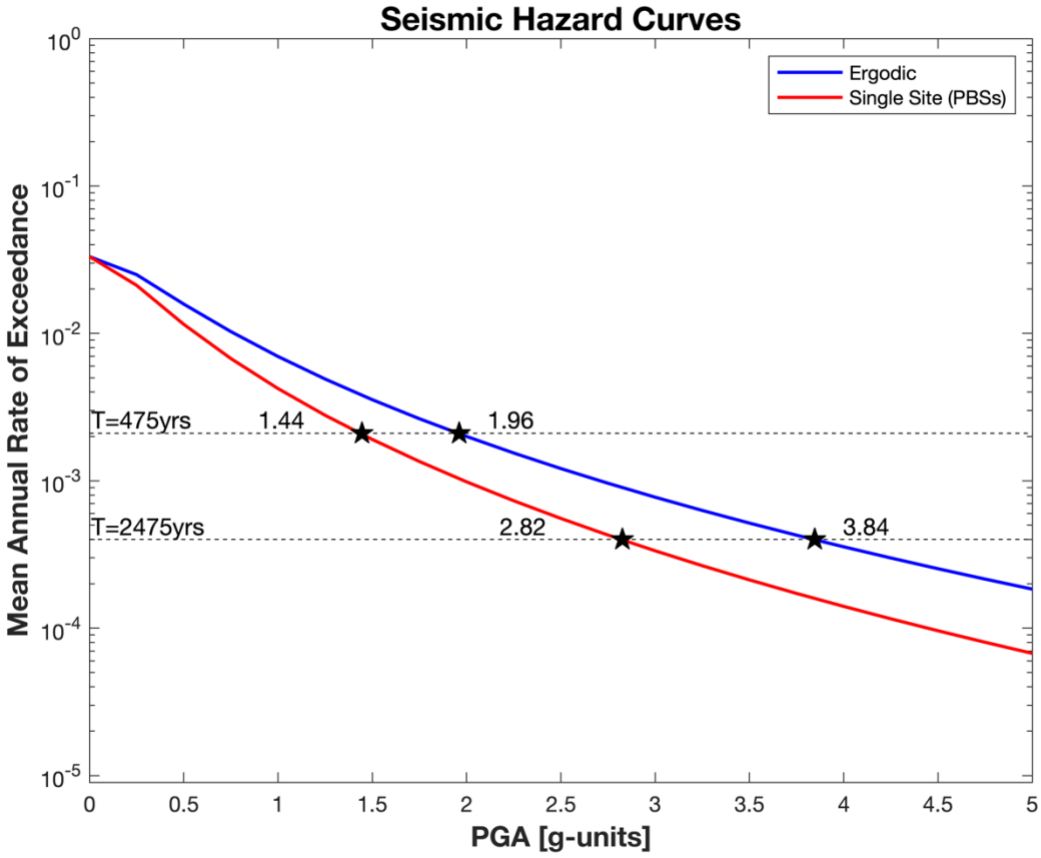

Figura 4.5. Curvas de Amenaza Sísmica, para condiciones ergódica y de sitio específico (*single site*).

El modelo GMPM utilizado para la curva ergódica considera factores lineales para la amplificación del sitio, mientras que en la metodología utilizada aquí los efectos de amplificación del terreno tienen consideraciones no solamente lineales, sino que incorpora curvas HVSR emulando la función de transferencia y el factor de decaimiento espectral κ_0, logrando la reducción de valores de diseño, en el caso de análisis para un periodo corto (alta frecuencia) PGA.

Recapitulando, se ha obtenido series de tiempo sintéticas de movimientos fuerte del terreno (*strong-motions*) de banda ancha para el Terremoto de Iquique 8.2M_W desencadenado

en el norte de la zona de subducción chilena. Los acelerogramas simulados se reprodujeron para 10 estaciones sismológicas ubicadas sobre roca que registraron el evento, situadas entre los 38.8 km y 141.56 km de la distancia mínima entre la ruptura y la estación (R_{rup}).

CAPÍTULO V. Conclusiones

- La complejidad geológica de un megathrust impidió alcanzar el contenido de movimiento fuerte del terreno de alta frecuencia (f >1 Hz) utilizando sólo la metodología de simulación 3D-FEM, por lo tanto, se desarrolló el enfoque híbrido, es decir, utilizando tanto el método estocástico como el 3D-FEM para completar toda la serie temporal de aceleración de banda ancha para los tres componentes (NS, EW, Z), fusionando los rangos LF y HF para cada componente ortogonal.

- En este estudio se detectó que el *rise time*, Tr, es un parámetro crítico dentro de la simulación de ruptura cinemática de fuente sismogénica de grandes terremotos de megathrust, razón por la cual, a partir del análisis de 45 Modelos de Ruptura de Falla Finita para la fuente sismogénica, generados a partir de 23 grandes terremotos de subducción alrededor del mundo con magnitudes comprendidas entre 7.3 y 9.2 M_W, se realizaron regresiones lineales sobre dos subconjuntos de datos (Cárdenas *et al.*, 2023).

- Los valores del Tr examinados en este estudio se centran específicamente en los terremotos de gran magnitud de la zona de subducción. Los resultados indican que los valores del *rise time* tienden a ser relativamente más cortos para los modelos de ruptura derivados de datos telesísmicos, observándose valores ligeramente más largos para los modelos derivados de datos de SGM.

- El valor de la pendiente de Tr obtenido para la regresión de SGM en nuestro estudio es de 0.36 con una precisión de aproximadamente el 16%; esto se alinea con los valores de pendiente de Tr de Gusev and Chebrov (2019) igual a 0.33, y Melgar and Hayes (2017), con un valor de 0.29. Además, las estaciones telesísmicas se encuentran a distancias mucho mayores de la fuente del terremoto en comparación con las estaciones SGM locales, lo que puede dar lugar a mayores efectos de atenuación en las ondas sísmicas que muestran una menor resolución de slip, aumentando la duración de la ruptura de la

fuente (Yokota *et al*., 2011; Kurahashi and Irikura, 2011), también reportado por Gusev and Chebrov (2019). Esto indica que las inversiones de solo datos teleseísmicos pueden tender a sobreestimar las características temporales de la fuente en comparación con los datos de movimiento fuerte del suelo de alta frecuencia de las estaciones sísmicas situadas cerca del epicentro del terremoto.

- La cantidad de modelos de ruptura determinados por datos SGM es todavía relativamente baja en comparación con el tamaño de la base de datos global. Con una mejor cobertura de SGM en el futuro, una mayor densidad de estaciones y, por tanto, un número significativamente mayor de modelos de ruptura SGM disponibles para su estudio, será posible refinar aún más las relaciones de escala del parámetro de tiempo de subida (Tr) y determinar cómo puede afectar a este parámetro las diferentes técnicas de inversión de fuentes.

- Los resultados muestran la importancia de las redes de SGM para que los estudios incorporen con precisión el escalado del tiempo de subida (Tr) en las simulaciones de *strong-motions* de banda ancha para futuros terremotos de subducción de gran magnitud.

- La técnica híbrida permitió obtener series temporales simuladas de banda ancha comprendidas entre 0.01 y 30 Hz. Lamentablemente, las zonas de *High-Frequency Strong-Motions-Generations-Areas* no fueron posibles de caracterizar (fuera de alcance).

- El trabajo realizado tiene algunas limitaciones, mostradas en la evaluación del error mediante el *Bias Model* apreciándose una subestimación para períodos > 1 s (es decir, f < 1 Hz) esto es consecuencia del tamaño de dominio muy grande de malla del 3D-FEM y el tamaño mínimo de elemento (*e*) alrededor de ~ 200 a 300 m diseñados para que permitan el paso de la más alta frecuencia posible (i.e. 1.5 Hz), con lo que se requirió de tiempos de ejecución muy grandes. Adicionalmente, la configuración del modelo de

velocidades corticales fue derivado de los trabajos de Gao and Tilmann (2021), y Comte *et al*. (2016), donde tienen su más alta resolución en zonas mayores a 5 km de profundidad.

- Para mejorar la evaluación de la amplificación del emplazamiento, en este trabajo se introdujeron los coeficientes HVSR en lugar de Funciones de Transferencia definidas para cada estación, los coeficientes HVSR se obtuvieron siguiendo las recomendaciones indicadas en Leyton et al. (2018a; 2018b), utilizando las curvas de amplitudes HVSR vs. frecuencia (periodo), y los resultados se muestran satisfactorios.

- Los *strong-motions* simulados para un rango de frecuencias de banda ancha (PBSs) en las estaciones seleccionadas se comparan con los registros observados, donde se observa valores bajos de sus residuales totales (ver figura 3.13) indicando un bajo desajuste, además, la estrecha coincidencia entre los valores máximos simulados y los valores correspondientes obtenidos de las curvas de aceleraciones espectrales (ver figura 3.10), dan cuenta de un modelado físicamente razonable de la fuente, propagación y sitio a pesar de las incertidumbres existentes en el megathust. Finalmente, el nivel de desajuste de los residuales de las intensidades PBS, es menor en el rango de campo cercano, $R_{rup} \leq 70$ km, con relación a los residuales de las intensidades obtenidas de los GMPMs aquí analizados, y futuras simulaciones, este podría reducirse mucho más.

- La configuración y distribución espacial de los datos de slip co-sismico para la ruptura cinemática de la fuente sismogénica, al ser evaluadas a través de los espectros de amplitud de Fourier entre 0.01 y 2 Hz (ver Figura 4.1), considerando los modelos de: Schurr, *et al.* (2014); y Hayes, *et al.* (2014). Se genera una mayor variación para frecuencias muy bajas ($f < 0.2$ Hz), mientras que para las frecuencias, $f > 0.2$ Hz, no existe mayor variabilidad, entre ambos modelos de slip, logrando que modelos de distribución de slip/slip-déficit racionales para rupturas de grandes terremotos sean plausibles dentro de las simulaciones basadas en la física de terremotos (PBSs).

- Al contrastar los valores de la desviación estándar de residuales intra-eventos ($\sigma_{\delta \mathrm{Wes}}$) para los *strong-motions* simulados por PBSs con los del modelo de predicción GMPM, en el dominio de las frecuencias (ver Figuras 4.2 y 4.3), se aprecia que la reducción porcentual más notable que varía entre 14.9% hasta 53.9%, se produjo en el intervalo de 2.0 a 100.0 Hz, rango relacionado con la metodología estocástica, y en la zona de frecuencias menores a 2.0 Hz no es notoria una reducción de valores residuales, debido a que la metodología cinemática adoptada en ese rango requiere cada vez mas de mayores parámetros para generar la ruptura basada en la física del fenómeno. Adicionalmente, al evaluar los valores de $\sigma_{\delta \mathrm{Wes}}$ para las distancias entre la fuente y ubicación de cada estación, R_{rup}, estos valores muestran su mayor reducción porcentual, de 2.6% hasta 10.23%, en la región del campo cercano $R_{rup} \approx 30$ a 70 km (ver Figura 4.4).

- Las estimaciones de los términos de emplazamiento mediante relaciones espectrales horizontales-verticales (HVSR) mejoran las predicciones de los *strong-motions*, como la reducción de valores de PGA en la curvas de amenaza sísmica *single site* (ver Figura 4.5), donde para el periodo de retorno de diseño de T = 475 años, el valor de PGA se reduce alrededor de un 50% al comparar las curvas de amenaza símica para sitio específico (PBSs) con la ergódica. En el caso de *strong-motions* PBSs híbridos, al incorporar parámetros de amplificación de sitio (HVSR y κ_0) le aporta un carácter no lineal, diferenciándose de las predicciones de modelos convencionales GMPM, además, las simulaciones PBSs ayudan a disminuir el parámetro τ dentro de modelos GMPM, relacionado a la incertidumbre aleatoria epistémica propia de las variaciones en los mecanismos y procesos de ruptura de la fuente sismogénica para distintos eventos en un mismo sitio.

- Para futuros análisis de grandes terremotos megathrust a través de PBSs, se recomienda utilizar modelos de *slip deficit*, relaciones de escalado de fuentes sismogénicas, modelos de velocidad más detallados en la zona somera de la corteza continental, que permitan

determinar y evaluar *strong-motions* para eventos no recurrentes, y que su credibilidad física presente poca incertidumbre.

REFERENCIAS

Aagaard, B., M. Knepley, C. Williams (2023a), *PyLith v4.0.0.* Davis, CA: Computational Infrastructure of Geodynamics. DOI: 10.5281/zenodo.10359667.

Aagaard, B. T., Knepley, M. G., & Williams, C. A. (2013). A domain decomposition approach to implementing fault slip in finite-element models of quasi-static and dynamic crustal deformation. *Journal of Geophysical Research: Solid Earth*, ***118*****(6)**, 3059-3079.

Aki, K., & Richards, P. G. (2002). *Quantitative seismology*.

Aki, K. (1966). Generation and propagation of G waves from the Niigata earthquake of June 16, 1964. Part 2. Estimation of earthquake moment, released energy, and stress-strain drop from the G wave spectrum, *Bull. Earthq. Res. Inst.* **44**, 73–88.

Akinci, A., Aochi, H., Herrero, A., Pischiutta, M., & Karanikas, D. (2017). Physics-based broadband ground-motion simulations for probable MW≥ 7.0 earthquakes in the Marmara Sea Region (Turkey). *Bulletin of the Seismological Society of America*, ***107*****(3),** 1307-1323.

Allen, T. I., & Hayes, G. P. (2017). Alternative rupture-scaling relationships for subduction interface and other offshore environments. *Bulletin of the Seismological Society of America*, ***107*****(3)**, 1240-1253.

Astroza, M., Ruiz, S., & Astroza, R. (2012). Damage assessment and seismic intensity analysis of the 2010 (Mw 8.8) Maule earthquake. *Earthquake Spectra*, ***28*****(1_suppl1)**, 145-164.

Atik, L. A., Abrahamson, N., Bommer, J. J., Scherbaum, F., Cotton, F., & Kuehn, N. (2010). The variability of ground-motion prediction models and its components. *Seismological Research Letters*, ***81*****(5)**, 794-801.

Bastías, N., & Montalva, G. A. (2016). Chile strong ground motion flatfile. *Earthquake Spectra*, ***32*****(4)**, 2549-2566.

Becerra, A., Sáez, E., Podestá, L., & Leyton, F. (2016). The 2014 earthquake in Iquique, Chile: Comparison between local soil conditions and observed damage in the cities of Iquique and Alto Hospicio. *Earthquake Spectra*, ***32*****(3),** 1489-1505.

Blaser, L., Krüger, F., Ohrnberger, M., & Scherbaum, F. (2010). Scaling relations of earthquake source parameter estimates with special focus on subduction environment. *Bulletin of the Seismological Society of America*, **100(6)**, 2914-2926.

Bradley, B. A., Bae, S. E., Polak, V., Lee, R. L., Thomson, E. M., & Tarbali, K. (2017). Ground motion simulations of great earthquakes on the Alpine Fault: effect of hypocentre location and comparison with empirical modelling. *New Zealand Journal of Geology and Geophysics*, ***60*****(3)**, 188-198.

Boore, D. M. (2003). Simulation of ground motion using the stochastic method. *Pure and applied geophysics*, ***160***, 635-676.

Cárdenas, D. R., Miller, M., & Montalva, G. A. (2024). Subduction Interface Earthquake Rise-Time Scaling Relations. *Bulletin of the Seismological Society of America*, ***114*****(1),** 278-290.

Cárdenas, D. R., Montalva, G. A., & Ruiz S. (2024). Hybrid Broadband Strong-Motions Uncertainties Simulations in the Near-Field Megathrust Earthquakes *Bulletin of the Seismological Society of America*, ***(in revison)***.

Catalán, P. A., Aránguiz, R., González, G., Tomita, T., Cienfuegos, R., González, J., ... & Gubler, A. (2015). The 1 April 2014 Pisagua tsunami: observations and modeling. *Geophysical Research Letters*, ***42*****(8)**, 2918-2925.

Cilia, M. G., Mooney, W. D., & Robinson, A. (2017). A Seismic Intensity Survey of the 1 April 2014 M 8.2 Iquique, Chile, Earthquake and Tsunami, and a Comparison with Strong-Motion Data. *Seismological Research Letters*, ***88*****(5)**, 1232-1240.

Comte, D., Carrizo, D., Roecker, S., Ortega-Culaciati, F., & Peyrat, S. (2016). Three-dimensional elastic wave speeds in the northern Chile subduction zone: variations in hydration in the supraslab mantle. *Geophysical Supplements to the Monthly Notices of the Royal Astronomical Society*, ***207*****(2)**, 1080-1105.

Fernández, J., Pastén, C., Ruiz, S., & Leyton, F. (2019). Damage assessment of the 2015 Mw 8.3 Illapel earthquake in the North-Central Chile. *Natural Hazards*, ***96***, 269-283.

Folesky, J., Kummerow, J., & Shapiro, S. A. (2021). Stress drop variations in the region of the 2014 MW8. 1 Iquique earthquake, northern Chile. *Journal of Geophysical Research: Solid Earth*, ***126*****(4)**, e2020JB020112.

Gao, Yajian; Tilmann, Frederik (2021): Seismic Velocity Model of Crust and Upper Mantle beneath the Central Andes. GFZ Data Services. https://doi.org/10.5880/GFZ.2.4.2021.005

Ghofrani, H., Atkinson, G. M., & Goda, K. (2013). Implications of the 2011 M9. 0 Tohoku Japan earthquake for the treatment of site effects in large earthquakes. *Bulletin of Earthquake Engineering*, *11*(1), 171-203.

Graves, R., & Pitarka, A. (2016). Kinematic ground-motion simulations on rough faults including effects of 3D stochastic velocity perturbations. *Bulletin of the Seismological Society of America*, ***106*****(5)**, 2136-2153.

Graves, R., & Pitarka, A. (2015). Refinements to the Graves and Pitarka (2010) broadband ground-motion simulation method. *Seismological Research Letters*, ***86*****(1)**, 75-80.

Graves, R. W., & Pitarka, A. (2010). Broadband ground-motion simulation using a hybrid approach. *Bulletin of the Seismological Society of America*, ***100*****(5A)**, 2095-2123.

Graves, R. W., & Pitarka, A. (2004, August). Broadband time history simulation using a hybrid approach.

Gusev, A. A., & Chebrov, D. (2019). On Scaling of Earthquake Rise-Time Estimates. *Bulletin of the Seismological Society of America*, ***109*****(6)**, 2741-2745.

Hartzell, S., & Langer, C. (1993). Importance of model parameterization in finite fault inversions: Application to the 1974 Mw 8.0 Peru earthquake. *Journal of Geophysical Research: Solid Earth*, ***98*****(B12)**, 22123-22134.

Hayes, G. P. (2017). The finite, kinematic rupture properties of great-sized earthquakes since 1990. *Earth and Planetary Science Letters*, ***468***, 94-100.

Hayes, G. P., Herman, M. W., Barnhart, W. D., Furlong, K. P., Riquelme, S., Benz, H. M., … & Samsonov, S. (2014). Continuing megathrust earthquake potential in Chile after the 2014 Iquique earthquake. *Nature*, ***512*****(7514)**, 295-298.

Herrero, A., & Bernard, P. (1994). A kinematic self-similar rupture process for earthquakes. *Bulletin of the Seismological Society of America*, ***84*****(4)**, 1216-1228.

Hicks, S. P., & Rietbrock, A. (2015). Seismic slip on an upper-plate normal fault during a large subduction megathrust rupture. *Nature Geoscience*, ***8*****(12)**, 955-960.

Ichinose, G., Somerville, P., Thio, H. K., Graves, R., & O'Connell, D. (2007). Rupture process of the 1964 Prince William Sound, Alaska, earthquake from the combined inversion of seismic, tsunami, and geodetic data. *Journal of Geophysical Research: Solid Earth*, ***112*****(B7).**

Kamae, K., Irikura, K., & Pitarka, A. (1998). A technique for simulating strong ground motion using hybrid Green's function. *Bulletin of the Seismological Society of America*, ***88*****(2)**, 357-367.

Kikuchi, M., Nakamura, M., & Yoshikawa, K. (2003). Source rupture processes of the 1944 Tonankai earthquake and the 1945 Mikawa earthquake derived from low-gain seismograms. *Earth, Planets and Space*, ***55*****(4)**, 159-172.

Kobayashi, H., Koketsu, K., Miyake, H., & Kanamori, H. (2021). Similarities and differences in the rupture processes of the 1952 and 2003 Tokachi-oki earthquakes. *Journal of Geophysical Research: Solid Earth*, ***126*****(1)**, e2020JB020585.

Kobayashi, R., & Koketsu, K. (2005). Source process of the 1923 Kanto earthquake inferred from historical geodetic, teleseismic, and strong motion data. *Earth, planets and space*, ***57*****(4)**, 261-270.

Koketsu, K., K. Hikima, S. I. Miyazaki, and S. Ide (2004). Joint inver-sion of strong motion and geodetic data for the source process ofthe 2003 Tokachi-oki, Hokkaido, earthquake, *Earth, Planets Space*, **56**, 329–334.

Konca, A. O., Avouac, J. P., Sladen, A., Meltzner, A. J., Sieh, K., Fang, P., ... & Helmberger, D. V. (2008). Partial rupture of a locked patch of the Sumatra megathrust during the 2007 earthquake sequence. *Nature*, ***456*****(7222)**, 631-635.

Kubota, T., Saito, T., & Hino, R. (2022). A new mechanical perspective on a shallow megathrust near-trench slip from the high-resolution fault model of the 2011 Tohoku-Oki earthquake. *Progress in Earth and Planetary Science*, ***9*****(1)**, 68.

Kurahashi, S., & Irikura, K. (2011). Source model for generating strong ground motions during the 2011 off the Pacific coast of Tohoku Earthquake. *Earth, planets and space*, ***63***, 571-576.

Lee, R. L., Bradley, B. A., Stafford, P. J., Graves, R. W., & Rodriguez-Marek, A. (2020). Hybrid broadband ground motion simulation validation of small magnitude earthquakes in Canterbury, New Zealand. *Earthquake Spectra*, ***36*****(2)**, 673-699.

León Ríos, S. S. (2015). Análisis de la distribución espacial de la sismicidad precursora y post sísmica del terremoto MW 8.1 de Iquique 2014 [*Tesis de Magíster, Universidad de Chile*].

Leonard, M. (2014). Self-consistent earthquake fault-scaling relations: Update and extension to stable continental strike-slip faults. *Bulletin of the Seismological Society of America*, ***104*(6)**, 2953-2965.

Leonard, M. (2010). Earthquake fault scaling: Self-consistent relating of rupture length, width, average displacement, and moment release. *Bulletin of the Seismological Society of America*, ***100*(5A)**, 1971-1988.

Leyton, F., Pastén, C., Ruiz, S., Idini, B., & Rojas, F. (2018a). Empirical site classification of CSN network using strong-motion records. *Seismological Research Letters*, ***89*(2A)**, 512-518.

Leyton, F., Leopold, A., Hurtado, G., Pastén, C., Ruiz, S., Montalva, G., & Saéz, E. (2018b). Geophysical characterization of the Chilean seismological stations: First results. *Seismological Research Letters*, ***89*(2A)**, 519-525.

Leyton, F., Ruiz, S., & Sepúlveda, S. A. (2010). Reevaluación del peligro sísmico probabilístico en Chile central. *Andean geology*, *37*(2), 455-472.

Liu, P., Archuleta, R. J., & Hartzell, S. H. (2006). Prediction of broadband ground-motion time histories: Hybrid low/high-frequency method with correlated random source parameters. *Bulletin of the Seismological Society of America*, ***96*(6)**, 2118-2130.

López-Comino, J. A., Stich, D., Ferreira, A. M., & Morales, J. (2015). Extended fault inversion with random slipmaps: a resolution test for the 2012 M w 7.6 Nicoya, Costa Rica earthquake. *Geophysical Journal International*, ***202*(3)**, 1505-1521.

Mai, P. M., and Thingbaijam, K. K. S. (2014). SRCMOD: An online database of finite-fault rupture models. *Seismological Research Letters*, **85(6)**, 1348-1357.

Mai, P. M., & Beroza, G. C. (2003). A hybrid method for calculating near-source, broadband seismograms: Application to strong motion prediction. *Physics of the Earth and Planetary Interiors*, ***137*****(1-4),** 183-199.

McCallen, D., Petersson, A., Rodgers, A., Pitarka, A., Miah, M., Petrone, F., … & Tang, H. (2021). EQSIM—A multidisciplinary framework for fault-to-structure earthquake simulations on exascale computers part I: Computational models and workflow. *Earthquake Spectra*, ***37*****(2)**, 707-735.

Melnick, D., Moreno, M., Quinteros, J., Baez, J. C., Deng, Z., Li, S., & Oncken, O. (2017). The super-interseismic phase of the megathrust earthquake cycle in Chile. *Geophysical Research Letters*, ***44*****(2)**, 784-791.

Melgar, D., & Hayes, G. P. (2017). Systematic observations of the slip pulse properties of large earthquake ruptures. *Geophysical Research Letters*, ***44*****(19)**, 9691-9698.

Mendoza, C. (1995). Finite-fault analysis of the 1979 March 14 Petatlan, Mexico, earthquake using teleseismic P waveforms. *Geophysical Journal International*, ***121*****(3)**, 675-683.

Mendoza, C., Hartzell, S., & Monfret, T. (1994). Wide-band analysis of the 3 March 1985 central Chile earthquake: Overall source process and rupture history. *Bulletin of the Seismological Society of America*, ***84*****(2)**, 269-283.

Mendoza, C. (1993). Coseismic slip of two large Mexican earthquakes from teleseismic body waveforms: Implications for asperity interaction in the Michoacan plate boundary segment. *Journal of Geophysical Research: Solid Earth*, ***98*****(B5)**, 8197-8210.

Montalva, G. A., Bastías, N., & Rodriguez-Marek, A. (2017). Ground-motion prediction equation for the Chilean subduction zone. *Bulletin of the Seismological Society of America*, ***107*****(2)**, 901-911.

Montalva, G. A., Chávez-Garcia, F. J., Tassara, A., & Jara Weisser, D. M. (2016). Site effects and building damage characterization in Concepción after the Mw 8.8 Maule earthquake. *Earthquake Spectra*, ***32*****(3)**, 1469-1488.

Moreno, M., Melnick, D., Rosenau, M., Baez, J., Klotz, J., Oncken, O., … & Hase, H. (2012). Toward understanding tectonic control on the Mw 8.8 2010 Maule Chile earthquake. *Earth and Planetary Science Letters*, ***321***, 152-165.

Moreno, M., Rosenau, M., & Oncken, O. (2010). 2010 Maule earthquake slip correlates with pre-seismic locking of Andean subduction zone. *Nature*, ***467*****(7312)**, 198-202.

Morales, D. (2016). Caracterización del periodo fundamental de vibración de edificios de muros de hormigón armado a partir de mediciones de vibraciones ambientales [*Tesis de Magíster, Universidad de Concepción*].

Murotani, S., Satake, K., & Fujii, Y. (2013). Scaling relations of seismic moment, rupture area, average slip, and asperity size for M~ 9 subduction-zone earthquakes. *Geophysical Research Letters*, ***40*****(19)**, 5070-5074.

Murotani, S., Miyake, H., & Koketsu, K. (2008). Scaling of characterized slip models for plate-boundary earthquakes. *Earth, planets and space*, **60(9)**, 987-991.

Nagai, R. (2001). Comparative study on the source processes of recurrent large earthquakes in Sanriku-oki region: The 1968 Tokachi-oki earthquake and the 1994 Sanriku-oki earthquake. *Zisin*, ***54***, 267-280.

Nakayama, W., & Takeo, M. (1997). Slip history of the 1994 Sanriku-Haruka-Oki, Japan, earthquake deduced from strong-motion data. *Bulletin of the Seismological Society of America*, *87*(4), 918-931.

Ojeda, J., Akinci, A., Tinti, E., Arriola, S., & Ruiz, S. (2021). Hybrid broadband strong-motion simulation to investigate the near-source characteristics of the M6. 5, 30 October 2016 Norcia, Italy earthquake. *Soil Dynamics and Earthquake Engineering*, ***149***, 106866.

Okuwaki, R., Yagi, Y., Aránguiz, R., González, J., & González, G. (2017). Rupture process during the 2015 Illapel, Chile earthquake: Zigzag-along-dip rupture episodes. *The Chile-2015 (Illapel) earthquake and tsunami*, 23-32.

Otarola, C., & Ruiz, S. (2016). Stochastic generation of accelerograms for subduction earthquakes. *Bulletin of the Seismological Society of America*, ***106*(6)**, 2511-2520.

Paolucci, R., Gatti, F., Infantino, M., Smerzini, C., Özcebe, A. G., & Stupazzini, M. (2018a). Broadband ground motions from 3D physics-based numerical simulations using artificial neural networks. *Bulletin of the Seismological Society of America*, ***108*(3A)**, 1272-1286.

Paolucci, R., Infantino, M., Mazzieri, I., Özcebe, A. G., Smerzini, C., & Stupazzini, M. (2018b). 3D physics-based numerical simulations: Advantages and current limitations of a new frontier to earthquake ground motion prediction. The Istanbul case study. In *Recent Advances in Earthquake Engineering in Europe: 16th European Conference on Earthquake Engineering-Thessaloniki 2018* **(pp. 203-223)**. Springer International Publishing.

Paolucci, R., Mazzieri, I., & Smerzini, C. (2015). Anatomy of strong ground motion: near-source records and three-dimensional physics-based numerical simulations of the M w 6.0 2012 May 29 Po Plain earthquake, Italy. *Geophysical Supplements to the Monthly Notices of the Royal Astronomical Society*, ***203*****(3)**, 2001-2020.

Parker, G. A., Stewart, J. P., Boore, D. M., Atkinson, G. M., & Hassani, B. (2022). NGA-subduction global ground motion models with regional adjustment factors. *Earthquake Spectra*, *38*(1), 456-493.

Pozo, I., Montalva, G., & Miller, M. (2023). Assessment of Kappa Values in the Chilean Subduction Zone for Interface and In-Slab Events. *Seismological Society of America*, ***94*****(1)**, 385-398.

Prieto, G. A., Shearer, P. M., Vernon, F. L., & Kilb, D. (2004). Earthquake source scaling and self-similarity estimation from stacking P and S spectra. *Journal of Geophysical Research: Solid Earth*, ***109*****(B8)**.

Rhie, J., Dreger, D., Bürgmann, R., & Romanowicz, B. (2007). Slip of the 2004 Sumatra–Andaman earthquake from joint inversion of long-period global seismic waveforms and GPS static offsets. *Bulletin of the Seismological Society of America*, ***97*****(1A)**, S115-S127.

Rodriguez-Marek, A., Montalva, G. A., Cotton, F., & Bonilla, F. (2011). Analysis of single-station standard deviation using the KiK-net data. *Bulletin of the Seismological Society of America*, ***101*****(3)**, 1242-1258.

Ruiz, S., Ojeda, J., Pastén, C., Otarola, C., & Silva, R. (2018). Stochastic Strong-Motion Simulation in Borehole and on Surface for the 2011 M w 9.0 Tohoku-Oki Megathrust Earthquake Considering P, SV, and SH Amplification Transfer Functions. *Bulletin of the Seismological Society of America*, ***108*****(5A)**, 2333-2346.

Ruiz, S., & Madariaga, R. (2018). Historical and recent large megathrust earthquakes in Chile. *Tectonophysics*, **733**, 37-56.

Ruiz, S., Metois, M., Fuenzalida, A., Ruiz, J., Leyton, F., Grandin, R., ... & Campos, J. (2014). Intense foreshocks and a slow slip event preceded the 2014 Iquique M w 8.1 earthquake. *Science*, ***345*(6201),** 1165-1169.

Salichon, J., B. Delouis, P. Lundgren, D. Giardini, M. Costantini, and P. Rosen (2003). Joint inversion of broadband teleseismic and interferometric synthetic aperture radar (InSAR) data for the slip history of the Mw = 7.7, Nazca ridge (Peru) earthquake of 12 November 1996, J. Geophys. Res. **108**, no. B2.

Silva, V., Amo-Oduro, D., Calderon, A., Costa, C., Dabbeek, J., Despotaki, V., ... & Pittore, M. (2020). Development of a global seismic risk model. *Earthquake Spectra*, ***36*(1_suppl)**, 372-394.

Schurr, B., Asch, G., Hainzl, S., Bedford, J., Hoechner, A., Palo, M., … & Vilotte, J. P. (2014). Gradual unlocking of plate boundary controlled initiation of the 2014 Iquique earthquake. *Nature*, ***512*(7514)**, 299-302.

Shao, G., X. Li, Q. Liu, X. Zhao, T. Yano, and C. Li (2010). A slip model of the Feb 27, 2010 Mw 8.9 Maule, Chile earthquake, in EGU General Assembly Conference Abstracts, 15704 pp. available at https://ji.faculty.geol.ucsb.edu/big_earthquakes/2010/02/27/chile_2_27.html (last accessed November 2023).

Skarlatoudis, A. A., Somerville, P. G., & Thio, H. K. (2016). Source-scaling relations of interface subduction earthquakes for strong ground motion and tsunami simulation. *Bulletin of the Seismological Society of America*, ***106*****(4)**, 1652-1662.

Skarlatoudis, A. A., Somerville, P. G., Thio, H. K., & Bayless, J. R. (2015). Broadband strong ground motion simulations of large subduction earthquakes. *Bulletin of the Seismological Society of America*, ***105*****(6)**, 3050-3067.

Sladen, A. , and Caltech (2007). Preliminary result 11/14/2007 (Mw 7.7), Tocopilla earthquake, Chile, Source Models of Large Earthquakes, available at http://www.tectonics.caltech.edu/slip_history/2007_tocopilla/tocopilla.html (last accessed November 2023).

Sladen, A., A. O. Konca, and Caltech (2007). Preliminary Result 09/12/2007 (Mw 7.9), Central Sumatra earthquake, Source Models of Large Earthquakes, available at http://www.tectonics .caltech.edu/slip_history/2007_c_sumatra/c-sumatra.html (last accessed November 2023).

Somala, S. N., Ampuero, J. P., & Lapusta, N. (2014). Resolution of rise time in earthquake slip inversions: Effect of station spacing and rupture velocity. *Bulletin of the Seismological Society of America*, ***104*****(6)**, 2717-2734.

Somerville, P., Irikura, K., Graves, R., Sawada, S., Wald, D., Abrahamson, N., ... & Kowada, A. (1999). Characterizing crustal earthquake slip models for the prediction of strong ground motion. *Seismological Research Letters*, ***70*****(1)**, 59-80.

Strasser, F. O., Arango, M. C., & Bommer, J. J. (2010). Scaling of the source dimensions of interface and intraslab subduction-zone earthquakes with moment magnitude. *Seismological Research Letters*, **81(6)**, 941-950.

Stupazzini, M., Infantino, M., Allmann, A., & Paolucci, R. (2021). Physics-based probabilistic seismic hazard and loss assessment in large urban areas: A simplified application to Istanbul. *Earthquake Engineering & Structural Dynamics*, ***50*(1)**, 99-115.

Taborda, R., & Bielak, J. (2014). Ground-motion simulation and validation of the 2008 Chino Hills, California, earthquake using different velocity models. *Bulletin of the Seismological Society of America*, ***104*(4),** 1876-1898.

Taborda, R., & Bielak, J. (2013). Ground-motion simulation and validation of the 2008 Chino Hills, California, earthquake. *Bulletin of the Seismological Society of America*, ***103*(1)**, 131-156.

Tassara, A., & Echaurren, A. (2012). Anatomy of the Andean subduction zone: three-dimensional density model upgraded and compared against global-scale models. *Geophysical Journal International*, ***189*(1)**, 161-168.

Tsuda, K. (2021). Dynamic Rupture Study of Near-Field Velocity Pulses during the 2016 Kumamoto Earthquake, Japan. *Bulletin of the Seismological Society of America*, ***111*(5)**, 2546-2558.

Wald, D. J., & Somerville, P. G. (1995). Variable-slip rupture model of the great 1923 Kanto, Japan, earthquake: Geodetic and body-waveform analysis. *Bulletin of the Seismological Society of America*, ***85*(1)**, 159-177.

Wei, S. (2014). Apr./0.1/2014 (Mw 8.1), Iquique, Chile. Source models of large earthquakes, available at http://www.tectonics.caltech.edu/slip_history/2014_chile/index.html (last accessed November 2023).

Wessel, P., W. H. F. Smith, R. Scharroo, J. Luis, F. Wobbe (2013). Generic Mapping Tools: Improved Version Released. *Eos Trans*. AGU **94(45)**, 409.

Yagi, Y., & Fukahata, Y. (2011). Rupture process of the 2011 Tohoku-Oki earthquake and absolute elastic strain release. *Geophysical Research Letters*, ***38*(19)**.

Yagi, Y. (2004). Source rupture process of the 2003 Tokachi-oki earthquake determined by joint inversion of teleseismic body wave and strong ground motion data. *Earth, planets and space*, ***56,*** 311-316.

Yamanaka, Y., & Kikuchi, M. (2003). Source process of the recurrent Tokachi-oki earthquake on September 26, 2003, inferred from teleseismic body waves. *Earth, Planets and Space*, ***55*(12)**, e21-e24.

Yokota, Y., Koketsu, K., Fujii, Y., Satake, K., Sakai, S. I., Shinohara, M., & Kanazawa, T. (2011). Joint inversion of strong motion, teleseismic, geodetic, and tsunami datasets for the rupture process of the 2011 Tohoku earthquake. *Geophysical Research Letters*, ***38*(7)**.

Yoshimoto, M., Watada, S., Fujii, Y., & Satake, K. (2016). Source estimate and tsunami forecast from far-field deep-ocean tsunami waveforms—The 27 February 2010 Mw 8.8 Maule earthquake. *Geophysical Research Letters*, ***43*(2)**, 659-665.

ANEXO 1. Material suplementario para el capítulo II

Supplementary S1.

Table 2.1. List of the earthquakes used in the present study and their source parameters.

Table 2.1 List of the earthquakes used in the present study and their source parameters.

	Location	Date	Seismic Moment (N·m)	M_w	Rupture Area (km^2)	Asperities Area (km^2)	Average Slip (m)	Maximum Slip (m)	Average T_r (s)	Average V_r (km/s)	Total Length (km)	Total Width (km)	Inversion Model	R_{min} (km)	Author
1	**Kanto, Japan**	Sep 01, 1923	1.46E+21	8.08	9100.0	1690.0	4.10	10.36	10.50	2.60	130.00	70.00	§ ‖	90	Kobayashi and Koketsu. (2005)*
2	**Kanto, Japan**	Sep 01, 1923	9.33E+20	7.95	9100.0	2210.0	2.53	7.71	8.00	3.00	130.00	70.00	‖ #		Wald and Somerville. (1995)*
3	**Tonankai, Japan**	Dec 07, 1944	1.31E+21	8.04	30800.0	4000.0	1.05	2.33	22.50	2.50	220.00	140.00	§ ‖	30	Ichinose *et al*. (2003)*
4	**Tonankai, Japan**	Dec 07, 1944	1.08E+21	7.99	11200.0	800.0	2.36	4.42	16.50	3.10	140.00	80.00	§	150	Kikuchi *et al*. (2003)*
5	**Tokachi-Oki, Japan**	Mar 04, 1952	4.80E+21	8.40	49725.0	10350.0	1.96	6.90	20.00	2.50	255.00	195.00	§ ‖	<50	Kobayashi *et al*. (2021)*
6	**Tokachi-Oki, Japan**	May 16, 1968	3.76E+21	8.35	28800.0	5200.0	2.41	9.29	12.00	1.90	240.00	120.00	§ ‖	80	Nagai *et al*. (2001)*
7	**Central Coast, Peru**	Oct 03, 1974	1.18E+21	8.01	42000.0	11202.2	0.85	4.83	20.00	3.00	250.00	168.00	‖		Hartzell and Langer. (1993)*
8	**Petatlan, Mexico**	Mar 14, 1979	1.37E+20	7.39	14400.0	3900.0	0.29	1.22	10.00	3.30	120.00	120.00	‖		Mendoza. (1995)*
9	**Playa Azul, Mexico**	Oct 25, 1981	8.49E+19	7.25	4200.0	925.0	0.49	4.04	1.00	2.60	60.00	70.00	‖		Mendoza. (1993)*
10	**Central Chile**	Mar 03, 1985	1.96E+21	8.16	42075.0	11250.0	0.79	3.29	14.00	3.00	255.00	165.00	§ ‖	10	Mendoza *et al*. (1994)*
11	**Sanrikuki, Japan**	Dec 28, 1994	4.92E+20	7.72	31521.0	5806.5	0.25	2.85	4.31	2.55	210.00	150.10	‖		Hayes. (2017)*
12	**Sanrikuki, Japan**	Dec 28, 1994	3.99E+20	7.70	15400.0	3199.5	0.71	4.03	12.00	2.40	110.00	140.00	§	<80	Nagai *et al*. (2001)*
13	**Sanrikuki, Japan**	Dec 28, 1994	7.49E+20	7.88	18700.0	4700.0	0.54	4.95	18.00	2.50	110.00	170.00	§	>100	Nakayama and Takeo. (1997) *
14	**Nazca Ridge, Peru**	Nov 12, 1996	4.61E+20	7.70	21000.0	5600.0	0.42	3.11	3.77	1.97	200.00	105.00	‖		Hayes. (2017)*
15	**Nazca Ridge, Peru**	Nov 12, 1996	6.57E+20	7.84	21600.0	5200.0	0.49	4.37	12.50	2.70	180.00	120.00	‖		Salichon *et al*. (2003)*
16	**Tokachi-Oki, Japan**	Sep 25, 2003	3.07E+21	8.24	61880.0	13104.0	0.80	7.75	4.85	2.02	272.00	227.50	‖		Hayes. (2017)*
17	**Tokachi-Oki, Japan**	Sep 25, 2003	2.70E+21	8.20	49725.0	9675.0	1.63	6.94	20.00	3.30	255.00	195.00	§ ‖	<50	Kobayashi *et al*. (2021)*
18	**Tokachi-Oki, Japan**	Sep 25, 2003	2.36E+21	8.21	12000.0	1600.0	3.11	7.06	15.00	3.60	120.00	100.00	§ ‖	50	Koketsu *et al*. (2004)*
19	**Tokachi-Oki, Japan**	Sep 25, 2003	1.92E+21	8.16	22100.0	4900.0	1.46	6.06	25.00	4.5	130.00	170.0	§ ‖	100	Yagi. (2004)*
20	**Tokachi-Oki, Japan**	Sep 26, 2003	1.25E+21	8.03	9600.0	3000.0	1.92	5.76	6.00	2.70	120.00	80.00	‖		Yamanaka and Kikuchi. (2003)*
21	**Tokachi-Oki, Japan**	Sep 25, 2003	3.60E+21	8.30	49725.0	10350.0	1.15	7.54	20.00	2.80	255	195	§ ‖#	<50	Kobayashi *et al*. (2021)*
22	**Sumatra, Indonesia**	Dec 26, 2004	7.15E+22	9.17	153422.1	50585.4	9.40	35.32	20.00	2.60	705.00	217.62	‖#		Rhie *et al*. (2007)*
23	**Sumatra, Indonesia**	Dec 26, 2004	7.69E+22	9.19	260295.5	72111.1	8.16	38.49	20.00	2.60	1355.00	192.10	‖#		Rhie *et al*. (2007)*
24	**Sumatra, Indonesia**	Mar 28, 2005	1.01E+22	8.59	209000.0	29480.0	1.49	9.25	6.44	2.12	836.00	250.00	‖		Hayes. (2017)*
25	**Pagai, Indonesia**	Sep 12, 2007	8.12E+20	7.86	36321.6	6204.9	0.34	5.66	4.15	2.27	224.00	162.15	‖		Hayes. (2017)*
26	**Pagai, Indonesia**	Sep 12, 2007	7.94E+20	7.90	45600.0	9720.0	0.37	6.00	2.20	2.20	240.00	190.00	‖		Konca *et al*. (2008)*
27	**Pagai, Indonesia**	Sep 12, 2007	7.94E+20	7.90	26400.0	5520.0	0.63	7.40	2.20	2.20	240.00	110.00	‖		Sladen and Konca. (Caltech, Pagai 2007)*

28	**Benkulu,Indonesia**	Sep 12, 2007	6.04E+21	8.44	112640.0	26628.1	0.80	6.78	8.11	2.21	352	320	ǁ	Hayes. (2017)†
29	**Pisco, Peru**	Aug 15, 2007	2.33E+21	8.17	61440.0	9812.5	1.10	6.38	6.69	1.38	384.00	160.00	ǁ	Hayes. (2017)*
30	**Tocopilla, Chile**	Nov 14, 2007	4.33E+20	7.68	24500.0	5512.5	0.45	3.67	3.87	2.35	200.00	122.50	ǁ	Hayes. (2017)*
31	**Tocopilla, Chile**	Nov 14, 2007	3.98E+20	7.70	20412.0	5913.0	0.88	3.80	1.60	1.60	162.00	126.00	ǁ	Sladen. (Caltech, Tocopilla 2007)*
32	**Maule, Chile**	Feb 27, 2010	2.51E+22	8.90	112200.0	29070.0	4.05	12.90	90.27	-	600.00	187.00	ǁ	Shao *et al*. (UCSB, Maule 2010)*
33	**Maule, Chile**	Feb 27, 2010	2.45E+22	8.85	186375.0	27512.5	5.14	16.96	5.90	2.11	1050.00	177.50	ǁ	Hayes. (2017)*
34	**Tohoku-Oki, Japan**	Mar 11, 2011	5.75E+22	9.11	100000.0	24800.0	12.59	51.21	1.20	2.80	500.00	200.00	ǁ	Yagi and Fukahata. (2011)*
35	**Tohoku-Oki, Japan**	Mar 11, 2011	4.79E+22	9.04	166000.0	27390.0	8.31	55.03	10.03	2.02	1250.00	132.80	ǁ	Hayes. (2017)*
36	**Costa Rica**	Sep 05, 2012	2.93E+20	7.57	8775.0	4550.0	0.43	2.51	3.94	3.05	450.00	19.50	ǁ	Hayes. (2017)*
37	**Costa Rica**	Sep 05, 2012	2.93E+20	7.60	10725.0	4160.0	0.54	2.72	3.00	2.50	150.00	71.50	ǁ	Lopez-Comino *et al*. (2015)*
38	**Offshore, El Salvador**	Aug 27, 2012	1.26E+20	7.32	14896.0	4088.0	0.27	1.53	4.02	1.74	152.00	98.00	ǁ	Hayes. (2017)*
39	**Iquique, Chile**	Apr 01, 2014	1.58E+21	8.10	45600.0	13350.0	0.67	4.21	44.64	-	285.00	160.00	ǁ	Wei. (Caltech, Iquique 2014)*
40	**Iquique, Chile**	Apr 01, 2014	2.49E+21	8.18	86400.0	9960.0	0.77	7.24	12.97	1.64	720.00	120.00	ǁ	Hayes. (2017)*
41	**Illapel, Chile**	Sep 16, 2015	2.91E+21	8.23	47520.0	12672.0	1.49	7.98	5.55	1.47	300.00	158.40	ǁ	Hayes. (2017)*
42	**Illapel, Chile**	Sep 16, 2015	3.33E+21	8.30	24700.0	5500.0	3.65	10.43	1.00	1.80	190.00	130.00	ǁ	Okuwaki *et al*. (2016)*
43	**Pedernales, Ecuador**	Abr 16, 2016	7.06E+20	7.82	33600.0	7980.0	0.46	3.97	3.04	2.29	210.00	160.00	ǁ	Hayes. (2017) †
44	**Quellon, Chile**	Dic 25, 2016	2.93E+20	7.57	17661.0	2583.0	0.33	5.68	2.64	2.11	145.00	121.80	ǁ	Hayes. (2017) †
45	**Alaska, USA**	Mar 28,1964	5.50E+22	9.10	225000.0	40000.0	4.00	17.40	23.5	2.4	500.00	5000.00	ǁ#	Ichinose *et al*. (2007)‡

*SRCMOD, †NEIC, ‡Ichinose *et al* (2007). § Strong-Motion data, ǁ Teleseismic data, # Geodetic data. R_{min}, minimum source-to-station distance in Strong Ground Motion data inversions.

ANEXO 2. Material suplementario para el capítulo III

Supporting Animations

Animation Captions

S2.a. Earthquake Slip Distribution Evolution.

S2.b. Earthquake Surface Displacement Distribution Evolution.